UNIVERSITY OF TRENTO - Italy

Doctoral dissertation

in fulfillment of the requirements for the degree of
Doctor of Philosophy in the subject of Physics

OPTICAL BIOSENSORS FOR MYCOTOXIN DETECTION IN MILK

Supervisor:
Prof. Lorenzo Pavesi

Ph. D. candidate:
Tatevik Chalyan

NanoScience Laboratory
Department of Physics

XXX PhD cycle in Physics
July, 2018

UNIVERSITY OF TRENTO - Italy

Doctoral dissertation

in fulfillment of the requirements for the degree of *Doctor of Philosophy* in the subject of Physics

---

Optical biosensors for mycotoxin detection in milk

Supervisor:
Prof. Lorenzo Pavesi

Ph.D. candidate:
Tatevik Chalyan

NanoScience Laboratory
Department of Physics

XXX PhD cycle in Physics
July 2018

"True education does not consist merely in the acquiring of a few facts of science, history, literature, or art, but in the development of character."

David O. McKay

iv

Acknowledgements

At the end of this long scientific journey, full of hopes and emotions, it is the right moment to recall all the achievements of my PhD life and acknowledge everyone who has had an impact in the realization of this wonderful experience.

Almost three and a half years ago, my life changed when I moved from Armenia to Italy. New places, new people, new language... everything new. I faced the challenge of integrating myself in the new environment and becoming a part of the beautiful city of Trento. During the PhD, I was always inspired by Trentino mountains. I correlated every new achievement with a new peak and I knew that in order to get to the top, motivation and hard work were needed. Although the peaks were the most exciting achievements, the path and the difficulties that I overcame were the biggest lessons that I have learnt. I truly believe that PhD is not only the research or written papers, it is the experience of facing problems and becoming confident to solve them. It is daily hard work, ups and downs, that in the end of the day, shape a strong character. The answer to the question, if I fulfilled all my expectations from the PhD is simple: the knowledge is never enough and I will continue to study and learn. But the experience of being part of the European project, multidisciplinary meetings and attending conferences, accomplished with a great success in SPIE UNITN Student Chapter management, satisfied and motivated me to continue in the same direction. However, all these achievements would not have been possible if I did not have all those people with whom I paved my way to self-realization. I am so lucky to be surrounded by the right people who supported and corrected me every single step of the way. I thank each and everyone personally.

The first person is my supervisor Prof. Lorenzo Pavesi, whom I want to thank for the PhD experience exactly as mine was. Thank you Prof. for noticing an unexperienced Armenian girl four years ago in Trieste and for giving me the chance to discover myself and to be a part of NanoLab. I admire the fact that although being so busy, you could always find a moment to support and encourage me. I wish one day to make you proud of me as much as I am proud of being your student. Next, I want to thank Mher, whose presence gave me more confidence and who for me, set

an example of an Armenian who is recognized and appreciated thanks to his talent and hard work. As a part of Nanolab, I have met the most wonderful colleagues and friends that one can ever wish for. Apart from all the scientific discussions and working hours, with every one of you I have a special moment and a memory to cherish. Davide, a maestro, a colleague, a perfectionist and a friend who opened the world of biosensing to me and prepared me for an independent research, thank you for all the knowledge and experience. The short period of working with you was probably the most productive and enjoyable one. I want to thank also Romain, for supervising me during the first year of my PhD. Special thanks to Prof. Marina Scarpa for the infinite discussions on binding kinetics and to Paolo, to the first person in Trento, who met and helped me to reach home the day of my arrival. Big thanks to Enrico and Giorgio, for the most enthusiastic discussions on lasers and noises, in particular, during the last eight months. Your professionalism is so motivating for a beginner like me.

Some say that we discover people during the trips and in critical situations. The trip to Sicily and OPTICS-2018 were the best demonstration of friendship and the sense of being a team. For all the things that we did together, thank you Massimo, Claudio, Mattia, Alessandro, Stefano S., Sara, Zahra, Fernando, Stefano B., Fabio, David, Chiara, Maddalena, Chiara V., Pierre, Stefano T. I hope to keep our friendship forever.

Finally, I want to say enormous thanks to Tania, who was my best advisor, supporter in Trento and a person able to find words to make me calm in any situation. I appreciate with all my heart all your efforts for my career development.

Being involved in a European project, my activities were not limited to Nanolab only, and fortunately I had an opportunity to work with Laura and Cristina, "le mie donne preferite". Your role in my PhD research and acquiring knowledge of biosensing is incredibly important. I can surely say that your trust in me was the fundamental base of my success. Thank you for being my teachers and friends in any situation. I want to mention also Andrea Adami, with whom at the end of the SYMPHONY project we worked up to 18 hours per day but finally we managed to integrate the system. They were the hardest but at the same time the most satisfying days of my PhD.

In addition, I would like to thank my colleagues from LioniX, in particular René and Hans, who gave me the chance to do an internship in the company. Special mention to Geert, whose efforts to teach me a gentle use of biological solutions resulted me the final section of my thesis. Thank you Erik, Floris and Lennart, for all the fruitful discussions and exchange of experiences.

For me my work has always been the priority, but there are special people, thanks to whom, I was able to discover and enjoy Trentino out of the laboratory and feel at home far away from my home. My Sanba family Pranab, Biniam, Linda, Safà, Behrouz, Payam, Amanda, Caterina, Nasim, Azzurra, Luigi, Gregor, Emanuele, Giorgia, Milica, Nonie, Behzad, Shahab, Andrea C. and Trentino Armenians Ruzanna, Lusine, Davit, Larisa, Lilit surrounded me with love, smiles, care and crazy and unforgettable days, that will always warm my heart. Particularly, I want to express my gratitude to Pranab, who was always ready to listen and understand me, but never closed his eyes to my mistakes.

On the moments of success one should always remember the start. My true start was in LT-PYRKAL, even before PhD. I will always be thankful to Mr. Buniatyan, Sarkis, Tigran, Sergey Surenich, Larisa and Armen for the confidence and experimental skills that I have learnt from them.

Finally, I want to dedicate my thesis to the people without whom I just cannot imagine myself and this PhD. They are my family and two best friends Sona and Artur. To my parents, Vardan and Gayane, my sisters Astghik and Arevik and my brother Gor, I dedicate not only this thesis, but all my achievements now and ever, because they are my strength and the most important people in my life. Everything is possible when I know that you guys have my back. Sona, you became a sister to me, thank you for living with me all three and half years of "OUR" PhD, for all the love, happiness and calls to wake me up every single morning. Artur, I will never be able to express how grateful I am for everything you have done for me. You have always been there for me and you were always ready to encourage and push me ahead. By taking me out from my comfort zone, you helped me to dream and realize those dreams. I promise to do the impossible to make all of you always be happy and proud of me. I am grateful to have you in my life.

Tatev Chalyan

Trento, 2018

Abstract

Optical biosensors, and in particular label-free optical biosensors have become one of the most active and attractive fields within the biosensing devices. The portability and the possibility to set free from the laboratory settings gave a new hint for integrated photonic biosensors development and use in numerous applications. Integrated photonic sensors have shown very promising results, and in particular, devices like WGM resonators and interferometers are showing high sensitivities and miniaturization abilities, which allow the realization of an integrated complete lab-on-chip device.

The main goal of my thesis is the development of an optical biosensor for the fast and comprehensive detection of carcinogenic Aflatoxin M1 (AFM1) mycotoxin. The acceptable maximum level of AFM1 in milk according to European Union regulations is 50 ng/L equivalent to 152 pM for the adults and 25 ng/L equivalent to 76 pM for the infants, respectively.

Within a European Project named *SYMPHONY*, we develop an integrated silicon-photonic biosensor based on the optical microring resonators (MRR) and the asymmetric Mach-Zehnder Interferometers (aMZI). The sensing is performed by measuring the resonance wavelength shift in the MRR transmission or the phase shift of aMZI caused by the binding of the analyte to the ligand immobilized on the sensor surface. These measurements were my principal task within the project.

The experimental characterization of the bulk refractometric sensing of the devices is performed in a continuous flow. This characterization assesses the high resolution of both device types, which are able to resolve variations in the refractive index of the liquids with a limit of detection down to 10^{-6} refractive index units (RIU).

Furthermore, the *SYMPHONY* sensor optimization based on the Fab' and DNA-aptamer functionalization strategies is realized. It is therefore

demonstrated, that the Fab' functionalization strategy provides more reproducible results with respect to the DNA-aptamer one. However, for both strategies, the specificity of the sensor functionalization to detect AFM1 molecules is achieved with respect to non-specific Ochratoxin molecules at high concentrations.

In the final stage of the *SYMPHONY* project, the Fab'-based functionalized aMZI sensor is tested with real milk samples (eluates) prepared in the *SYMPHONY* system that consists of the three main modules: the defatting module, the concentrator module and the sensor module. The system calibration yields the minimum concentration of AFM1 at 40 pM to be detectable.

The detection of the ligand-analyte binding in real-time enabled the study of the kinetics of the binding reaction, and we measured for the first time the kinetic rate constants of the Fab'-AFM1 interaction with our sensors.

Finally, a MRR based affinity biosensor is developed dedicated to the biotinylated BSA - anti-biotin binding study. An affinity constant of 10^6 M^{-1} is measured. The sensor is successfully regenerated up to eight times by applying longer incubation period.

Contents

List of Abbreviations

AFB1	**A**flatoxin **B**1
AFM1	**A**flatoxin **M**1
aMZI	**a**symmetric **M**ach-**Z**ehnder Interferometer
BHF	**B**uffered **HF** oxide etch
BSA	**B**ovine **S**erum **A**lbumin
CMOS	**C**omplementary **M**etal **O**xide **S**emiconductor
DMSO	**D**imethyl **S**ulfoxide
DRIE	**D**eep **R**eactive-**I**on Etching
EDS	1-ethyl-3-(3-dimethylaminopropyl)carbodiimide hydrochloride
ELISA	**E**nzyme-**L**inked **I**mmunosorbent **A**ssay
FEM	**F**inite **E**lement **M**ethod
FOM	**F**igure **O**f **M**erit
FSR	**F**ree **S**pectral **R**ange
HPLC	**H**igh **P**erformance **L**iquid **C**hromatography
ID	**I**nner **D**iameter
LOD	**L**imite **O**f **D**etection
LPCVD	**L**ow-**P**ressure **C**hemical **V**apor **D**eposition
MES	2-(N-**M**orpholino)**E**thane**S**ulfonic acid
MFD	**M**ode **F**ield **D**iameter
MZI	**M**ach-**Z**ehnder Interferometer
MRR	**M**icro **R**ing **R**esonator
NHS	N-hydroxysuccinimide
NIR	**N**ear **I**nfrared
OD	**O**utside **D**iameter
OSA	**O**ptical **S**pectrum **A**nalyzer
OTA	**O**chratoxin **A**
PBS	**P**hosphate **B**uffered **S**olution
PCB	**P**rinted **C**ircuit **B**oard
PDMS	**P**olydimethylsiloxane

PD	**P**hoto**d**etector
PECVD	**P**lasma-**E**nhanced **C**hemical **V**apor **D**eposition
PM	**P**olarization **M**aintaining
PMMA	**P**olymethylmethacrylate
RIE	**R**eactive-**I**on **E**tching
SEM	**S**canning **E**lectron **M**icroscopy
SOI	**S**ilicon **O**n Insulator
SM	**S**ingle **M**ode
SNR	**S**ignal to **N**oise **R**atio
SPR	**S**urface **P**lasmon **R**esonance
TEOS	**T**hermal **O**rthosilicate
TE	**T**ransverse **E**lectric
TFF	**T**angential **F**low **F**ilter
TIR	**T**otal **I**nternal **R**eflection
TM	**T**ransverse **M**agnetic
TLC	**T**hin **L**ayer **C**hromatography
TRIS	**T**ris(hydroxymethyl)aminomethane
VCSEL	**V**ertical-**C**avity **S**urface-**E**mitting **L**aser
VIS	**V**isible
WGM	**W**hispering **G**allery **M**ode

Chapter 1

Introduction

1.1 Thesis Structure

This thesis is structured into four chapters.

Chapter 1 gives the introduction of the problem, existing solutions and the key components of the biosensors for mycotoxin detection. Then I introduce different types of the optical biosensors, in particular SPR, waveguide and fiber based evanescent sensors. This chapter is concluded with the state-of-the-art of the optical sensors for later comparison with the devices developed during my PhD.

Chapter 2 gives a general theoretical background, that entails the models and equations used to describe the MRR and aMZI based biosensors. It covers both the description of the kinetic of the binding reactions, that selectively recognize the analyte molecules, and the description of the photonic sensors, that transforms the binding to a measurable signal.

Chapter 3 reports on the development and characterization of the experimental apparatus. Here, I have optimized and tested optical setups, for the precise and stable measurement of the three different photonic sensors used in this thesis which are based on MRR (fabricated in FBK and LioniX) and aMZI (fabricated in LioniX) at 850 nm. Therefore, the setup for *SYMPHONY* MRR devices was initially realized by Dr. Davide Gandolfi. In the conclusion of the chapter, I present the final integration of the *SYMPHONY* system realized by me.

Chapter 4 is dedicated to the results and discussions. In particular, in § 4.1 the experimental results on the MRR based sensors, developed within *SYMPHONY* project are presented. This device is designed by Dr. Davide Gandolfi and Dr. Romain Guider, and fabricated by Dr. Alina Samusenko.

The results on the optical characterization of the MRR based photonic chips and the bulk sensitivity measurements that are reported in § 4.1.1 and § 4.1.2, respectively, as well as some of the results in § 4.1.3 are obtained by me and Dr. R. Guider. The functionalization of the MRR based biosensors, both with DNA-aptamers and Fab', is performed by Dr. Laura Pasquardini.

In § 4.2 all the experimental results presented for aMZI based sensors are obtained by me. Surface functionalization is done by Dr. Cristina Potrich in LABSSAH, FBK. The optical and bulk sensitivity characteristics of the sensors are demonstrated. First, the sensing of AFM1 in buffer solution is realized with the Fab' functionalized aMZI sensors. For Fab'-AFM1 molecular interaction the affinity and dissociation constants in buffer are calculated. Finally, AFM1 detection in real milk samples and the sensor calibration are reported in § 4.2.5 and § 4.2.6, respectively.

The last § 4.3 of this chapter is dedicated to the results, obtained during my internship in LioniX. Under the supervision of Dr. Geert Besselink, I developed an affinity biosensor based on the multi MRR photonic chips for the biotinylated BSA and anti-biotin interaction studies. Binding constants, as well as the affinity of the sensor are measured. The sensor regeneration to eight times is realized.

Appendix A shortly reports on the preparation of the buffers and regeneration solutions, as well as materials used both in the studies of AFM1 and anti-biotin. While Appendix B shows the steps of milk sample preparation in the *SYMPHONY* system, i.e. fat removal and concentration details.

1.2   Biosensor

"Any device that has specific biochemical reactions to detect chemical compounds in biological samples..."

Leland Clark
"Father" of Biosensors

A biosensor is a complex integrated device providing a specific quantitative or relative analytical information on a sample through a biological recognition element which is in direct spatial contact with a transduction element [1]. It is a manifold system connecting different fields such as biology, chemistry, optics, electronics, informatics in a single device. In 1975 the first commercial biosensor to analyte whole blood glucose content was reported [2]. Since then, the biosensors technology started, by the development of different components of the whole system, improving the performance and the specificity of biosensors, as well as including new targets for detection. Figure 1.1 shows the key components of any biosensing device.
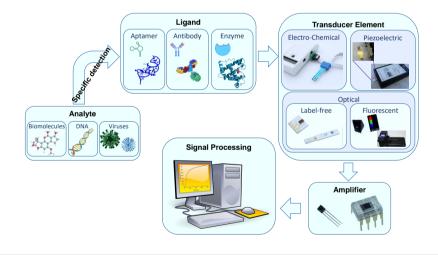

FIGURE 1.1: Key components of a biosensor[1]. The transducer receives a signal from a ligand-analyte reaction which is read as an electrical/optical signal in real-time.

In order to detect the target molecules, i.e., the analyte, the transducer element is immobilized (activated) with specific molecules, so called ligand or receptor, that can react with the analyte. In this way, the biomolecular interaction of the analyte and ligand/receptor is sensed by the transducer and a signal, which can have electro-chemical [3], optical [4] origin is generated.

In particular, in this thesis an optical transducer based on silicon is studied. Silicon based mass-production and low-cost technologies, such as silicon photonics, are attractive by providing a possibility of a biosensor fabrication in which reaction and analysis take place in a single device.

In recent years a class of electro-chemical transducers, based on graphene, is suggested to become the cheapest technology for sensing applications, thanks to the easy and accessible fabrication of graphene using graphite. This new generation of biosensors is already applied in the detection of various analytes, in the field of clinical, environmental and food research [5].

Other examples of transducers are microelectrodes arrays (MEA) [6], which have applications in impedance spectroscopy, in recording the neural activity in-vitro and in-vivo, and microelectromechanical systems (MEMS) [7]. Lastly, microcantilevers [8] and quartz- crystalmicrobalances (QCMB) [9], that perform gravimetric sensing exploiting the change in resonance frequency of a vibrating piezoelectric crystal [10] need to be mentioned.

The variety of analytes is growing very fast, depending on applications, such as health control, food safety, environment monitoring, drug delivery. Day-by-day, appearance of new viruses, toxins, new DNA mutations demand proper ligands to observe them. In order to fulfill these needs of selective recognition, also different kinds of ligands have to be explored. Selectivity is the ability of a (bio-)sensor to recognize preferentially a certain analyte, or class of analytes, even in presence of other interfering species. According to the International Union of Pure and Applied Chemistry (IU-PAC) definitions [11, 12], specificity is the ultimate of selectivity i.e., the ability of the sensor to respond only to its target. The most known and wide

---

[1]The parts of the picture are taken from:
viruses (https://goo.gl/L8efxU), aptamer (https://goo.gl/zGCyaF),
antibody (https://goo.gl/cs28XW), enzyme (https://goo.gl/NrkfrF),
electro-chemical (https://goo.gl/B9yKKs), piezoelectric (https://goo.gl/aYfe8a),
label-free (https://goo.gl/VKxeV9), fluorescente (https://goo.gl/y3942p),
amplifier (https://goo.gl/ddg8zC)

spread ligands are enzymes, aptamers, particularly DNA and RNA, antibodies etc. Antibodies have been employed in molecular bio-recognition since 1950s and they are exposed in the heart of immunoassays. Their many characteristics, like diversity, high affinity, well studied regeneration methods of antibodies, undeniably make them a powerful biorecognition element [13]. At the same time, aptamers and, mainly, DNA-aptamers emerge as competitors in the field of in-vitro diagnostics [14]. Thanks to their small dimensions, they are suitable for a high-density coverage of the sensor. In addition, aptamers are stable to long-term storage.

There is a continuous challenge for the development of biosensors and technologies that are able to simultaneously detect multiple biological materials, from whole cells to single molecules, with increasing capabilities. In addition, depending on the detection approaches, we can define two groups of biosensors: *labeled* and *label-free*. While the labeled detection requires a secondary molecule or an amplification step, label-free detection enables the sensors to directly detect the molecule of interest after the capture reaction [15]. An example of labeled detection method is the fluorescence microscopy where target biomolecules are stained (labeled) with fluorescent markers to increase the resolution and the contrast of the microscope image. Despite the fact that labeled detection methods have the advantage of the dual-confirmation of the presence of the analyte thanks to the secondary molecule, which reduces false-positive readings, the secondary molecule introduces an additional time-consuming step, thus making labeled detection methods not suitable for rapid and real-time sensing applications. On the other hand, the quantitative analysis are challenging due to the fluorescence signal bias, as to each molecule belong to number of fluorophores that cannot be precisely controlled [16], thus making the fluorescence-based biosensors applicable in cases when pure solutions are studied. Nevertheless, for the biomolecular interaction studies, affinity characterizations, the presence of a label, might affect the interaction process. In this case, the use of a label-free technique is preferable. Label-free Biomolecular Interaction Analysis (BIA) is a powerful technique to study the chemical binding of molecules in real-time. BIA is an important method for drug discovery and drug development [17]. Finally, label-free approach is more economic, as it does not require additional labeling step and is applicable for small volumes of analyte studies.

During the past years, concerns were raised on the portability and on

the possibility of freeing biosensors from the laboratory settings. This requires the sensor integration with microfluidics and the realization of a complete integrated lab-on-a-chip device [18]. The role of microfluidic systems is highly important, since they take control of flow conditions, mixing rates of different reagents, as well as of reducing sample and reagents volume [19]. In fact, lab-on-a-chip is a term for devices that integrate (multiple) laboratory functions on a single chip of only millimeters to a few square centimeters total area and that are capable of handling extremely small fluid volumes down to less than picoliters. Figure 1.2 is an ideal demonstration of the idea of a lab-on-a-chip device.

FIGURE 1.2: Lab-on-a-chip principle[2].

There are many applications where a highly integrated lab-on-a-chip device could be of particular interest. Therefore, lab-on-a chip devices became more prominent after the evolution of *Complementary Metal Oxide Semiconductor (CMOS)*, a standard fabrication technology for silicon-based microelectronics which expanded the development of multidisciplinary,integrated

---

[2]The picture is taken from http://www.gene-quantification.de/lab-on-chip.html

sensing platforms, by taking advantage of several favorable optical properties of silicon, such as the high refractive index, that enables the realization of small optical components [20]. The easy fabrication with CMOS processes, fosters a low cost for eventual mass production of Silicon On Insulator (SOI) wafers. Spectral properties of the material allow silicon photodetectors and waveguides fabrication to operate next to each other on a single platform. The particularity of multiplexing capabilities of an integrated lab-on-a-chip biosensor permits screening of the target sample against several markers, thus increasing accuracy and speed of detection. This approach, for example, is used for the recognition of particular diseases or for pharmaceutical researches [21]. The possibility of real-time monitoring of reaction kinetics offered by these type of biosensors, makes them indispensable tool in drug screening and development industry. These devices find a use not only in the medical diagnostics or in specialized laboratories, but in point-of-care instrumentations [22], as well as for the environmental and pollution monitoring, where lab-on-a-chip biosensors can be used to detect bacteria, chemical compounds or heavy metals [23], present in the atmosphere, in the soil or in the water directly in nature. Another application of lab-on-a-chip biosensors, and perhaps in recent days, a highly demanding one, is in the field of security and counter terrorism. Small traces of chemical and biological warfare agents, life-threatening gases can be detected in airports, stadiums and other critical safety scenarios [24].

Finally, we recall the application of the lab-on-a-chip label free biosensors that is one of the goals of my thesis, i.e., food safety control. Biosensors are used in detection of contaminants in the food industries, such as pesticide, toxin, mutated DNA sequence, etc. Here, we mainly focus on the study of a lab-on-a-chip optical biosensor immobilized with the antibodies or DNA-aptamers, for a label-free detection of mycotoxins, in particular Aflatoxin M1 in milk.

1.2.1 Mycotoxins

For a biosensor development the first important step is to understand the target molecule which has to be detected. Understanding the nature of the analyte permits to select proper ligands and construct sensitive tool for the detection. Here, we will concentrate on mycotoxins, in particular aflatoxins, that are present in milk and dairy products.

Contamination of food and agricultural products by various types of toxigenic molds (fungi) is a serious and a global problem that becomes a subject of many researches in increasing number of countries. Studies showed that approximately 25% of the crops in the world get contaminated by molds and are affected by mycotoxins [25], causing the economic loss of billions of dollars. Climatic conditions, such as rain, humidity, heat etc., can stimulate fungal growth, as well as poor harvesting practices, improper drying, handling, packaging, storage, and transportation conditions contribute to the process and increase the risk of mycotoxin production. Fungal toxins have been detected in various food commodities from many parts of the world and have been recognized to be one of the most dangerous contaminants [26] that affect human and animal health.

Mycotoxins are produced by some of the specific strains of filamentous fungi belonging to species of the genera Aspergillus, Penicillium, and Fusarium that affect crops at the field level and may grow on food during storage under certain favorable conditions. Mycotoxins are considered as "risk factor" to humans highly depending on the toxicity of the mycotoxin, the dose involved and the extent of the exposure. Since 1960, nearly 400 types of mycotoxins have been discovered. From the point of view of health, the important mycotoxins in human and animal food include: aflatoxins, ochratoxin, trichothecenes, fumonisins, and patulin.

1.2.1.1 Aflatoxins

Aflatoxins are highly toxic, mutagenic, teratogenic and carcinogenic compounds that are produced as secondary metabolites by fungi belonging to several Aspergillus species, mainly A. flavus and A. parasiticus [27, 28]. Aflatoxins have a high presence in tropical and subtropical regions where humidity and temperature conditions are optimal for toxin production. The name "aflatoxin" comes from the combination of "a" for the Aspergillus genus, "fla" for the species flavus, and ends with the word toxin, because of its toxicity. The severe outbreak of turkey "X" disease (in the U.K.) that resulted in the death of more than 100000 turkeys and other farm animals, in 1960s, led to the discovery of aflatoxins. The cause was attributed to Brazilian peanuts fed to the animals, which was contaminated with A. flavus. Aflatoxins are found in a wide range of agricultural products, including cereals (maize, rice, wheat), spices (chillies, black pepper, ginger), tree nuts

(almond, pistachio, walnut, coconut), milk (human and animal), and butter (see Figure 1.3). The fact that the listed products are used in everyday life, makes aflatoxins even more dangerous.

Different types of aflatoxins have been identified wherein the major ones include aflatoxin B1, B2, G1, G2, and M1. Fungal species belonging to Aspergillus flavus typically produce AFB1[3] and AFB2, whereas A. parasiticus produces AFG1 and AFG2 as well as AFB1 and AFB2. These aflatoxins are classified by International Agency for Research on Cancer (IARC) as Group 1 carcinogens [29].
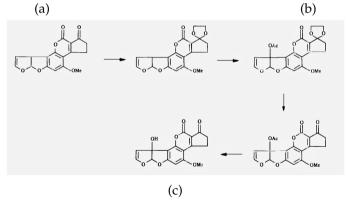

(a)   (b)

(c)

FIGURE 1.3: (a) Maize cob and (b) peanuts colonized by Aspergillus species[4]. (c) Chemical conversion of AFB1 to AFM1.

---

[3]Aflatoxins are labeled as AF+the type, for example AFB1.

Less toxic AFM1 that is present in milk is a result of AFB1 mutation in animal (caw, sheep, goat) organism. Figure 1.3c shows the steps of the chemical conversion of AFB1 to AFM1 [30]. It is generally recognized that contamination of milk and milk products with AFM1 varies according to geographical location (dry or wet) and season (hot or cold).

Since most of the human species, as well as animals, particularly the young nurturing ones, are dependent on milk as a part of complete basal nutrition, AFM1 contamination in milk and its products are of extreme importance and is a serious problem. In 1993 the IARC categorized AFM1 as a 2B human carcinogen [31]. Later, the European Commission regulation (EC) No. 1881/2006 specified the maximum level of AFM1 contamination in milk to 50 ppt (50 pg/ml), and to 25 ppt (25 pg/ml) for infant formulae. However, a long-term consumption of AFM1 at low levels (ppb) may lead to the development of hepatocellular cancer. Aflatoxins are perceived to be co-factors in the higher incidence of liver cancer (hepatocellular carcinoma) along with hepatitis-B virus for instance [32].

1.2.2 Aflatoxin M1 detection techniques

Many methodologies have been researched to remove AFM1 from milk by adsorption using bentonite, applying ultraviolet radiation, humic acids etc. However, AFM1 is know to be resistant against chemical and thermal treatments [33]. Consequently, it is highly important to detect and eliminate contaminated milk immediately after getting it from animals. Numerous techniques have been developed for this purpose.

1.2.2.1 High Performance Liquid Chromatography (HPLC)

The generally accepted method for the detecting of Aflatoxin M1 in milk is the High Performance Liquid Chromatography (*HPLC*) [13, 34]. The HPLC instrumentation consists of few fundamental parts. First, the mobile phase, i.e., the solution, which contains the target particles, held in solvent reservoirs, is pumped through the system by one or more pumps at a constant

---

[4]The pictures are taken from:
(a) *https://goo.gl/NU63jz*, (b) *http://aquafind.com/articles/Mycotoxin.php*

flow rate and delivered to the specific column under high pressures (400 atmosphere) [35]. The HPLC column is composed of a metal or plastic cylinder, that contains a packing of small porous particles with a second phase bound to the surface [36]. The solution, flowing in the column, is called a stationary phase. The sample mixture flows through the packed particle bed at a constant flow rate. During the flow, each component of the mixture interacts with the stationary phase at a different rate, thus causing the sample separation. Next, the separated components are eluted and moved into a detector cell. Detection is realized by absorption spectroscopy at a wavelength of 220 nm. A quantitative information about the initial amount of the target compounds can be extracted from a chromatogram, which gives a dependence of the intensity, corresponding to each component, from the elution time.

HPLC is used for confirmation and precise quantification of AFM1 present in milk after it has been detected by other relatively fast techniques. HPLC is an expensive technique to perform, mainly due to the cost of the instrumentation and the cost of employment of technical operators. In particular, in countries where the level of AFM1 is the highest (India, African countries), the possibility to examine milk with HPLC is less probable.

1.2.2.2 Thin Layer Chromatography (TLC)

Thin Layer Chromatography (*TLC*) method is older (first time used in 1966) than HPLC and has several advantages. It is far cheaper than HPLC methods and it does not require extensively trained operators, however it is less accurate than HPLC [37]. TLC with fluorescence detection was applied for ultimate separation of the aflatoxin spots from the background, detection, and quantification. In this method, ultra-violet light is used for the detection and the typical monitoring of the presence of AFM1 in a blue fluorescent line. In developing countries TLC is the preferred detection technique due to the low cost and ease of use.

1.2.2.3   Enzyme Linked ImmunoSorbant Assay (ELISA)

The most common technique for AFM1 detection in milk (even if not an ac-
creditate method) is the *ELISA* (Enzyme Linked ImmunoSorbant Assay), in-
troduced in 1971, by Peter Perlmann and Eva Engvall at Stockholm Univer-
sity in Sweden [38]. It is a plate based assay. The general concept of ELISA,
particularly for AFM1 detection, is the following: the assay is performed
by adding AFM1 standard controls and samples to anti-AFM1 monoclonal
antibody-coated wells. Then the plate is left to incubate for 20 minutes.
During this time the AFM1 molecules bind to the antibody. After the first
washing step, AFM1 that has been conjugated to horseradish peroxidase
(AFM1-HRP) is added and incubated for 10 more minutes, thus allowing
the conjugate to bind to any remaining unbound antibody. After the second
washing step, substrate is added, which reacts with the bound conjugate to
produce blue color. The color development is inversely proportional to the
AFM1 content in the sample, i.e., more blue color means less AFM1. The in-
tensity of color/ optical density is measured at 450 nm. A calibration curve
is obtained be plotting the optical densities of the standard solutions.

  The advantages of the ELISA technique are the fast analyses and the cost
of the equipment required [39]. However, a positive ELISA result needs
to be verified by HPLC. Frequently, ELISA method yields higher concen-
trations than those obtained by HPLC. The origin of this mismatching can
be a fake signal due to the cross-reaction between antibodies and proteins
present in milk [13].

1.2.2.4   Bilayer Lipid Membranes (BLM)

Another reliable technique for AFM1 detection in milk is Bilayer Lipid Mem-
branes (*BLM*), classified as a non immunochemical technique [40]. BLM
based biosensors are meant for laboratory use by specialized personal. They
are attractive thanks to fast analyses durations of approximately 15 seconds.
The idea of BLM technique is quite simple. As a consequence of the interac-
tion of AFM1 and a lipid membrane, channels in the lipid membrane open
and allow the eluent to pass through. The eluent is an ionic solution so that
changes in ion concentration can be monitored using an electrochemical de-
tector. By controlling the flow rate it is also possible to eliminate protein
interferences that usually give a non-specific and fake response. The great

advantage of this technique is the possibility of multiple use of lipid membranes. The cost of the equipment is much lower than HPLC.

1.2.2.5   Rapid One Step Assay (ROSA)

Besides the listed detection techniques, which are widely used in all over the world, a fast and simple way of the AFM1 detection in milk is developed by the Charm Sciences Inc. The Rapid One Step Assay (ROSA)[5] is a lateral flow test that can be run using the Charm EZ system or ROSA Pearl-X Reader. ROSA realizes the AFM1 quantitative detection at the US FDA action level of 0.5 ppb (500 ppt) in dairies and food manufacturers. The duration of the test is 8-minutes. After the 8-minutes incubation with the ROSA incubators which provide the exact temperature and time needed for each test reaction, the Charm EZ reads and displays the result of the test as "Negative" or "Positive".

By the same equipment it is possible to test the presence of different antibiotics in milk as well.

1.2.2.6   Summary of AFM1 detection methods in milk

Besides the commercially available detection methods, there are several other techniques for the AFM1 detection in milk. One example of the AFM1 detection system is a gold microelectrode array (MEA) immunosensor accomplished with ELISA [6]. Other detection system based on a competitive immunoassay using horseradish peroxidase (HRP) as a tag and the magnetic nanoparticles coated with anti-AFM1 antibody in order to separate the bound and unbound fractions of milk sample is reported [41]. Immunoassays have application also in the membrane-based flow-through enzyme immunoassay sensors for the AFM1 detection since 1999 [42].

Even though the immunological techniques have many advantages such as relatively rapid and sensitive analysis, however, they are limited by their elevated cost. As alternatives, the aptamer based sensing technologies are developed. Recently, the magnetic nanoparticles immobilized with the DNA-aptamers have been employed in the sensing platform for the AFM1 detection in a range of 20 and 1000 ng/kg concentrations [43].

---

[5]https://www.charm.com/rosa-lateral-flow-antibiotic-strip

Table 1.1 summarizes the lowest detectable concentrations of AFM1 monitored by the described approaches.

TABLE 1.1: Laboratory based techniques for Aflatoxin M1 detection in milk. LOD shows the limit of detection.

Technique name	AFM1 LOD (ppt)	~Duration (hours)	Reference
HPLC	4.5	72	[34, 44]
TLC	5	4-5	[45]
ELISA	4.3	3	[39, 46]
BLM	16	0.5	[40]
ROSA	500	0.15	[47]
MEA	8	2	[6]
Electrochemical	10	0.5	[41]
Field Immunoassay	50	3	[48]
DNA-aptasensor	20	4	[43]
SPR	0.6	2	[42]

One can notice, that among the listed techniques, except the last one, i.e., Surface Plasmon Resonance (SPR), all the others are based on fluorescence or electrochemical detection mechanism. The name of the SPR method, already indicates its origin to be an optical sensor. The next section is committed to the optical biosensors, which are based on the evanescent field sensing mechanisms.

1.2.3   Optical biosensors

The first optical sensors came into sight in 1937, when Langmuir and Schaefer described the determination of a biomolecule adlayer thickness formed on a metallic surface via the observation of colors produced by reflective interference [49]. However, the real outbreak of optical biosensors occurred in the mid-90s with the development and realization of micro-fabrication technologies and detection systems. Since then, optical biosensors, in particular label-free optical biosensors, have become one of the most attractive

biosensing devices thanks to a number of unique characteristics such as the use of light, which rules out electrical interference, and the excellent bio-analytical performance. The choice of the transducer is dictated by several fundamental parameters that leads to the prioritization of one or the other detection method. The most obvious one is the limit of detection (LOD) [50, 51], which can be defined as the smallest detectable concentration of the target analyte or the lowest detectable molecular mass of the target molecules, or the lowest detectable surface mass density of the target substance. Thanks to the possibility of miniaturization, optical biosensors can be utilized to test small (down to few microliters) sample volumes. This point sometimes can be crucial if the sample volume is available in very limited amounts (e.g., human drug targets) or the transducer is integrated with other processes delivering small sample amounts. Optical biosensors are winners in terms of simultaneous multiple sensing possibilities in short detection time. The more multiplexed a sensor, the more parallel tests can be performed at the same time, keeping the equipment size and cost to the minimum. A wide range of transducer principles was developed in the last three decades. Next, a few of the most important types of the optical biosensors, i.e., SPR, waveguide and fiber based sensors are described.

1.2.3.1 Surface Plasmon Resonance (SPR)

A wide class of optical label-free biosensors is based on a surface plasmon resonance (SPR) phenomena. It is the most popular and commercialized optical biosensor technology today. This technology provides binding, kinetics, affinity, specificity and concentration, without any need of labelling. Surface plasmon resonance was demonstrated for the first time by Liedberg in 1983 [52], even though the basic phenomenon was already described by Kretschmann since 1968 [53]. A surface plasmon wave (SPW) is a charge density oscillation occurring at the boundary of two media with dielectric constants of opposite signs, such as a metal (gold or silver) and a dielectric. The SPR method is based on the change in the SPW resonance caused by the change in the refractive index of one of the two medias. In any SPR configuration, the incident light totally reflects from the dielectric-metal surface and generates an evanescent field penetrating into the metal layer. Under certain angles or wavelengths, the propagation constant of the evanescent field matches with SPW, resulting in a resonance coupling of the incident

light with SPW. This yields an intensity loss in the output reflected light and the appearance of a characteristic negative peak (deep) in the intensity profile of the reflected light as a function of the incident angle. The position of the deep, and consequently of the resonance angle, is correlated with the refractive index near to the metal surface. Thus, a change in the surrounding environment yielding a change in the refractive index causes the displacement of the resonance angle which is measured by the shift of the intensity deep. In particular, using a metal surface as a layer for ligand molecules immobilization, and flowing a target solution over that layer, the molecular binding event can be monitored by recording the angular position of the intensity deep [54].

Among various SPR configurations, based on a light coupling technique, such as prism coupling, waveguide coupling, fiber optic coupling or grating coupling, the most convenient one to get the lowest sensing limit of detection is the prism based method, even though it is bulky and creates several challenges for integration in a compact lab-on-a-chip device. Waveguide coupling is a good alternative and in contrast to the prism, it is easily integrable. Figure 1.4a shows the SPR prism configuration working principle.

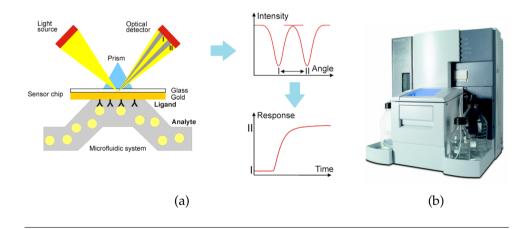(a)   (b)

FIGURE 1.4: (a) The angle of reflected intensity changes when target molecules bind to the molecules immobilized on the surface of the gold layer and, therefore, changes the refractive index[6]. Decrease of intensity is real-time monitored and represented as a sensorgram. (b) SPR GE Biacore T200 commercial system.

Numerous commercial apparatuses exist based on the SPR method. The most known and commonly used are the *Biacore*[7] instruments that are totally automated so that the analysis and the sensor regeneration is computer controlled. The sensor chip in Biacore systems, consists of a glass slide coated with gold. Figure 1.4b shows an example of the commercial *Biacore T200 system*[8]. Biacore apparatus permits to monitor binding events between molecules ranging from ions to viruses.

SPR is also used for mycotoxin, in particular aflatoxins detection. Several works reported low limits of detections for AFM1 (see Table 1.1) and AFB1 in milk [42, 55, 56].

1.2.3.2 Waveguide based biosensors

Waveguide based optical biosensors represent a large class of detection mechanisms, that includes variety of optical structures, such as interferometers, resonators, etc. The introduction of the waveguides by Colladon dates back to 1842, who experimentally showed that due to total internal reflection (TIR), the light can be guided in a transparent material with refractive index higher than its surrounding environment ($n_{substrate}$< n_{core} >n_{clad}) [57]. By using waveguides, the light path can be simply controlled without the necessity of using bulky components like mirrors or beam splitters (see Figure 1.5a). In particular what is interesting for my work, is that light propagation through waveguides offers excellent possibilities for sensing.

In fact light propagates through the waveguide according to particular patterns of the electromagnetic field, called guided modes [58]. In a slab waveguide the electrical component of the guided mode is given by:

$$\bar{E}_i(x,z,\omega,t) = \bar{E}_i^0(x,\omega) \exp[j(\omega t - \widetilde{\beta}_i z)] , \qquad (1.1)$$

where z is the propagation direction and x is the direction where the refractive index step profile occurs.

---

[6]The picture is from https://goo.gl/WzUdGz.

[7]https://www.gelifesciences.com/en/ae/solutions/protein-research/products-and-technologies/spr-systems

[8]The photo is from https://www.gelifesciences.com/en/ar/shop/protein-analysis/spr-label-free-analysis/systems/biacore-t200-p-05644

The field profile $\bar{E}_i^0$ and the propagation constant $\widetilde{\beta}_i$ of mode *i* are dependent on the light angular frequency ω, the geometry and the refractive index *n* of all the materials (see Figure 1.5b).

Let us define the effective refractive index $\widetilde{n}_{eff}$ of the mode as:

$$\widetilde{\beta}_i = \frac{2\pi}{\lambda}\widetilde{n}_{eff},\tag{1.2}$$

where λ is the wavelength of the propagated light.

In addition, for the certain combination of these parameters, one can achieve monomode waveguiding systems that have only one transverse electric (TE) and transverse magnetic (TM) guided-wave.
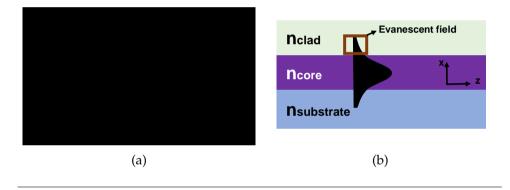
FIGURE 1.5: (a) Schematic of a slab waveguide. The total internal reflection takes place in a waveguide when the $n_{substrate} < n_{core} > n_{clad}$ condition is satisfied. The propagation direction is z. (b) The evanescent field penetrates into the cladding layer, thus becoming sensible to environmental changes.

What is important for sensing is the fact that $\bar{E}_i^0(x, \omega)$ is not to be strictly confined to the core layer, but has exponentially decaying tails in the surrounding materials as well, these are named the evanescent fields. The decay length the evanescent field ranges from one tenth of the wavelength to infinity, depending on the geometry and materials. Nevertheless, there is a large interaction volume of the evanescent field with the surrounding materials. This is used in sensing, since each change in these materials is sensed by the propagating optical modes and can be measured as a change in their

characteristics. In most chemo-optical sensors the sensing action is localized in the cladding region.

As the evanescent field of the guided mode penetrates into the cladding, any refractive index change near to the waveguide surface yields a change of the effective refractive index of the mode. This change is the basic of optical waveguide based biosensors. Therefore, one of the properties of the biosensor, such as the sensitivity, depends on the evanescent field. When used as label-free sensors, the volume of interaction between the analyte and the evanescent field can be very small, and mainly limited by the thickness of the layer of the captured analyte. In the case of molecules of nanometric sizes (like proteins), this means that most of the evanescent tail is unperturbed and does not contribute to the signal, thus the sensor will have a small sensitivity. Simulations can evaluate the dependence of the sensitivity from the thickness of the formed molecular layer [59].

Finally, what makes the use of waveguide based optical biosensors particularly interesting, is the possibility of their integration. In addition, there is a large flexibility in the choice of construction materials and dimensions for waveguides design. In particular, the systems based on silicon wafers are small and robust, thanks to the development of silicon technologies in the last few decades and the possibility of easy and economic fabrication of Si, SiON and Si_3N_4 waveguides.

Different types of waveguide based optical biosensors differ on the way the change in the effective refractive index of the propagating mode is measured. In the following sections, only the two geometries, i.e., interferometers and microring resonators, studied in this thesis are described.

1.2.3.2.1   Interferometers

Waveguide interferometers have particular importance thanks to the smart combination of two very sensitive methods, i.e., the waveguiding and the interferometry techniques, which results in high sensitivity point-of-care biosensors [60, 61]. Significant advantages of these techniques are the high dynamic range and the long interaction length. Two of the most popular types of interferometers for biosensing applications are *Mach-Zehnder* and *Young interferometers (YI)*. Both work on the same principle. A polarized light beam of a coherent and monochromatic source is split into two beams in the device, in order to propagate independently in the two arms of the

interferometer. One of the arms, so called sensing arm, interacts with the sample of interest, i.e., the target solution. The second arm serves as a reference, which either is insulated from the environment or interacts with a reference sample. Any change of the target solution affects the effective index of the mode which, in turn, shifts the phase of the light propagating through the sensing arm, compared to the one of the reference arm. The different phases are measured by the interferometer.

The difference between the two kinds of interferometers is basically the way how the interference of the two beams is recorded. In a *Mach-Zehnder interferometer (MZI)*, the beams are recombined in a waveguide which is interfered to a photodetector, i.e., one output beam is observed. While in a Young interferometers the light exists from the two arms and the interference is observed in the far-field. Figure 1.6 shows the basic design and working principle of (a) MZI and (b) YI respectively.

(a)   (b)
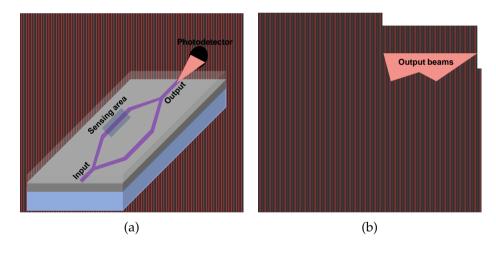
FIGURE 1.6: Typical (a) Mach–Zehnder and (b) Young interferometer configurations. The light coupled into the waveguide structure of the interferometer is split into two beams, which propagate along the sensing and reference arms, respectively. In the case of a MZI, the two beams are recombined by directing them to the same waveguide, resulting in their interference. While the beams of a YI are projected from two closely spaced outputs onto a detector array, where an interference pattern is detected.

Moreover, for increasing the sensing properties of MZI sensors, a configuration based on an asymmetry between interferometer arms is proposed (aMZI) [62].

For the first time, in 1993 Heideman et al. [63] demonstrated a biosensing platform based on integrated MZI. MZI were fabricated on a silicon substrate with a Si_3N_4 waveguide and etched gratings for input/output coupling. Biosensor, immobilized with antibodies, successfully detected human chorionic gonadotropin (hCG). Since then many works have been reported on integrated MZI biosensors [64, 65]. Parallel to integrated MZI, the development of integrated YI was realized. The first demonstration of an integrated YI for sensing was done by Brandenburg and Henninger in 1994 [66]. After that many research papers on YI sensors implementation [67, 68] have been published (see Table 1.2).

1.2.3.2.2 Whispering Gallery Mode Resonators

The *Whispering Gallery Modes (WGMs)* effect in dielectric optics has been investigated since the 1960s [69], however the use of a small WGM resonator for biosensing applications made its first appearance only in recent years [70, 71]. When the light propagates along the closed loop of a waveguide shaped in a ring geometry (named ring resonator), a self-interference takes place, and if the interference is constructive, the field builds up in the cavity. The eigenmodes that satisfy the constructive interference condition are called WGM resonances. The wavelengths of the WGM resonances depend on the geometry of the waveguide and of the ring, as well as, by the effective index of the circulating optical modes. Moreover, it is important to note, that WGM resonators are not only limited to the microring (MRR) geometry [72]. In fact, many other examples of WGM resonators exist made as microdisks[73], spiderweb ring resonator [74], microspheres [75], microtoroides [76] etc. Figure 1.7 shows a few WGM resonator structures.

The WGM has an evanescent field at the resonator surface which senses the binding of biomolecules. WGM resonator based biosensors are, arguably, the most promising competitors to SPR biosensors. They are entirely made with low-loss dielectrics, and for this reason their resonances are sharper and more resolved than that of SPR. In addition, unlike the straight waveguide, the effective light-analyte interaction length of a ring resonator sensor

is no longer determined by the sensor's physical size, but rather by the number of revolutions of the light supported by the resonator, which is described by the resonator quality factor (Q-factor). Q-factor can be defined as the ratio of the light stored in the resonator to the light dissipated per cycle. Due to high Q-factors (>10^6), small molecule ($\approx$50 Da) detection has been experimentally demonstrated. Different proteins, down to a single molecule level [77], have been detected by different configurations with different Q-factors ranging between 10^3 and 10^8. As an example, streptavidin detection has been performed with microspheres [75]. Recently thrombin detection was also carried out by microrings [50].
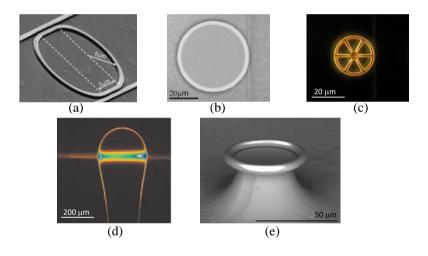
FIGURE 1.7: Various WGM resonator configurations[9]: (a) racetrack resonator [72], (b) microdisks [73], (c) spiderweb ring resonator[74], (d) microsphere [75] and (e) microtoroid [76].

The possibility of miniaturization down to few tens of micrometer in diameter and an easy integrability with photonic waveguides allow the realization of complex systems. Some commercial apparatus based on WGM biosensors are appearing on the market, with up to 128 multiplexed sensing

---

[9]I personally thank Dr. Mher Ghulinyan and Prof. Andrea Armani for providing pictures for Figure 1.7 (c) and (e), respectively

sites (and no cross-talk) as in the case of the Maverick system, from Genalyte[10].

It is fair to underline the importance of integrated WGM resonators in a wide range of applications, such as telecommunication [78, 79], quantum information [80], nonlinear photonics [81, 82] etc., where they play the role of the key component of the system.

Microdisks and microrings are the main configurations used in integrated platforms thanks to the flexibility in terms of size and fabrication materials, even though they suffer from high losses due to the roughness of the surfaces. The light coupling is realized by in-plane or vertically integrated bus waveguides. In contrast to the mentioned configurations, microtoroids and microspheres show an extremely high quality surface smoothness, but they have the disadvantage of being bulky and difficult in integration.

1.2.3.3 Fiber based biosensors

Finally, to complete the overview of optical label-free biosensors, we must mention *optical fiber based sensors*. Thanks to their small size, flexibility, mechanical robustness, mature fabrication techniques and their essential property of light guiding with low losses, these photonic devices are excellent candidates for remotely sensing or for in-vivo biosensing. Fiber Bragg gratings (FBGs), while developed as a tool for the telecommunications, have flourished as a versatile sensor with a wide breadth of applications. They are currently the most popular among all fiber-based optical sensors for analyzing load, strain, temperature, vibration, and refractive index [83]. Particular attention has to be reserved to *long-period gratings (LRG)* sensors, that are demonstrated to be easily manufactured and highly sensitive [84, 85]. The use of LRG in biosensing started mainly in 2000s. In 2007, Chen et al. realized a target DNA sequence detection in real time with an optical biosensor based on a dual-peak long-period fiber grating [86]. Aside from gratings, several other fiber-based technologies have been developed, taking advantage of cost effectiveness and waveguiding capabilities of optical nanofibers. Due to the small dimensions, nanofibers have a very large evanescent field outside the fiber, thus altering measurements of high sensitivity to refractive index changes. Optical structures like MZI [87], coils [88] or ring resonators [89] have been implemented based on nanofibers.

---

[10]https://www.genalyte.com/

<center>(a)   (b)   (c)</center>
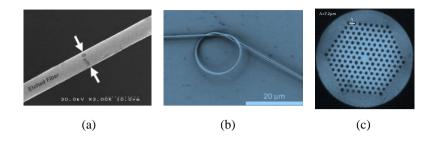
FIGURE 1.8: Fiber based biosensing configurations: (a) FBG on an etched fiber [90], (b) nanofiber loop [91], (c) Photonic crystal fiber based biosensor [92].

Finally, a new type of fibers are used to make hollow fiber biosensors. This type of biosensors is based on a photonic crystal fiber (PCF), which is a fiber with air holes in the cross-section [92]. Two main advantages of this type of biosensors are the fact that air holes in the fiber can act as a simple fluidic channel to deliver the biological samples and that the unique light guiding mechanism of photonic crystal fiber ensures a strong light-matter interaction because of the large light-sample overlap. The array of air holes may hold a few nL/cm sample volumes, making them more desirable tools for biomedical applications. In Figure 1.8 few examples of fiber based biosensors are shown.

1.2.3.4 Comparison of optical biosensors

There are plenty of other techniques, both optical and non-optical, for target molecule detection, but the listed ones are perhaps the most common and studied. In Table 1.2, we put together known optical characteristics of some biosensors in terms of bulk sensing. For bulk sensing we consider the sensor response to an overall change of the cladding material, i.e., when the environmental change occurs near to the surface of the sensor. It is different from the surface sensing which is considered only when the analyte is sensed by the ligand immobilized on the sensor surface. It is clearly visible, that the integrated interferometers or WGM resonators based devices are excellent candidates for a new generation of high sensitive biosensors which came after SPR. While the former table shows the performance of sensors

obtained from the bulk sensing measurements, for a complete understanding of cons and pros of each device, Table 1.3 represents the specific analyte detection limits for various biosensors. Later in this thesis we will compare the state-of-art with our results on label-free biosensors based on integrated SiON microring resonators (MRR) and Si_3N_4 asymmetric Mach-Zehnder Interferometers (aMZI).

TABLE 1.2: Comparison of sensing performances of few optical biosensors in terms of bulk sensitivity (S_b) and bulk limit of detection (LOD_b) measured in refractive index units (RIU).

Sensor platform	LOD_b (RIU)	S_b (nm/RIU)	Q-factor	Reference
SPR	10^{-5} - 10^{-8}	10^4	-	[93, 94]
Long range SPR	9.7×10^{-8}	3.2×10^4	-	[95]
MZI	10^{-6} - 10^{-7}	2×10^4	-	[96]
YI	8.5×10^{-8}	7.5×10^3	-	[97]
SOI microring	10^{-4} - 10^{-7}	70	10^4	[72]
SOI microdisk	5×10^{-4}	26	3.3×10^4	[98]
Microsphere	3×10^{-7}	30	5×10^6	[99]
Opto-fluidic ring	10^{-3}	0.315	-	[100]
FBG	7.2×10^{-6}	404	-	[101]
LPG-PCF	4.42×10^{-7}	2260	-	[102]
Nanofiber	10^{-7}	700	-	[88]

TABLE 1.3: Detection limit of various optical biosensors in case of specific analyte sensing.

Sensor platform	Analyte	Size kDa[11]	LOD nM	Reference
SPR imaging	β2-microglobulin	11.8	1	[103]
SPR	ATP	0.5	0.48	[104]
MZI	Streptavidin	52.8	19×10^{-5}	[105]
MRR	miRNA	7.2	10^{-3}	[106]
FBG	CR protein	0.025	398	[107] [12]

1.3   Motivation to my thesis work

As previously mentioned, the most common and traditional techniques for Aflatoxin M1 detection in milk and dairy products are HPLC and ELISA. They appear to be adequate and well studied for detecting the lowest concentrations of AFM1 defined by the European Commission regulation (EC), i.e., 50 ppt (50 pg/ml) and 25 ppt (25 pg/ml) for adults and infants, respectively. However, these analytical methods require trained personnel and laboratory environment. Moreover, they are time consuming and expensive. This fact encouraged the development of a new, economic, fact and user-friendly biosensing device, that can be run out of specialized laboratories. To this end, a FP7 European project called *Symphony "integrated SYsteM based on PHOtonic microresonators and microfluidic components for rapid detectioN of toxins in milk and dairY products"*, grant number 610580[13] started in 2013. The project consortium has developed a desktop system that incorporates sample preparation and the functions of a small laboratory to detect even very low concentrations of AFM1 in milk (see Figure 1.9). The developed system brings the testing into the dairy.

---

[11] 1Da=1g/mol

[12] In the reference it is reported LOD = 0.01mgL^{-1}. The conversation is done by following: 398 nM = 0.01 mgL^{-1}/25.106g mol^{-1}

[13] Project website: http://symphony-project.eu/

The Description of work [108] of the project states that:

"The objective of the Symphony project is the development of a system for the detection of aflatoxin M1 in milk for the dairy industry. Symphony project will deliver and test in real settings a smart heterogeneous integrated system by the integration of key enabling technologies such as micro-nano-bio-systems and photonics, polymer-based technologies for low-cost microfluidics and Si-based photonic structures".

Thus, the project aims at the realization of a complex system, where the sensor has to satisfy the requirements, of being multiplexed, reusable and suitable for the integration with the rest of the apparatus, together with ultra-sensitive detection limits.
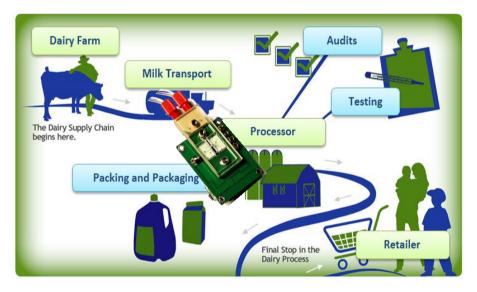

FIGURE 1.9: Milk passes a long way from the dairy farm to the consumer, undergoing time consuming laboratory tests and monitoring. If AFM1 is detected this way in the middle, milk and other products are eliminated. In order to prevent such economical loss, *SYMPHONY* device is developed to be used directly in farms.

The need for an integrated system, with cheap light sources and detectors, motivated the choice of silicon-based CMOS-compatible materials, to be operated at wavelengths in the VIS-NIR range (see Figure 1.10).
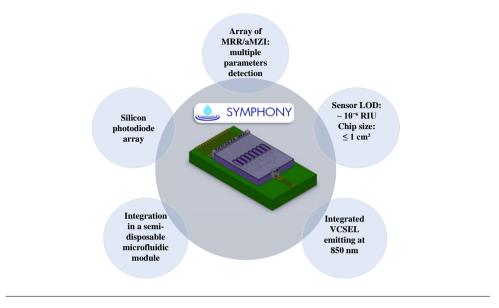
FIGURE 1.10: *SYMPHONY* device key components.

In the introduction it is shown that the Silicon Photonics is arguably one of the most promising technologies for developing highly integrated, miniaturized and multiplexed biosensors. Moreover, the use of silicon nitride, Si_3N_4, and silicon oxynitride, SiO_xN_y, extends the possible range of light guiding and sensing to the visible spectrum. This enables the on-chip integration of silicon-based photodetectors and fast developing VCSELs as a light source. The Nanoscience Laboratory of the University of Trento has had already an experience on investigation of silicon-based waveguides for labeled biosensors realization, operating in the visible range [109]. However the used fluorescence method had many limitations due to the background noise caused by the scattered light, mainly generated at the interfaces of the reaction wells. Therefore, for the further development of a biosensing platforms, resonant WGM cavities and asymmetric MZI (aMZI) were investigated as alternative approaches, which have the potential of being more robust to intensity fluctuation and noise. At the same time, these devices fulfill the required low detection limits.

Motivated by these considerations and requirements, this thesis is devoted to the development and experimental investigation of silicon WGM

microring resonators and aMZI based label-free biosensors for AFM1 detection in real milk samples, as well as to the integration of the *SYMPHONY* device. Moreover, in this thesis, I have studied protein- antibody specific binding using a multi-MRR photonic chip. A comparable to commercially available SPR [110] or photonic crystal microcavities [111] affinity biosensor is investigated for biotinylated BSA - anti-biotin interaction studies.

Chapter 2

Theoretical background

This chapter is dedicated to the theoretical bases of the characteristics of the label-free biosensors that have been investigated in this thesis. First, we will give a definition of the main parameters of any biosensing device, i.e. sensitivity and limit of detection, then the working principles of the transducers, in particular microring resonators (MRR) and asymmetric Mach-Zehnder interferometers (aMZI) are described. Finally, the chapter is concluded with a brief introduction of the biomolecular binding kinetics, the ligand-analyte interaction models, affinity and dissociation constant, as well as the kinetic rate constants calculation methods.

2.1   Label-free biosensing principle

As previously anticipated, the objects of our studies are integrated MRR and aMZI sensors, that are both from the waveguide based biosensor's family. They are both based on the effective refractive index variations taking place near the sensing surface. The former device is based on the shift of the WGMs resonance, while the latter one detects the phase changes in the resulting interference pattern.

Let us start with the basic principles of label-free biosensing. For this purpose, one needs light propagating in an optical waveguide, that guarantees an evanescent field out of the waveguide. A specific ligand needs to be immobilized on the waveguide surface to detect the analytes. Figure 2.1a shows a waveguide coated with antibody as a ligand. The guided light propagates with an effective refractive index n_{eff}. This is a weighted average of the real indexes probed by the propagating optical modes which

depend also on the materials bound on the surface. Usually, each biosensing experiment starts with a buffer flow that passes on the waveguide surface and defines an initial refractive index that is sensed by the evanescent field. We have a constant n_{buffer} refractive index at t_0 when the analyte molecules, accompanied with other biomolecules that can be found in the original analyte solution, arrive to the sensing region of waveguide. These new molecules in fact, are concentrated on the surface of the sensor, replacing pre-existing buffer molecules. This exchange of material produces local variations in the refractive index. Hence, this variation is caused by the material change, but not by the molecular interaction, the refractive index undergoes a bulk change as it is shown in Figure 2.1b. The evanescent field, which decays exponentially in few tens or hundreds of nanometers, is suited to sense this local perturbation, while being almost insensitive to fluctuations far in the cladding. Note that, while designing a waveguide sensor, one has to consider the sizes of ligand and analyte in order to overlap the evanescent field, otherwise no sensing can be performed effectively. Next, the specific binding between the ligand and the analyte takes place. This molecular interaction leads a particular refractive index variation that is specific to the binding reaction (Figure 2.1c). When the index of refraction does not experience anymore variation, i.e., all the binding events have occurred or the surface is saturated, the rinsing and/or the regeneration of the sensor has to be performed. Special solutions particularly chosen for each ligand and analyte are used for this purpose. During the rinsing process all target and non-specific molecules are washed out and the buffer solution is left to flow over the sensing region of the waveguide. This yields a refractive index variation with respect to the initial value. When the sensor regeneration process is completed, not always a complete regeneration of the sensor can be carried out. It can happen, that some molecules of analyte remain attached to the ligands, thus causing a partial recovery of the baseline value of the refractive index (Figure 2.1d). If the sensor reused, this residual signal has to be taken in account during the measurements.

Hence, the optical transducers studied in this thesis are specifically designed to detect the phase shift of the guided light due to the binding of the analyte. This can be accomplished by performing interferometric measurements or by monitoring the spectral shifts of WGM resonances.
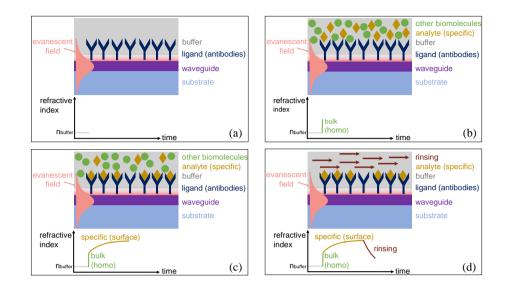
FIGURE 2.1: Schematic drawing of the label-free biosensing approach, when the waveguide is immobilized with ligand, in this case with antibodies: (a) the evanescent field defines a baseline value of the refractive index when the buffer is only present, (b) the bulk variation of the refractive index due to the environment changes near to the waveguide sensing surface, (c) the evanescent field interacting with the captured molecules. The presence of the analyte perturbs locally the refractive index, (d) the rinsing process of the sensor is taking place, thus forcing the refractive index to return to the initial value.

2.1.1   Sensor characteristics

In order to give a preference to one or another sensing mechanism, the comparison between biosensing characteristics needs to be performed. Previously, in Table 1.2 we introduced a bulk *Sensitivity (S_b)* and *Limit of Detection (LOD)* of the sensors. These are parameters that are used in this thesis for characterizing MRR and aMZI biosensors. Sensitivity quantifies the sensor's output signal produced by a unitary variation at the input. It is defined as the ratio of the output signal variation to the refractive index variation n_s of the cladding. The measured output variable in the case of MRRs is the resonance wavelength, λ_0, of an optical resonator [112]. Here, the sensitivity in bulk sensing is given by:

$$S_{b,WGM} = \frac{\partial \lambda_0}{\partial n_s} \qquad (2.1)$$

For the interferometers the measured quantity is the phase ϕ_0 of the interferometric pattern. Therefore, the sensitivity for aMZIs is defined as:

$$S_{b,aMZI} = \frac{\partial \phi_0}{\partial n_s} . \qquad (2.2)$$

In the next sections we will show, that these sensitivities are proportional, through geometrical factors, to the intrinsic sensitivity, which is defined as:

$$S_{b,i} = \frac{\partial n_{eff}}{\partial n_s} . \qquad (2.3)$$

The minimum amount of input that can be distinguished with a certain confidence level is defined to be the *Limit of Detection (LOD)* of the biosensor. It is the smallest signal that can be differenced from the background (baseline) noise. According to the general accepted rule the signal must be at least three times greater than the background noise [113].

When performing biosensing measurements, however, we are more interested in the concentration of the target molecules (analyte) in the so called solvent or buffer solutions. We can therefore distinguish between the measurement limit of detection and the analyte concentration limit of detection (LOD_a).

One method for the background noise calculation is to calculate the mean and standard deviation of multiple readings of the signal in the absence of any analyte, i.e. a signal given by the buffer (blank) solution. According to the rules of statistical analyses, at least 20 readings of the blank have to be performed, but in real experimental conditions it is not always practical to perform multiple blank determinations. In this case, LOD can be extracted from the sensor calibration curve by a regression line, i.e., by the dependence of the signal from an analyte concentration. Here, the analytes are the molecules different from the buffer. Hence the slope of the calibration curve corresponds to the sensitivity of the sensor $S_{b,i}$, thus the LOD_a can be calculated as:

$$LOD_a = \frac{k\sigma}{S_b}, \qquad (2.4)$$

where σ is the standard deviation of repeated measurements of blank solutions. On the other hand, the definition of the instrument LOD_i in terms of the standard error of the regression is:

$$LOD_i = k\sigma + a \, ,\tag{2.5}$$

where a is the intercept of the calibration curve.

The International Union of Pure and Applied Chemistry (IUPAC) recommends the use of k=3, which sets the confidence level to 99,7%.

The LOD therefore carries the influence of instrumental uncertainties, which can arise in any component of the whole sensing system: signal readout unit configuration and detector dark signal, temperature and fluid control, purity of carrier buffers and analyte, laser source, etc. For this reason, the fair comparison of the biosensors can be done considering the Figure Of Merit (FOM) which depends only on the characteristics of the transducer [114]. For WGM sensors with quality factor Q and a spectral full-width at half-maximum $\delta\lambda$, we can define as:

$$FOM = \frac{QS_{b,WGM}}{\lambda_0} \, .\tag{2.6}$$

In some works, authors prefer the use of the "intrinsic LOD", ILOD [98], defined as ILOD = FOM^{-1}. This definition of FOM is also used for SPR or photonic crystal cavity sensors [115]. This parameter for a comparison of the intrinsic performances between (bio-)sensors can be used.

2.1.2 WGM microring resonators

There is a plethora of different designs based on WGMs for biosensing applications. In § 1.2.3.2.2 it was already presented the variety of biosensors both integrated and free space, where the light propagates inside a close loop. Among all configurations, microrings (MRRs) and microdisks are the most convenient for integrated lab-on-a-chip devices being a versatile tool for Silicon Photonics. MRRs depict a ring-shape bent single-mode waveguide, closed on itself. If the waveguide is widened towards the center of the ring, it eventually forms a microdisks, supporting a multi-modal propagation. The modes with grabbing light near the outer edges of the structure will be confined by total internal reflection, and will circulate in a similar

fashion to that of the microring. Thus, we can use a comprehensive model for describing both structures at once [116].

Here we will discuss the simplest coupling mechanism, i.e., light point coupling from the straight waveguide to the ring-shape waveguide (microring resonator) of inner radius R as it is presented in Figure 2.2.
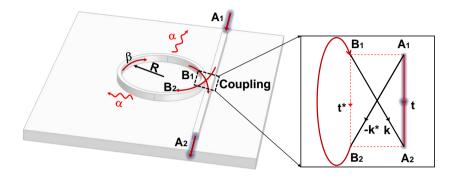

FIGURE 2.2: Schematics of the WGM ring resonator. The field amplitudes in the waveguide and ring are labelled with A and B, respectively. The subscripts label the positions before (1) and after (2) the coupling zone. The field transmission and coupling coefficients are labelled t and k, respectively. The propagation constant inside the ring is β and the radius of the ring is R. Losses are defined by the α coefficient.

The field amplitudes in the waveguide and in the ring are A and B, correspondingly, and the numbering 1 and 2 indicate the amplitudes before and after the coupling zone. The propagation constant along the ring is β, while the field transmission and coupling coefficients are labelled with t and k, respectively, and the * denotes their conjugated complex values. Light propagation inside the ring is affected by losses of different origins. They are categorized as:

- **Absorption losses**, led by the light-matter interaction. In the cladding layer, the absorption of the evanescent field takes place. Both band-to-band or free carrier absorption contribute depending on the wavelength of the light.

- **Radiative losses**, take place due to the finite confinement of the optical mode.

- **Scattering losses**, due to the roughness on the exterior sidewall of the resonator waveguide. This surface scattering is accentuated in bends because the mode is pushed towards the sidewall of the waveguide.

All these losses can be described by a single parameter, named attenuation coefficient $\alpha = \sum_i \alpha_i$, where i means the contributions of surface and bulk absorption, radiation and surface scattering.

In the following, another source of losses related to the coupling will be described. Taking into account these facts, the coupling between the waveguide and the microring resonator can be described by a matrix relation [117]:

$$\begin{pmatrix} A_2 \\ B_2 \end{pmatrix} = \begin{pmatrix} t & k \\ -k^* & t^* \end{pmatrix} \begin{pmatrix} A_1 \\ B_1 \end{pmatrix}, \tag{2.7}$$

with

$$|t|^2 + |k|^2 = 1. \tag{2.8}$$

From the relation 2.8 the field amplitudes before and after the coupling can be described by:

$$\begin{cases} A_2 = tA_1 + kB_1 \\ B_2 = -k^* A_1 + t^* B_1 \\ B_1 = e^{-\alpha \pi R} e^{i2\pi R\beta} B_2 = ae^{i\theta} B_2, \end{cases} \tag{2.9}$$

where a = $e^{-\alpha \pi R}$ and θ = $2\pi R\beta$.

A_2/A_1 gives the waveguide transmission:

$$\frac{A_2}{A_1} = \frac{te^{-i\theta} - a}{e^{-i\theta} - at^*}. \tag{2.10}$$

Consequently, we can calculate the waveguide transmission coefficient T as:

$$T = \left| \frac{A_2}{A_1} \right|^2 = \frac{|t|^2 + a^2 - 2a|t|\cos(\theta + \phi_t)}{1 + |t|^2 a^2 - 2a|t|\cos(\theta + \phi_t)}. \tag{2.11}$$

where ϕ_t is the argument of the complex transmission coefficient t.

Next, the solution of the system for the fraction of the B_1 field coupled into the microring resonator and the input field A_1 is:

$$\frac{B_1}{A_1} = \frac{-ak^*}{e^{-i\theta} - at^*},$$
(2.12)

which allows obtaining the microring cavity intensity build-up I:

$$I = \left|\frac{B_1}{A_1}\right|^2 = \frac{a^2(1 - |t|^2)}{1 + |t|^2 a^2 - 2a|t|cos(\theta + \phi_t)}.$$
(2.13)

One can notice, that both, Eq. (2.11) and Eq. (2.13), are periodic in θ, with a 2π periodicity. Moreover, the microring cavity gets its maximum intensity, i.e., resonates when $cos(\theta + \phi_t) = 1$ or equivalent by:

$$\theta + \phi_t = 2\pi m,$$
(2.14)

where m is an integer number, called the azimuthal mode number. Often ϕ_t is neglected in comparison to θ, since for microrings or microdisks R » β^{-1}, thus leading θ » ϕ_t and taking $\theta \approx 2\pi$ m. Indeed ϕ_t plays a role of a corrector of the resonance spectral position near its intrinsic position. The intrinsic spectral resonance condition can therefore be expressed as:

$$\lambda_m = \frac{2\pi R}{m} n_{eff},$$
(2.15)

where n_{eff} is the effective refractive index of the resonator mode. It is important to mention, that the exact calculation of n_{eff} is not trivial. It depends on the wavelength and on the geometrical details of the resonator and can be calculated both analytically or modelling. Considering known n_{eff}, the transmission spectrum can be easily simulated by using Eq. (2.12). An example of a simulated transmission spectrum is reported in Figure 2.3a.
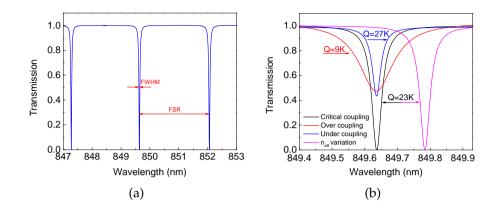
FIGURE 2.3: (a) Simulated spectrum of a critical-coupled WGM resonator. (b) Comparison of the resonance of WGM resonator when, respectively, a critical (Q=23K), over (Q=9K) and under (Q=27K) coupling takes place. In addition, pink line shows the resonance shift due to a n_{eff} refractive index variation.

In the transmission dips are periodically appearing due to the resonant coupling with the microring resonator. The periodicity, i.e., the spacing between neighbor resonance deeps, is called Free Spectral Range (FSR), and can be calculated from Eq. (2.15) as:

$$FSR \approx \frac{\lambda^2}{2\pi R n_g}, \tag{2.16}$$

where n_g is the group index:

$$n_g = n_{eff} - \lambda \frac{\partial n_{eff}}{\partial \lambda}, . \tag{2.17}$$

The Extinction Ratio (ER) that described the efficiency of the transmission, can be obtained by the value of the transmission at resonance:

$$ER^{-1} = T(\lambda_m) = \frac{(a - |t|)^2}{(1 - a|t|)^2} . \tag{2.18}$$

Therefore, when $|t|$ = a, ER becomes infinite and the transmission vanishes. This means, that all the input light is coupled to the microring resonator. This condition is named critical coupling and when it is satisfied the light in the cavity interferes perfectly and destructively with the light transmitted in the waveguide, causing drops to zero in the transmission. However, there are two other cases, i.e. over-coupled ($|t| <$ a) and under-coupled ($|t| >$ a) regimes, where the resonance takes place, but the transmission does not vanish. All three possibilities are shown in Figure 2.3b.

Next, the *Quality factor Q* of a resonance is defined as the ratio of the energy stored in the resonator to the energy consumed per cycle by damping processes, consequently it is connected with resonator losses. The losses define the finite width of the resonances as well. Thus, we can define the Q-factor as:

$$Q = \frac{\lambda_0}{\Delta\lambda_{FWHM}} .$$

(2.19)

Note that, in comparison with the critical coupling case, the Q-factor is lower for over-coupling and higher for under-coupling regimes.

The measured value of the Q-factor can be expressed as [118]:

$$Q_l^{-1} = Q_c^{-1} + Q_0^{-1} ,$$

(2.20)

where Q_l is the loaded (measured) quality factor, Q_0 is the intrinsic quality factor, given by the losses of cavity (radiation, surface scattering, absorption), and Q_c is the contribution of the coupling. In the same work, i.e., [118], the authors calculated the coupling Q-factor, considering the results by Spillane et al. [119]. For Q_c they got:

$$Q_c^{-1} = \frac{2Q_l^{-1}}{1 - \sqrt{T_{min}}} ,$$

(2.21)

where T_{min} is the minimum of the measured transmission spectra at the resonance. In critical coupling, T_{min}=0, thus $Q_c = 2Q_l$ and $Q_l = \frac{1}{2}Q_0$. Finally, the relationship between intrinsic Q-factor and the attenuation coefficient α is:

$$Q_0 = \frac{2\pi n_g}{\lambda\alpha} .$$

(2.22)

In the following discussions we will use Eq. (2.19) to measure the Q-

factor. Finally, for the MRR based biosensors the sensitivity and the limit of detection given by Eq. (2.1) and Eq. (2.4), respectively, will be used.

2.1.3   Mach-Zehnder interferometers

The second device, that has been studied in this thesis is asymmetric Mach-Zehnder interferometer (aMZI). First, we will discuss in general MZI, then will show the advantages of the asymmetric configuration. If in the case of WGM resonators we deal with self-interfering light in a ring-shape closed loop, here the interference happens by dividing and recombining light. A schematic representation of such configuration is shown in Figure 2.4.
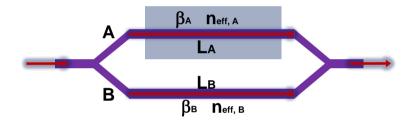

FIGURE 2.4: Schematic of a Mach-Zehnder Interferometer in a biosensor configuration. The splitted light amplitudes in the two arms are labelled with A and B, respectively. The effective refractive indexes, $n_{eff;A/B}$, are different in the two waveguides, leading to different propagation constants. The interaction lengths on both arms are, respectively, L_A and L_B.

A beam splitter located immediately after the input waveguide splits the light beam into two parts, which propagate along two waveguides forming an interferometer arms. After crossing the arms, the two beams are recombined by a second beam splitter. The measured variable in this system is the transmitted intensity which is strongly dependent on the relative phase of the two beams at the second beam splitter. Here, L_A and L_B are called interaction lengths, the propagation constants and effective refractive indexes are labelled as $\beta_{A/B}$ and $n_{eff;A/B}$, for sensing and reference arms, respectively.

The Mach-Zehnder is a favored configuration among interferometric devices particularly for biosensing purposes, thanks to an easy accessible reference arm that minimized external variations, such as temperature change or mechanical vibrations [63].

The sensing principle, as for any other waveguide based biosensor, is based on evanescent field interaction with the material near to the waveguide surface, in the sensing arm of MZI, leading to an effective refractive index changes. The latter affects the phase difference. The phase difference is then:

$$
\begin{aligned}
\phi_{AB} = \phi_A - \phi_B = \beta_A L_A - \beta_B L_B = \\
= \frac{2\pi}{\lambda}(n_{eff,A}L_A - n_{eff,B}L_B).
\end{aligned}
\tag{2.23}
$$

Considering the light recombination on the second beam splitter lossless, then the interference of the light leads to a transmission:

$$
T = \frac{1}{2}[1 + cos(\phi_{AB})].
\tag{2.24}
$$

In biosensors based on interferometric devices, the detection of the phase shift is realized by monitoring the transmission spectrum at a certain fixed wavelength (see Figure 2.5).
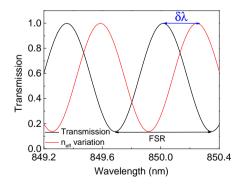

FIGURE 2.5: Transmission spectra of a MZI (black line). The red line shows the transmission spectra shift due to a n_{eff} refractive index variation.

The spacing between adjacent peaks of the MZI intensity response is called Free Spectral Range (FSR).

If we assume that the arm A is exposed to a sensing liquid and the arm B is protected by a cladding layer, an estimate of the bulk sensitivity we can be obtained the:

$$S_b = \frac{\partial T}{\partial n_A} = -\frac{sin(\phi_{AB})}{2}\frac{\partial \phi_{AB}}{\partial n_A} = -\frac{\pi L_A sin(\phi_{AB})}{\lambda}\frac{\partial n_{eff,A}}{\partial n_A}. \qquad (2.25)$$

The sensitivity of a MZI can be optimized by increasing the L_A interaction length.

When the two arms of the interferometer have the same effective refractive index and optical path length, so called balanced MZI, it is hard to detect a phase variation. Therefore, it is better to use other MZI geometries which optimize the sensitivity.

2.1.4 Asymmetric Mach-Zehnder interferometers

To achieve a high sensitivity, one way is to artificially increase the phase difference. This is done in an asymmetric design of MZI (aMZI). aMZI consists of inequivalent, i.e., unbalanced arms as a result of the removal of the cladding and of an additional path length introduced in only one of the arms [62]. An additional path length can be added to the reference arm, as well as the width of the waveguides in the sensing and reference arms can be designed differently [120]. Each of these techniques contributes in increasing of the sensitivity by affecting the phase delay. The efficiency of the configuration will be maximized if both these contributions converge together, thus ensuring the transmission at the output port being wavelength-dependent. Figure 2.6 represents an aMZI configuration.
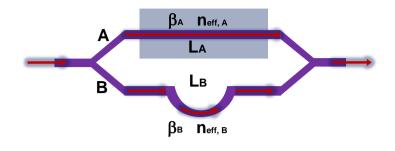
FIGURE 2.6: Schematic of an asymmetric Mach-Zehnder Interferometer in a biosensor configuration. The sensing window is present only on the upper arm of aMZI, while the second arm has an additional length. The interaction lengths on both arms are, respectively, L$_A$ and L$_B$.

If we assume that the wavelength scan is performed in a small range ($\delta\lambda$) starting from a given wavelength (λ_0), then the phase difference accumulated by the light during the propagation in the two arms ($\phi_{AB}(\lambda)$) is:

$$\phi_{AB}(\lambda) = \phi_{AB}(\lambda_0 + \delta\lambda) \approx \frac{2\pi}{\lambda_0}(n_{eff,A}L_A - n_{eff,B}L_B)(1 - \frac{\delta\lambda}{\lambda_0}) =$$
$$\phi_0 - \frac{2\pi\delta\lambda}{\lambda_0^2}(n_{eff,A}L_A - n_{eff,B}L_B)\,, \tag{2.26}$$

where

$$\phi_0 = \frac{2\pi}{\lambda_0}(n_{eff,A}L_A - n_{effB},L_B)\,, \tag{2.27}$$

By defining $\Lambda = \lambda_0{}^2/(n_{eff,A}L_A\text{-}n_{eff,B}L_B)$, we can straightforwardly compute the transmission spectrum of the aMZI as:

$$T(\lambda_0 + \delta\lambda) \cong \frac{1}{2}[1 + \cos(\phi_0 - \frac{2\pi\delta\lambda}{\Lambda})]\,. \tag{2.28}$$

Λ defined by this way, plays the role of the FSR [121]. In order to make Λ arbitrarily short one can increase the optical path difference between the two arms. Reducing the FSR, the steepness of the curves of the transmission

spectrum and the number of visible peaks (and valleys) in a given wavelength range increase. Therefore, Λ sets the intrinsic resolution for the measurement of the phase $\phi_{AB}(\lambda)$.

$\phi_{AB}(\lambda)$ is measured via a sinusoidal fit of the transmission spectrum, and, from its variation, changes in the refractive index n_A are measured once other parameters are known. The bulk sensitivity (S_b) is computed as:

$$S_b = \frac{\partial T}{\partial n_A} \simeq \frac{\partial \phi_0}{\partial n_A} = \frac{2\pi L_A}{\lambda_0} \frac{\partial n_{eff,A}}{\partial n_A} , \qquad (2.29)$$

Moreover, S_b is independent from the actual ϕ_0 value, thus giving the possibility to increase S_b by choosing a longer L_A. In addition, in the design of the aMZI we can construct waveguides of any shape, i.e., straight, curved or spiral, thus increasing the sensing area and the resolution of the sensor. However, there is always a limit for the device dimensions, since the absolute intensity and the visibility of the interference fringes depend on the propagation loses which increase if the aMZI arms are too long. Hence, the ultimate LOD of the system is highly depending on the operation points of the device, i.e., the total interaction length and the sensitivity of the system, as well as the perturbations due to the liquid non-homogeneous distribution in the large sensing area.

2.2   Binding kinetics

The last section of this chapter is dedicated to the molecular binding models and to the introduction of binding characteristics of a biosensor, like affinity, dissociation constant, association and dissociation rate constants.

Label-free affinity biosensors are widely used for monitoring and analyzing the biospecific interaction between immobilized ligand and dissolved analyte. The characterization of antibody affinity and kinetic studies of antibody-antigen reactions are needed to select the appropriate reagents for immunoassay. Hence, kinetic analysis are performed to characterize the reversible, non-covalent binding in terms of binding strength and speed. As any binding mechanism, non-covalent binding is affected by several contributions, such as hydrogen bonds, ionic/electrostatic interactions, van der Waals forces, and finally hydrophobic effects [122].

Let us to describe the steps of the recognition reactions. Once the ligand is immobilized on the surface for the selective binding of its antigen, i.e., analyte, the specific recognition and binding is supposed to occur. Each reaction consists of two phases, i.e. association and dissociation, where the former shows how fast one molecule binds to another by forming complexes, and the latter points to the speed of the complex destruction. If the biomolecular system is left to incubate for a certain time, it will reach en equilibrium and the rate of complex formation and destruction will be the same. Thus the number of bound and unbound molecules will be constant.

Dissociation phase depends on the complex strength, that is conditioned by the binding affinity, giving an information on the complex formation in equilibrium.

The binding depends on the dimensions of the reacting molecules, as well as on the presence of disturbing non-specific molecules, thermal influence, etc. The influence of non-specific binding can, in fact, disturb a measurement, giving a fake information about signal levels, causing incorrect estimation of affinity constant. When the functionalization of the sensor, i.e., ligand immobilization, is performed, the process is realized to minimize non-specific interactions.

Finally, the molecular binding events are followed by the sensorgrams, which refers to the time dependence of the signal shift (resonance wavelength, phase, angle, etc.). The characteristics of the molecular reactions can be extracted from the fit of the sensorgrams. Several models exist to describe the molecular system. Therefore, here we will briefly discuss three of them, i.e., 1:1, heterogeneous and mass transport. Note, that the molecular interaction studies presented in this thesis are based on the 1:1 model only.

2.2.1 1:1 Binding model

Let us describe the mechanism of getting an information about the molecular interactions from the effective refractive index changes near to the sensor surface.

At a given time, the sensor response R, which is the resonance shift in case of MRRs or the phase shift for aMZI, can be approximated by the sum of four contributions:

$$R = R_R + R_L + R_A + R_{ns}, \tag{2.30}$$

where R_R is caused by the refractive index of the sample buffer, R_L due to refractive index change caused by immobilized ligand, R_A due to analyte bound to immobilized ligand and R_{ns} due to nonspecific binding. Therefore, the rate of change of R is:

$$\frac{dR}{dt} = \frac{dR_R}{dt} + \frac{dR_L}{dt} + \frac{dR_A}{dt} + \frac{dR_{ns}}{dt} \,. \tag{2.31}$$

Since the composition of the buffer solution is constant during the experiment, then dR_R/dt=0. Moreover, the ligand is anchored at the sensor surface by the covalent bonds or by the disulfide bonds, no ligand leakage is assumed to take place, thus dR_L/dt=0. And, finally, we consider that the ligands are specific to the target molecules and no non-specific binding events occur, therefore dR_{ns}/dt=0. Under these hypothesis, the sensorgram shows only the sensor response due to the analyte binding. Thus:

$$\frac{dR}{dt} \sim \frac{dR_A}{dt} \,. \tag{2.32}$$

Let us suppose that the ligand L and the target molecule A bind reversibly in solution to form a binary complex AL. Here, we will discuss the case when the L ligand has only one single binding site. This binding model represents a simple 1:1 interaction.

$$L + A \underset{k_{off}}{\overset{k_{on}}{\rightleftharpoons}} LA \,, \tag{2.33}$$

where k_{on} is the second-order rate constant for complex association and k_{off} is the first-order rate constant for complex dissociation. The rate of complex formation depends on the free concentration of A and L ([A] and [L] correspondingly) and on the stability of the complex:

$$\frac{d[AL]}{dt} = k_{on}[A][L] - k_{off}[AL] \,. \tag{2.34}$$

Therefore, the concentration of complex [AL] is identical to the concentration of bound analyte and, consequently, is proportional to the response R_A. The free ligand concentration [L] is the difference between the total

and the bound ligand concentrations. The maximum response due to ana-
lyte binding, R_{max} will therefore be proportional to the total ligand concen-
tration and (R_{max}-R_A) will be proportional to the free ligand concentration.
The free concentration of the analyte continuously flowing over the sensor
may be considered constant and identical to the total analyte concentration,
C. With these assumptions Equation (2.34) can be written in the following
form:

$$\frac{dR_A}{dt} = k_{on}C(R_{max} - R_A) - k_{off}R_A =$$
$$= k_{on}CR_{max} - (k_{on}C + k_{off})R_A. \tag{2.35}$$

The system reaches an equilibrium after leaving for a long time. Eventually
the binding interaction reaches a point where association and dissociation
rates compensate each other. At this point the level of signal reaches a con-
stant value $R_A = R_{eq}$. Thus, the association equation can be written as:

$$\frac{dR_A}{dt} = k_{on}CR_{max} - (k_{on}C + k_{off})R_{eq} = 0. \tag{2.36}$$

The solution of the differential Eq. (2.35) with the boundary condition 2.36
is:

$$R_A(t) = \frac{k_{on}C}{k_{on}C + k_{off}}R_{max}[1 - exp(-(k_{on}C + k_{off})t)] =$$
$$= R_{eq}[1 - exp(-(k_{on}C + k_{off})t)]. \tag{2.37}$$

Introducing a new parameter:

$$k_{obs} = k_{on}C + k_{off}, \tag{2.38}$$

the Eq. (2.37) can be rewritten as:

$$R_A(t) = R_{eq}[1 - exp(-k_{obs}t)], \tag{2.39}$$

where R_{eq} is the response at equilibrium and k_{obs} is the experimentally
determined value of the pseudo-first-order rate constant for approach to
equilibrium. By fitting the sensor response with Eq. (2.39), we can extract

the values for R_{eq} and k_{obs}. Doing the same for different analyte concentrations it is possible to obtain a linear dependence for k_{obs} values on the C concentration. The linear fit of this dependence should then yields a slope equal to k_{on} and an intercept equal to k_{off}.

The equilibrium dissociation constant for the complex is defined as the ratio of k_{off} and k_{on}:

$$K_D = \frac{k_{off}}{k_{on}}. \tag{2.40}$$

The affinity K_A of analyte molecules is inversely proportional to the K_D value.

Sometimes this method for K_D calculation yields significant uncertainties due to the exponential fit. Therefore a different approach can be used for the equilibrium analyses, based on Langmuir isotherm [49, 123]. For different concentrations C of the analyte the measured response R_A is described by:

$$R_A = \frac{R_{max}}{\left(1 + \frac{K_D}{C}\right)}. \tag{2.41}$$

The values of K_D and R_{max} can be determined by fitting R_A as a function of C concentration with Eq. (2.41).

Note, that equilibrium and saturation are different phases. The relationship between R_{eq} and R_{max} is in direct dependence to the analyte concentration C relative to K_D. For instance, if we take a $C = K_D$, we will get R_{eq} = 0.5 R_{max}, i.e., 50% of possible maximum signal. Normally, R_{max} is generally observed, if $C > 10K_D$ condition is satisfied.

Finally, in the dissociation phase, the analyte concentration is suddenly reduced [A]=0 by injecting the running buffer. The response of the sensor follows an exponential decay. Hence, no complex formation takes place in this phase, from the Eq. (2.34) we will get:

$$\frac{d[AL]}{dt} = -k_{off}[AL] = 0, \tag{2.42}$$

which yields to:

$$\frac{d[R_A]}{dt} = -k_{off}R_A(t). \tag{2.43}$$

Considering the fact, that the dissociation starts from the R_{eq} signal level, the solution of the differential equation 2.43 is:

$$R_A(t) = R_{eq}exp(-k_{off}t). \tag{2.44}$$

Figure 2.7 shows a typical sensorgram starting with a baseline, corresponding to buffer, i.e., analyte is missing, then an analyte is inserted and an association follows there, the signal increases according to Eq. (2.39). Next, an equilibrium is achieved and the signal remains stable. Then the analyte is removed and the buffer is flown again. This last part of the sensorgram corresponds to the dissociation described by the Eq. (2.44).
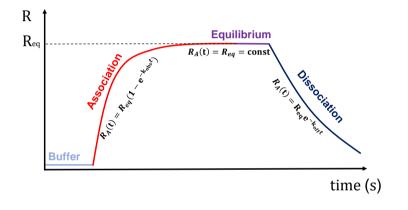

FIGURE 2.7: Example of a sensorgram showing an initial baseline, where the analyte is missing, an increase of the signal due to the association phase, an equilibrium, corresponding to the constant signal and, finally, a decrease of the signal during dissociation.

2.2.2 Heterogeneous Binding model

The 1:1 model is an ideal case and not always suites for more complex systems. Let us introduce the 2:1 heterogeneous ligand model, that assumes a single analyte binding at two independent ligand sites simultaneously. Each ligand site binds the analyte independently with a different rate constant. In this case the reactions will be the followings:

$$\begin{cases} L_1 + A \xrightleftharpoons[k_{off1}]{k_{on1}} L_1 A \\ L_2 + A \xrightleftharpoons[k_{off2}]{k_{on2}} L_2 A \,, \end{cases} \tag{2.45}$$

where, as before, A is the analyte and L represents the immobilized lig- and. This molecular behavior is typical for small dimension ligands and, respectively, big analytes. Alternatively it can describe the case when the ligands are too dense on the surface and some overlap happen. Since each ligand react with only one analyte, this model can be assumed as a combi- nation of two 1:1 models. The fit function will be the same of two Eq. (2.39), adding a parameter to account for the percentage of the binding contributed by each interaction. This model is useful if we record a sensorgram with an association phase, which shows an initial fast on-rate followed by a slower on-rate. This will cause a signal continuous increase, rather than an equilib- rium. While in the dissociation phase, an initial fast dissociation is followed by a slower off-rate, with the higher concentration curves that do not permit to recover baseline as it is represented in Figure 2.8 with the red line.
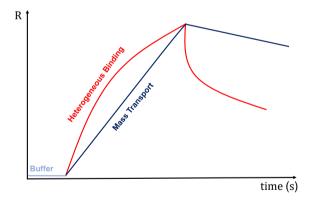

FIGURE 2.8: Examples of sensorgrams for the heterogeneous (red) binding and mass transport (blue). Heterogeneous binding is characterized by biphasic curves that do not reach equilibrium and often do not return to baseline sig- nal in the dissociation. Mass transport limited curves are usually represented by straight lines.

2.2.3 Mass Transport model

We conclude this section with the description of the mass transport model which can be applicable when the analyte molecules flow over the biosensor surface via laminar flow. Hence, the frictional forces from the sides of the tubing and the surface of the biosensor slow the velocity of the liquid close to the surface. This decreases the flow rate on the sensor site, distracting efficient exchange of analyte molecules from the surface to the bulk solution. Here, the binding rates depend on the supply of analyte molecules rather than the kinetics of biomolecular interactions. Moreover, at low concentrations, the binding between the ligand and the analyte molecules, near the biosensor surface, can occur faster than the analyte replacement in the surrounding solution. The shape of the binding curve is determined by the analyte diffusion rate. It is clear, that flow rate plays a crucial role in such systems. Basically, it adjusts the analyte molecules diffusion on the sensor surface, consequently the binding kinetics. Mass transport model is explained by the following expression:

$$A_{bulk} \underset{k_m}{\overset{k_m}{\rightleftharpoons}} A_{surf} + L \underset{k_{off}}{\overset{k_{on}}{\rightleftharpoons}} LA \,, \tag{2.46}$$

Often mass transport limited curves appear as straight lines as it is shown in Figure 2.8 with a blue line [122]. The model for mass transport limited data analyses is built on two fundamental steps, i.e., the rate of analyte transport from the bulk solution to the surface (k_m), and the interaction of the analyte with the ligand. When k_m is much smaller than $k_{on}[A]$, then the limitation caused by diffusion, can be significant. One way to reduce the mass transport effect, is to increase the analyte concentration and to reduce the number of immobilized ligands. Increasing the flow rate also will eliminate effects of the phenomenon.

Chapter 3

Experimental apparatus

The development of a biosensing system that is able to sense

- the smallest changes of the liquid environment near to the sensing surface,

- the binding of biomolecules of few hundreds of Da molecular weight,

and that is able to give repeatable results is a complicated task. A part from the sensor itself, there is a number of critical points to be considered:

- the stability of of intensity, polarization, wavelength and temperature of the laser source,

- the mechanical stability of the light coupling system,

- the temperature stability of the sensor, sensing liquids as well as of the environment,

- the alignment of the flow-cell with the sensor chip, insuring a homogeneous flow and the absence of leakage of flowing solutions,

- the minimization of electrical noise in the readout system,

- the reproducible and efficient coverage of the sensor (surface functionalization) with the specific receptors, i.e. aptamers and antibodies.

During my PhD I worked with different biosensing devices demanding different approaches for sensing measurements, that is why in this thesis, different experimental setups have been implemented. In this chapter, all

the different schemes used for the aMZI and MRR based biosensors development are presented. Figure 3.1 shows a general setup of the experiments. The main difference between setups is related to the chip design and, consequently, to the coupling methods. Next we will present for each setup the appropriate image.
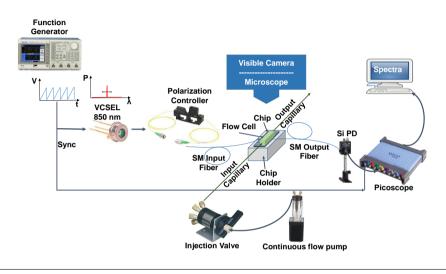

FIGURE 3.1: Schematics of the experimental setup.

3.1 Chip design

First, the design and characteristics for the sensor platforms that have been used for AFM1 detection in buffer as well in milk solutions within the *SYMPHONY* project and for the anti-biotin sensing measurements will be presented. For the first, two sensors based on integrated microring resonators and asymmetric Mach-Zehnder interferometers were designed and fabricated. All sensing measurements were performed in UNITN, while antibiotin related experiments were performed in Lionix International on the third sensor design. All the three chip designs consider the actual laser tuning range to cover the range of at least two FSR-s.

3.1.1   Microring resonators for *SYMPHONY*

The first sensor configuration is the *SYMPHONY* sensor based on MRRs, which was developed by D. Gandolfi and A. Samusenko. For the fabrication of the microring resonators, in FBK a Plasma-Enhanced Chemical Vapor Deposition (PECVD)for SiO_xN_y deposition is used. SiO_xN_y is transparent at 850 nm. This material demonstrates several properties, that allow to vary refractive index of the dielectric material between 1.45 (n_{SiO_2}) and 2 ($n_{Si_3N_4}$) by changing the relative amount of nitrogen and oxygen atoms, that, from the other hand, influences on the optical scattering and reduces losses, by relaxing the strain at the silica-SiON boundaries, while keeping a high refractive index contrast with silica cladding. Deposition is realized on 6-inch 625 μm thick c-Si wafers with a 4 μm thick buffer oxide layer. Fabricated SiON film thicknesses are 305 nm and 350 nm respectively for BS2 and BS3 wafers, with 1.66 refractive index. Both thickness values are measured after a thermal treatment at $1050°C$. The SiON waveguide circuit, consisting of waveguides, splitters and racetrack resonators with 100 μm radius, is realized with UV-photoli-thography and reactive ion etching. Then, the SiON is covered by a 1 μm thick cladding layer in silicon dioxide (SiO_2). The sensor sites are defined by opening a 20 μm-wide window on top of the ring resonators using a combination of reactive ion etching and chemical etching. The gap between the 1 μ-wide ring waveguide and 0.9 μ-wide bus waveguide in the 35 μm-long coupling region is 0.6 μm. The two different waveguide widths are due to phase matching the modes in the coupling region. On the chip, the signal from the input waveguide is coupled to four MRRs by directional couplers. The design of the sensor is shown in Figure 3.2.

(a)

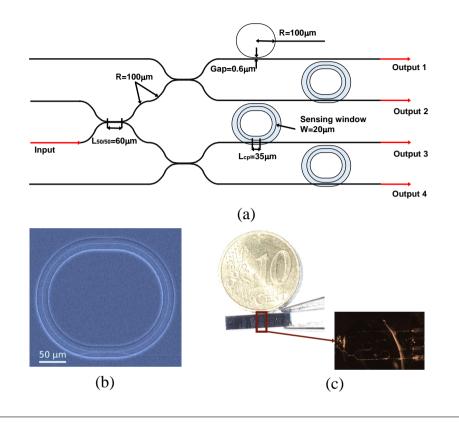(b)   (c)

FIGURE 3.2: (a) Sketch of the microring resonator chip, (b) SEM image of the single MRR, (c) photograph of the chip and a one euro-cent coin for size comparison and a zoomed microscopic view of the chip illuminated with VCSEL. A drop of water is added on the chip.

3.1.2 Microring resonators for anti-biotin sensing

The second design of MRR-based chips are realized and manufactured in LioniX International BV by means of the TriPleX technology [124]. A 4 inches 525 μm thick silicon substrate is oxidized to form a 8 μm thick thermal oxide layer. Then, a 103 nm thick LPCVD (low-pressure chemical vapor deposition) Si_3N_4 layer (refractive index: 2.02) is deposited onto the thermal oxide followed by a thin LPCVD SiO_2 cladding layer. This layer stack is patterned by using photolithography, dry etching (RIE) and, subsequently, resist removal. The waveguides were, then, covered with a further

6 μm thick LPCVD SiO$_2$ cladding. In order to enable interaction between the waveguide evanescent field and the liquid sample of interest, the top (SiO$_2$) cladding is locally removed by opening the sensing windows. This is accomplished by a photolithography step and BHF wet etch down to the Si$_3$N$_4$ waveguide core layer. All chips fabricated in LioniX are designed in a way to guarantee propagation losses below 0.1 dB/cm and in order to ensure bending losses below 0.01 dB/90° bending radii >100 μm are used. The design of the sensor is shown in Figure 3.3.
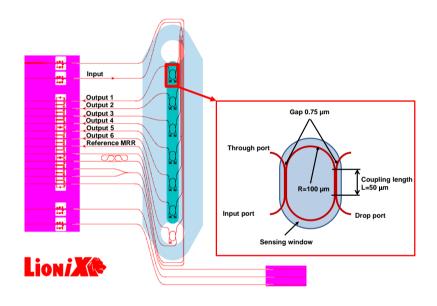

FIGURE 3.3: Sketch of the microring resonator chip; (inset) Design of the single MRR: it consists of a racetrack shaped microring with radius 100 μm, coupling length 50 μm, gap 0.75 μm. Waveguide width is w=1.0 μm.

3.1.3   Asymmetric Mach-Zehnder Interferometer

Another sensor design for *SYMPHONY* project based on aMZI was realized and fabricated by LioniX International BV based on the TriPlex technology

[125]. The same fabrication process as it was described in the previous section, has been used for multi-aMZI chips. A sketch of the sensor is reported in Figure 3.4. Eight aMZI are integrated in a single chip. Four of them (upper part of the design) have opening windows on both arms, while the other four aMZIs (bottom ones) have opening windows only on one arm thus increasing the phase difference between the light on both arms. This makes such device more sensible for environmental changes.

Sensing window S=640×660 µm²
ΔL=640 µm
Output 4
Output 3
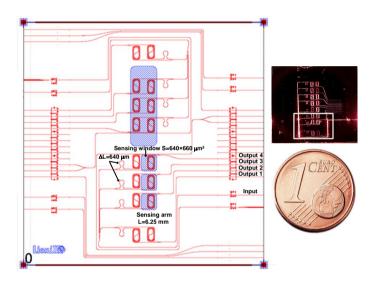Output 2
Output 1
Input
Sensing arm
L=6.25 mm

FIGURE 3.4: (left) Sketch of the asymmetric Mach-Zehnder Interferometer based chip; (right)photograph of the chip and a one euro-cent coin for size comparison. White square encloses the aMZIs on the chip that were used for the measurements.

A same input signal is sent to the four aMZI by a one to four channel splitter. The long optical path length of the sensing arms is L=6.25 mm, and it is achieved by a spiral waveguide to minimize the footprint. The difference in optical path-length determines the FSR of the aMZI and is chosen such that it matched the bandwidth of the used Vertical-Cavity Surface-Emitting Laser (VCSEL). Three out of the four aMZI have the sensing window on top of the sensing arm. Openings are shown in the Figure 3.4 by blue hatched regions. The fourth aMZI is left covered by the cladding in

order to isolate it from the microfluidic chamber and, therefore, to be used as the reference sensor (baseline sensor). This aMZI is used as an internal reference both for the input signal intensity (e.g. to control the VCSEL fluctuations) and for temperature. The area of and pitch between the sensors are chosen such that each individual sensor can be functionalized by a spotter with a different chemistry allowing internal consistency tests or multianalyte detection. Note that the input and output waveguides are all on the same edge of the chip.

3.2   Optical setups

In this section the key components of the optical setups will be described.

3.2.1   VCSEL at 850 nm

For the all experiments, presented in this thesis a VCSEL diode laser is used. In particular it is a VCSEL diode U-L-M Photonics ULM850-B2-PL-S0101U, which is sold as bare-die, and can be bonded with a flip-chip method directly at the input of the waveguides. Moreover, these VCSEL diodes are single mode, polarization maintaining and can be tuned in wavelength by more than 1.6 nm, by changing the driving current. During the wavelength tuning, the probability of experiencing a mode-hop is low, because the vertical cavity is very short and, consequently, the FSR is large.

An optical setup based on fiber coupling was developed (see § 3.2.2), where the VCSEL source was the same, but in a TO46 can, ULM850-B2- PL-S46FZP that helps during pigtailing process for handling glue inside. The pigtailing of the VCSEL diode was performed at UNITN. The output beam from the laser diode is circular, and by aligning a single-mode optical fiber (see Figure 3.5a), I was able to achieve almost 55 % optical fiber in butt-coupling efficiency (the fiber Mode Field Diameter (MFD) was 5 μm). Once the correct position of the fiber is found, a small drop of UV-curable glue is placed on its tip. This curing of the glue is done with a UV-curing LED system first with low powers (20 mW) for 30 seconds for couple of times in order to avoid fast crystallization of glue that can cause fiber misalignment. Once glue is hard and the fiber is stable, we use a high power (120 mW) illumination for 5-6 minutes for final fixing the fiber in his position. To increase

the mechanical stability of the bonding, an additional drop of epoxy glue is put into the TO46 can, filling the empty volume. For better protection of the fiber from bend tensions on the glued point, a short piece of shrinking tube is wrapped around the assembly.
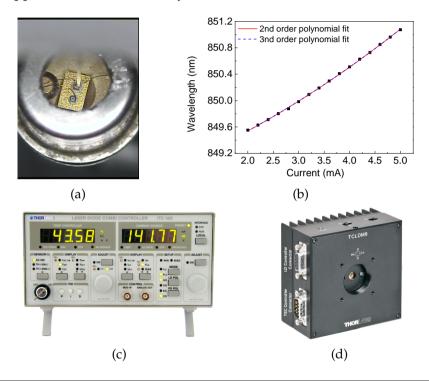

(a)

(b)

(c)

(d)

FIGURE 3.5: (a) Microscope picture taken during the fiber pigtailing of the VCSEL source. (b) Calibration of the lasing wavelength of the VCSEL, as a function of the driving voltage. The wavelength has been measured with an Optical Spectrum Analyzer (average uncertainty 5 pm), (c) ITC502 - Laser Diode/Temperature Combi Controller, (d) TCLDM9 - TE-Cooled Mount.

From a commercial 2 mW laser diode, a maximum output power from the pigtailed fiber of 1.1 mW was achieved. This way pigtailed VCSELs output power is very stable in time that yields the stable alignment of the fiber.

To drive the VCSEL, the current has to be in the range from 2 mA (lasing threshold) to 6 mA (damaging threshold, output power 2 mW). This range is

too small to be accurately tuned by most of the commercially available laser drivers. In fact in NanoScience Laboratory we have a Laser Diode/Temperature Combi Controller, but only the part of temperature controller was suitable for our system. To overcome this problem, we connected the laser in series with a resistor of R = 550 Ω, and we drove it directly by setting the voltage with a function generator.

Figure 3.5b shows the calibration curves for the emission wavelength, measured with an OSA, as a function of the driving voltage. We fit the data with second and third order polynomial functions. One can see that even the second order is sufficient. From the fitting coefficients in the sensing experiments we extract the emission wavelength by measuring the driving voltage.

In order to keep stable the laser temperature, we used a temperature controller[1] (see Figure 3.5c) connected to the laser diode mount[2], both from Thorlabs, showed in Figure 3.5d. Laser diodes can be quickly and easily changed in the mount. It is as simple as inserting the laser diode into the socket according to the imprinted pin assignment. The diode socket is located very close to the front of the cold plate making the connection of short lead devices easier.

3.2.2   Light coupling with fibers

In the beginning of this chapter we presented the schematics of the experimental setup. The main difference while changing the chips, is the method of light in/out coupling that leads the use of different apparatus. In all utilized setups light was coupled into the photonic chip by optical fibers. During my PhD I used to work with two types of fiber "setups". First one was based on a system of two single tapered fibers. On the second optical setup, I used a fiber array that has a spacing between fibers equal to the distance of the waveguides on the chips. Note, that the polarization of the light at the input of a chip is controlled by using a 2-paddles polarization controller placed between the VCSEL and the input fiber (See Figure 3.1).

---

[1]https://www.thorlabs.com/thorproduct.cfm?partnumber=ITC502
[2]https://www.thorlabs.com/thorproduct.cfm?partnumber=TCLDM9

3.2.2.1   Light in/out coupling by tapered fibers

During the first year of *SYMPHONY* project, for preliminary tests a single MRR on the chip is used. For this purpose, the optical fiber setup consisting of two tapered lensed optical fibers, *OZ-Optics TSMJ* series are used, that are positioned with sub-micrometric precision with a six axis remotely controlled mounts on two XYZ-translation stages, *Newport Ultralign 562* series actuators, *Newport NanoPZ PZA12* is used. The use of tapered lensed fibers is highly recommended, as it reduces the insertion losses to the photonic chip, by improving the matching of the mode field diameter. The use of the remotely controlled actuators permits more precise fiber alignment thanks to the range of motion and stability that ensures 30 nm of motion sensitivity with no loss of position when power is removed. The photonic chip is placed on a flat holder.
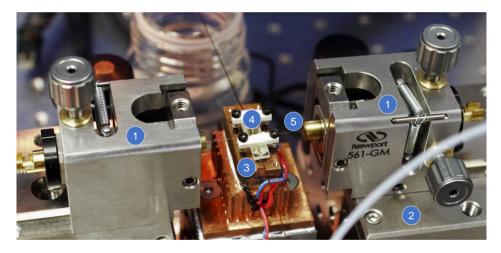

FIGURE 3.6: Photograph of the experimental setup. In the photo the numbering corresponds to: (1) the translation stages for the precise alignment of the optical fibers, (2) the remotely controlled Newport NanoPZ PZA12 stage, (3) sample holder, (4) the home made microfluidic flow-cell fixed on the chip, (5) the optical tapered lensed optical fiber.

The position of this holder can be translated longitudinally and vertically with micrometric screws, *Newport Ultralign 561D*. To visualize the sample and the positioning of the fibers, an optical microscope is placed above

the holder. The microfluidic flow-cell is fixed on the chip surface with small screws that are screwed on the holder. Figure 3.6 shows described setup.

3.2.2.2   Light in/out coupling by fiber array

The schematic layout of the fiber array for coupling light from the VCSEL to the chip and back to the photodetectors (PD) is shown in Figure 3.7. This fiber array consists of thirteen fibers each 1 meter long (see Figure 3.8a). Single mode (SM), multimode (MM) and single mode polarization maintaining (PM) fibers are used for this array. The operating wavelength range of the *780-HP* SM fibers is 780-970 nm, with a core diameter of 4.4 μm, while *PM780-HP* PM fibers have 770-1100 nm operating wavelength range and correspondingly 4.5 μm core diameter. The *GIF50C* MM fiber has an operating wavelength range between 800-1600 nm and a core diameter of 50 ± 2.5 μm. The fiber array facet is polished under an angle of $0°$. The distance between fibers is 250 μm which corresponds to the distances between neighbor waveguides on the chip.
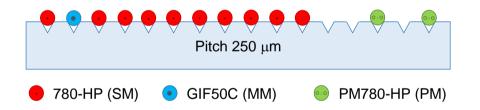

FIGURE 3.7: Fiber array used to couple light from the VCSEL and back to the photodetectors. In red are the single mode output fibers, in blue a multimode fiber and in green the single mode polarization maintaining input fibers used for simplification of the alignment process.

Orientation of the slow and fast axis of the polarization maintained (PM) fiber can be found in the same figure and in combination with the output of the used laser results in TE mode coupling into the chip.

For MRR multi-channel experiments within *SYMPHONY* project, we used a tapered lensed optical fiber for input and described fiber array for output light coupling, since input and output waveguides are located on the different edges of the chip, while for aMZI chips only a fiber array is

enough for light in/out coupling since all the input and output waveguides are on the same edge.

(a)   (b)

FIGURE 3.8: (a) The picture of fiber array that consists of thirteen 1 meter long fibers. (b) Zoomed view on the optical fiber array positioners and the chip under the PDMS microfluidic flow-cell fasten on the chip holder.

The fiber array was positioned relatively to the chip thanks to the aluminum holder placed on XYZ-translastion stages, *Newport Ultralign 562* series. In the Figure 3.8b it is shown a light coupling stage based on a fiber array.

3.2.3   Alignment stage

Even though light coupling from the fiber array to a chip was done with high stability, however chip replacement and realignment was a relatively long process. For this reason, Lionix International built a miniaturized fiber array to chip alignment stage (see Figure 3.9) devoted to handling our chips.

The input waveguide and the four output waveguides in the chip (see Figure 3.4) are interfaced to a fiber array. The stage reliably and quickly aligns and fastens the photonic chip to the fiber array and, at the same time, provides the microfluidic circuits.
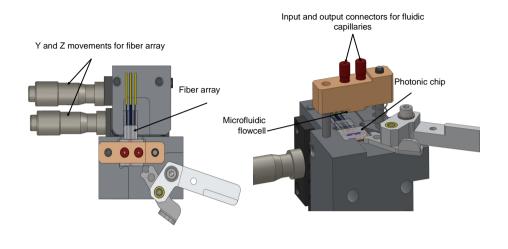
FIGURE 3.9: 3D renderings of the miniaturized alignment stage: The chip is placed into the insert of the holder and clamped into the corner by the handle. The chip is pressed downwards and leveled horizontal with the fiber array when the cover part with fluidic connectors and integrated flow-cell is pushed down. An integrated Viton O-ring assures a leak thigh connection between the photonic chip and the cover part and, at the same time, creates the microfluidic flow-cell over the sensor surface.

A clamp mechanism presses the photonic chip into a predefined corner of a frame. This assures a first rough alignment of the chip with the fiber array with micrometric resolution. The frame where the fiber array and the sensor chip are placed is milled in a single movement, ensuring a minimal alignment inaccuracy on the non adaptable pitch, roll and yaw axis. Horizontal leveling of chip to fiber array is accomplished when the cover part with integrated connectors for fluidic capillaries is pushed down onto the chip. In the same movement, a 200 μm height flow-cell is created by an integrated Viton O-ring underneath the cover part which seals off an elliptical area between the two connectors and the sensor area. Fine tuning of the alignment is then realized by maximizing the output signals with y and z movements.

3.3 Microfluidic flow-cell

One of the fundamental components of any biosensing system is a microfluidic flow-cell. This has to be designed in a way that

- it includes all sensing area of the biosensor in order to homogeneously wet the sensor's surface,

- it has a volume that permits a continuous laminar flow of flowing solutions,

- it is preferable to have a flow-cell made by a transparent material that makes possible to follow the flow evolution near to the sensor surface.

A part from these important properties of flow-cells, one has to consider ways for avoiding air bubbles while flowing liquids. When there are air bubbles, they simply can cover a sensing surface and not allow the target solutions to interact with sensor. Air bubbles can form from microfluidic material itself if it will chemically react with flowing solutions. Another reason of bubble formation can be a very tighten alignment of microfluidic on the sensor surface.
Considering these requirements, several microfluidic flow-cells have been proposed. Here I will present the two that I worked with.

3.3.1 Flowcell integrated to the alignment stage

On the alignment stage discussed above, a flow-cell is created by an integrated Viton O-ring (see Figure 3.10b) underneath the cover part which seals off an elliptical area between the two connectors and the sensor area. Flow cell is made from PMMA that is well known for these type of applications for its low molecule adsorption. Note, that all tubings and connectors in a loop are from PMMA as well. Microfluidic flow-cell can be pressed down against the chip using a screw as it is shown in Figure 3.10a. At that moment the O-ring seals off the sensor area and the enclosed area inside acts as a microfluidic flow-cell. On the Figure 3.10b in red the connectors for the fluid tubes (for tubing with 1/32" OD). The surface of that area is $\approx 22 \times 10^6$ μm^2.
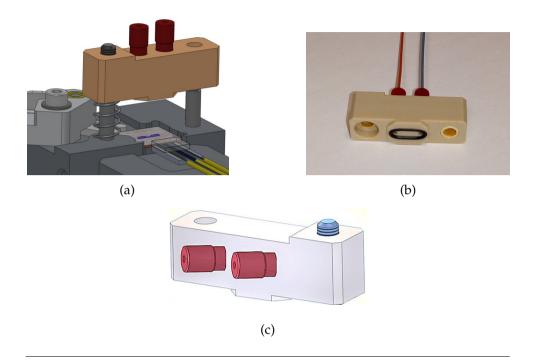
(a)

(b)

(c)

FIGURE 3.10: (a) The schematic of the flow-cell positioning against the chip. (b) The picture of the microfluidic cell. It contains two fluidic ports and an O-ring that forms a flow-cell. In red the connectors for the fluid tubes with 1/32″ OD. (c) Further modifications of the microfluidic flow-cell.

During squeezing the microfluidic its actual height changes which can cause liquid flow blocking and the air bubble formation. In order to optimize the flow-cell height, I tested three flow-cells with different heights (100μm, 150μm and 200μm) and followed the formation of air bubbles. Table 3.1 reports the results[3] of these tests.

---

[3]In a scale of 1 to 10, 10 means an easy removing of an air bubble with fast flow rate, while 1 means that it is needed to untight the screw that fixes the microfluidic and use a high flow. This leads to a misalignment of the sensor and to a probable leakage.

TABLE 3.1: Characteristics of microfluidic flow-cell depending on the cell height.

Height	Number of bubbles per hour	Easy to remove bubbles
μm		In scale of 1 to 10
100	>30	1
150	>10	5
200	>2	9

Finally, according to these results, for the final measurements of anti-biotin sensing the flow-cell with 200 μm height was chosen.

A possible modifications of the microfluidic is shown in Figure 3.10c. By placing the input and the output capillaries on the side of the microfluidic and by using a transparent PMMA one can achieve a desirable visibility of the chip and, respectively, of the sensor (MRR or aMZI) under the flow-cell which makes possible to get an immediate information about bubble arrival and flow behavior.

3.3.2 Flowcell from PDMS

The alternative to the microfluidic flow-cell discussed above, can be a flow-cell from PDMS that is made in UNITN. PDMS was chosen in order to obtain a leak-tight sealing between microfluidic and chip. This elastomer has been vastly adopted in the field of microfluidics, because it can be easily cast, even in molds with submicrometric features. When solid, its elastic properties make it a good sealant. The geometry of a flow-cell is limited by the chip dimensions. Our MRR based chips typically have 5 mm$\times$3 mm surface and the area where MRR sensors are located is typically 500 μm large, while for aMZI sensors the sensing window is 660 μm and thus demanding a flow-cell at least 700 μm. A flow-cell that fulfilled the requirements was fabricate by using a milled PCB as a mold for the PDMS casting. In Figure 3.11a it is shown the geometry of the flow-cell that was used in all experiments on MRR and in some on aMZI sensors. The inner 800 μm$\times$100μm$\times$5 mm volume corresponds to the flow-cell that covers all the sensing area on the chip (see Figure 3.11b).

(a)

(b)

(c)
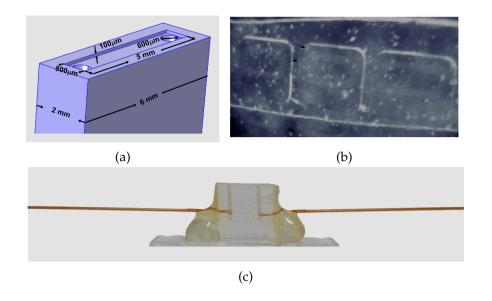
FIGURE 3.11: (a) Schematics of fabricated PDMS microfluidic. The inner part of 800 μm$\times$100μm$\times$5 mm volume corresponds to the flow-cell that covers all sensing area on the chip. (b) Microscope top-view picture showing the alignment of the flow-cell to the sensing arms of three aMZIs on the chip. (c) Side view of a PDMS flow-cell. The system consisting from the PDMS and 150 μm of ID capillaries are fixed on the plexiglass piece with epoxy glue.

The PDMS is prepared by mixing the elastomer, *Dow Corning Sylgard 184*, with the curing catalyst in 10:1 ratio. While the mix is still liquid, it is poured on the mold and placed in a vacuum chamber for 30 minutes. After degassing, still liquid PDMS is cured in room-temperature within maximum 48 hours. After carefully removing solid PDMS from the mold we cut and separate the pieces that correspond to microfluidics. Next by drilling we make halls of 600 μm diameter on the top and bottom of flowing area for satisfying liquid in and out condition. And finally we insert capillaries of 150 μm inner diameter (ID), into the holes for creating free liquid flow from the pump to the chip and out. In order to achieve a stable and easy alignable microfluidic system, a PDMS flow-cell and capillaries are fixed together in a middle of 1 cm long and 3 mm large plexiglass piece with bi-component epoxy glue (see Figure 3.11c). It completely becomes solid in almost four hours.

This way of fabrication of microfluidic flow-cells has few significant advantages, such the possibility to fabricate and glue up to fifteen flow-cells at the same time where each all is 2 mm wide and from 4 to 6 mm long.

3.4 Liquid flow module

In this section we will discuss two kinds of liquid flow modules to realize the necessary flow (i.e., continuous or oscillating flow) at the desired flow rates.

3.4.1 Syring-pump continuous flow

In biosensing measurements, there is always the need of switching between different solutions, i.e., buffers and target solution. Therefore, in our setup we used a pump that provides continuous flow and a 6-way loop injection valve for multi-solution injections. We choose a VICI M6 syringe-free pump and a VICI C1CF valve, which are shown in Figure 3.1 and are zoomed in Figure 3.12. The pump is able to feed an unlimited volume of carrier solution, usually the incubation buffer, to the sensor without interruptions.

The patented M Series liquid handling pump is a syringe-free pump capable of delivering a bidirectional flow over six orders of magnitude. The M Series is a positive displacement pump, which means that it is self-priming and tolerant of any gas which may find its way into the fluid lines which prevents bubbles formation. There is no separate fill cycle, and the capacity is unlimited.

This pump supplies a flow range of 5 nl/min to 5 ml/min (10 ml/min intermittent). USB and RS-485 communication protocols are incorporated into the micro- processor-driven controller. The included software package controls flow rates, flow direction, and metered volumes.
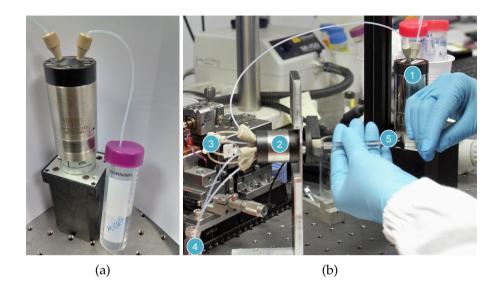
(a)   (b)

FIGURE 3.12: (a) Picture of the VICI M6 continuous flow pump, connecting a buffer reservoir to the injection valve. (b) Picture of the VICI C1CF injection valve at the moment of injection of target solution. The numbering corresponds to: (1) VICI M6 continuous flow pump, (2) 6-way loop injection valve, (3) sample loop, (4) waste collecting reservoir, (5) Hamilton syringe, 700 series, fixed blunt needle.

Continuously flowing as well as injected solutions final flow directions to the sensor are controlled by an injection valve. By switching a valve, small volumes of injected sample solutions can be delivered to the sensor in the flow of small liquid plugs, implanted in the continuous stream of carrier baseline solution. The working principle of such valve is demonstrated in Figure 3.13. When the handle is set to "load", the inner rotator connects the sample injection port to the sample loop (i.e., a piece of PMMA tube of known volume) by 1-6-3-2 way, and the pump port (i.e., a carrier or baseline liquid entrance port) to the sensor port by 4-5 way, hence making possible to fill the sample loop with the target solution, without interrupting the flow towards the sensor. When the handle of the valve is set to "inject" position, the inner rotator switch the connections, directing the sample injection port directly to the waste by 1-2 way, while the flow of carrier liquid pushes the sample in the capillaries towards the sensor by passing 4-3-6-5 loop.
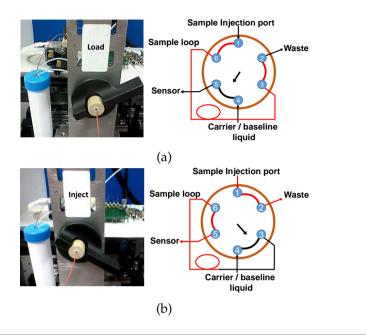
(a)

(b)

FIGURE 3.13: Schematic representation of the working principle of an injection valve. (a) When the valve is in "load" position, the sample loop can be filled with the analyte solution through the injection port, while the flow of carrier solution remains uninterrupted. (b) When the valve is in "inject" configuration, the carrier solution without mixing pushes the fixed-volume plug of analyte solution towards the sensor.

One of the many advantages of this valve is the "bubble-free" insertion of the sample solution into the loop between a pump and a sensor. The volume of the analyte solution is defined by the volume of sample loop, that can be minimized. The smallest volume that we used was 20 μL, but it can be still reduced.

For the final integration of *SYMPHONY* system, this loop played a highly important role, i.e., a connection between sensor and concentrator modules.

3.4.2 Oscillating flow pump

The second liquid handling unit which was built in Lionix enables execution of automated sample injection and washing. The main part of the liquid handling system consists of two (micro) peristaltic pumps, three valves, and the associated vials and tubing (P625/275 pumps and pump tube set P625/ TS020P *(Instech Laboratories, Inc., USA)*). In Figure 3.14a the experimental system used for anti-biotin experiments is shown. The liquid handling module is the lower instrument on the picture.

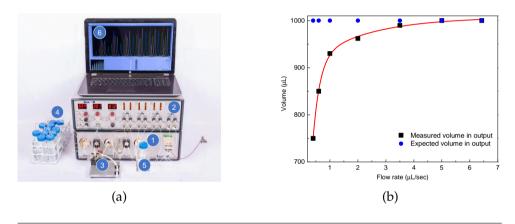|	
(a)	(b)

FIGURE 3.14: (a) A picture of an experimental apparatus for anti-biotin studies. Numbers correspond to: (1) Liquid handling module, (2) signal readout system system (OSROM), (3) alignment stage, (4) some sample reservoirs, (5) waste container, (6) computer connected to the pump and OSROM for system control and data registration. (b) The calibration of the volume of liquid in the output of the pump. Blue dots refer to expected liquid volume, while the black ones are the real measured ones. Red curves shows data fitting from where we extracted the accuracy of the flow rate.

Pumps and valves are operated via LabVIEW software. The pump can deliver 0.4-7 μL/s flow rate. The flow rate is conditioned by the given voltage that drives the pump. The relationship is given by:

$$F = 1.40078 \times V \,, \tag{3.1}$$

where F is a flow rate, V is a voltage and 1.40078 μL/(sV) is a constant

for the pump system. We used this relationship for the pump calibration. Through the software we set the flow rate, that was converted to the voltage and drove the pump. We aimed to flow 1 mL of solution (MilliQ in this case). The continuous flow duration was 1 mL/F. The flow duration was inserted to the program and when it finished the pump stopped working. We collected the liquid in the output of the pump in a reservoir and measure the real volume. Figure 3.14b shows that for small flow rates we measured different volumes (black dots) from what expected (blue dots). From data fit we got the relationship between the flow rate and the flowing volume.

This system allows an automatic switch between up to 8 solutions, such as buffer, water, cleaning solution, regeneration solution and sample, without changing reservoirs or moving tubings.

In parallel there is an alternative supply route for sending an analyte to the sensor via a so-called load/inject valve. This load/inject valve is supplied with a sample loop consisting of tubing of a certain capillary volume. The filling of the sample loop is conducted by an independent pump and can therefore be executed apart from the main supply toward the chip. The advantage of the use of an extra pump and valve is that loading of the sample loop can be done simultaneously. Measurement of the baseline then is done during infusion of buffer over the chip surface while the sample loop is being filled with sample. After filling the sample loop, its content can be injected over the chip by switching from load mode to inject mode. Cleaning and flushing of the sample loop and associated tubing serve to prevent contamination and carry-over between consecutive loading and measurement runs.

One way for incubation with sample, apart from unidirectional flow, is by using the oscillating flow. The oscillating flow in some sense shakes the analytes within the microfluidic volume, thus insuring a homogeneous coverage of the ligands, immobilized on the sensor surface, by the analytes. In the case of oscillating flow, the center of a sample plug is brought toward the middle of the sensor by a timed pumping. Flow is stopped then after which the sample plug is repeatedly moved back and forth over the sensor by pumping alternately in one and the other direction, at a volumetric flow rate down to 0.4 μL/s. The clear advantage of the oscillating flow approach is that, even with prolonged incubation, only a limited sample volume is needed.

3.5   Signal read-out systems

Finally, one of the most critical parts of any biosensing system is the signal read-out block. The correctness of the biosensing measurement depends on how sensitive is the readout system and how much is the contribution of noises for the signal reading. Here we will discuss two approaches for signal real-time detection and monitoring.

3.5.1   OSROM

One of many techniques for signal processing is the Fourier Transform algorithm. This is at the bases of the so-called OSROM read-out system, built in LioniX (see Figure 3.14a), hence many details are not presented here.

OSROM contains a pigtailed VCSEL (type ULM850, TO46, 2.0 mW; obtained from *Philips Technology GmbH, U-L-M Photonics, Ulm, Germany*) and 8 PIN photodiode detectors (PD) for simultaneus detection of the signal from different sensors, plus associated electronics and a built-in DAQ unit. Other parts of the OSROM are a current source for driving the VCSEL diode as well as a thermal controller of the embedded VCSEL. OSROM is suitable for the fiber array placed on the alignment stage described in the section 3.2.3. The experimental data reported in section 4.1.4 have been acquired by the OSROM system.

3.5.2   *SYMPHONY* signal acquisition

In this thesis I will mainly concentrate in data analyzes extracted from signal acquisition method realized in UNITN. In all discussed setups the output light is sent to a commercial Si transimpedance amplified photodetector from Thorlabs (*PDA36A*) interfaced to a PicoScope 4824 (an 8 channel USB oscilloscope) from *Pico Technology*. The PicoScope 4824 mix of 8 channels, high resolution and deep memory makes it suitable for a wide range of applications that cannot be met by traditional benchtop oscilloscopes. 12 bit resolution both for the oscilloscope and spectrum analyzer helps track down noise, analyze harmonics and measure distortion. Even though Picoscope 4824 has his own software for signal analyzes, therefore we connected it to a computer through the LabVIEW interface developed by us particularly for

the *SYMPHONY* system, i.e., VCSEL signal detection and biosensing measurements. Basically, we read the synchronization signal of the sawtooth function generator (modulation frequency of 20 Hz), which drives the current of the VCSEL and provides the wavelength scanning. Then we infer the direct modulation voltage from the moment passed from the trigger. Voltage-wavelength transmission is done by inserting in the LabVIEW code the results of the third order polynomial fit, shown in Figure 3.5b.

First, we acquire the output signal from VCSEL and save it as a normalization reference. By this way, we do not occupy a channel from the Picoscope for a reference signal. Then, the transmission spectra of simultaneously measured MRR or aMZI sensors is recovered by normalizing with the saved VCSEL reference signal. For every acquired spectrum, a Matlab script, embedded in the LabView code of the acquisition program, analyzes the data and extract the signal used for the sensing. The algorithms are different, depending on the kind of photonic sensor.

In the case of MRR, we choose a wavelength scanning range which includes one resonance. Within this range, the resonance wavelength is roughly estimated by finding the minimum value in the transmission. Then, by applying a Lorentzian fit, we extract the Q-factor and resonance peak position. Next, we perform a real-time monitoring of the resonance peak position. Thus the biosensing measurements becomes a measurement of the resonance wavelength variation in time. By using the Matlab script, it is possible to follow this variation in real time.

In the case of the aMZI, the algorithm is slightly different. Here a sinusoidal fitting on the data is performed. Knowing the frequency of the sinusoidal to be fitted, which is indeed the FSR, one can extract the amplitude and the phase from the Matlab script. In this case we monitor the time dependence of the phase value, which is later transformed to the wavelength.

This algorithm allows to measure the wavelength shift for both MRR and aMZI sensors down to 10 fm. The velocity of the measurement is determined by the PicoScope, which supports up to 80 MS/s sample rate.

3.6 SYMPHONY integrated system

The last section of this chapter is dedicated to description of the complete system development within the collaboration of the *SYMPHONY* European

project, i.e., the integration of the full system that is able to perform a complete analyses of milk samples against AFM1 presence. The system consists of three main subsystems. Due to the complexity of milk which is a matrix combining different molecules with different properties and sizes, it is a big challenge to build a module that can treat milk. AFM1 is a small molecule (327 Da) and in order to have a selective optical biosensor for AFM1 detection at low concentrations such as 50ng/ml, we first treat milk samples passing them through a fat removal module where we purify milk from proteins (mainly casein), vitamins, sugars and other disturbing components. Then, the purified samples are sent to a concentrator module, that is capable to concentrate the purified milk samples up to 20 times. The resulting liquid (eluate) then is injected on the sensor to sense the presence of toxin. The schematics of the system is shown in Figure 3.15.
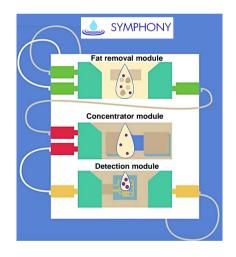

FIGURE 3.15: The principal modules of the *SYMPHONY* device: contaminated milk sample passes through the fat removal unit where fat, protein molecules are removed, then it undergoes a concentration process, after which it is sent to the photonic sensor.

The fat removal or defatting module was designed and built by FBK MST (MicroSystems Technology) group. It was implemented with commercial tangential flow filter (TFF) modules and it was composed of:

- a peristaltic pump (flow rate 30ml/min, overpressure 1 bar; recommended for best flexibility: flow rate up to 60 ml/min, 2 bar overpressure);

- a custom-made TFF assembly, using a custom milled membrane holder and a 20 μm pore nylon net by *Millipore*;

- a Pellicon TFF cassette pore 0.65 μm, accepting about 30ml/min from previous stage;

- a manometer for pressure check;

- recirculation of the retentate and collection of the processed sample in a vial.

For the further purification of milk samples the defatting module was accomplished with a chemical treatment that made possible to separate the most part of proteins. Milk sample preparation steps are described in AppendixB. Prepared sample then passed through the concentrator module, where the fundamental role was played by bullet designed by the partners ACREO and EPIGEM. The "bullet" consisted of a multiple stack of Nickel metal meshes (390 meshes in total) comprising an array of high surface area metal wires and an array of holes.

The working principle of bullet is following: it collects the relatively small number of AFM1 molecules in a relatively large sample volume and then subsequently eluates the collected molecules into a small known volume of clean material (i.e. concentration). In order to capture the AFM1 molecules, meshes were functionalized with anti AFM1 antibodies. The high surface area metal wires were stacked and achieved the specified high surface area within a 100μL volume. The concentrator was meant to concentrate AFM1 in buffer solution from 20 to 50 times. The bullet was designed to contain about 180 μL of fluid. Typical elution volume was smaller, $\approx$ 130 $\pm$ 20 μL. Out of this volume $\approx$ 40 μL of eluate is injected into a detector module.
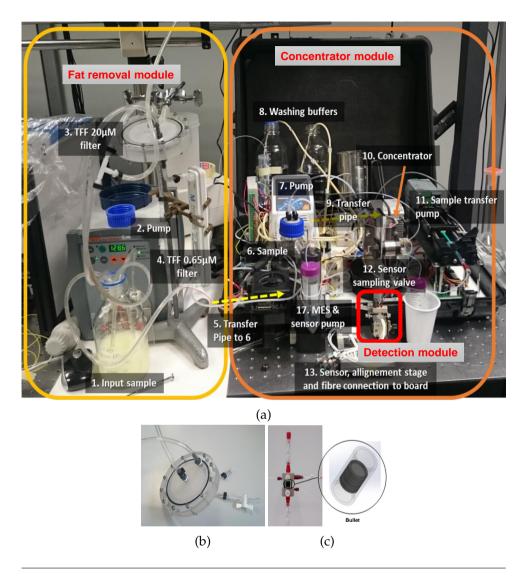
(a)

(b)   (c)

FIGURE 3.16: (a) The modules of *SYMPHONY* device connected with tubings. (b) TFF 20 μm filter assembly. (c) Concentrator unit and the schematics of the bullet.

Figure 3.16a represents the real system that was demonstrated in the final review meeting of the project. Despite the fact that the overall picture

of the system is not the one that was planned from the beginning, but the transfer of milk sample from one module to another is realized by just a single tube, thus securing the concern of an integrated system for milk analyses against AFM1. The integration between the first two units was easily realized by connecting deffater output and concentrator input tubes to the same reservoir where a protein and fat free milk sample was collected. Yet the most challenging part was the connection between the concentrator and the detection modules. In the output of the concentrator module, we got eluate relieved under high pressure and thus full of air bubbles. The presence of an air bubble on the sensor surface is determined a "fake" resonance/phase shift as a result of liquid-air refractive index changes. Taking account this issue we decided to have a reservoir after the concentrator, where we could collect the eluate and clearly see when air bubbles separated from liquid part. Hopefully we were able to have the required volume of eluate free of bubbles after few seconds already. Finally, the injection of eluate to the photonic sensor took place by using a syringe pump described in section 3.4.1 and a Milliliter Syringe Pump Module from *Harvard Apparatus* in withdraw mode in order to fill the sample loop of the valve as it is shown in Figure 3.17a.

The movements of the second pump are controlled through the same software as the concentrator and detector (see Figure 3.19).

When the valve is in "Load eluate" position, the sample loop can be filled with the eluate through the load port by dispensing the *Harvard Apparatus* syringe pump, while the continuous flow of carrier solution remains uninterrupted thanks to the first *VICI* pump. Here we deal with 2-3-6-1 and parallel 4-5 flow directions (see Figure 3.17a). We carefully filled in the volume of 30 μL of loop avoiding an injection air bubbles as well, and immediately switched the valve in position "Inject eluate", where the carrier buffer pushed the eluate to the sensor by 4-3-6-5 routine (see Figure 3.17b).
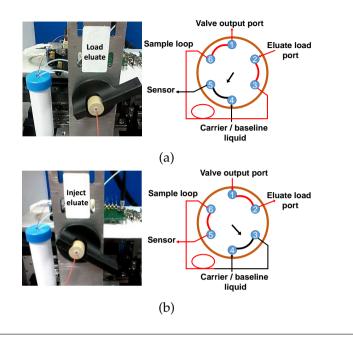
(a)

(b)

FIGURE 3.17: Schematic representation of the working principle of an injection valve in integrated system.

In Figure 3.18 we show the final integrated system of concentrator - detector modules. Detector, i.e., aMZI chip was placed on the alignment stage. The signal read-out is carried out by the same LabVIEW program that is already discussed in the section 3.5.2.

The sensor board was designed in collaboration with FBK. We developed a final software interface for the whole *SYMPHONY* system, that included concentrator, *Harvard Apparatus* syringe-pump and sensor board controls. Figure 3.19 shows the *SYMPHONY* interface. The white curve shows the sensorgram that was measured in this system.
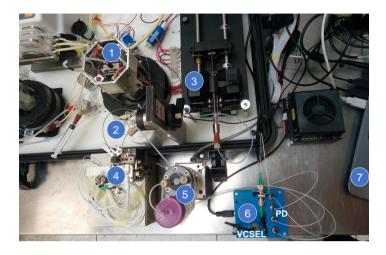
FIGURE 3.18: Concentrator-detector integration. Numberings correspond to: (1) bullet, (2) eluate reservoir, (3) *Harvard Apparatus* syringe pump, (4) alignment stage with aMZI chip on it, (5) *VICI* pump, (6) sensor board, (7) computer that is connected with the board through USB and which runs a software.
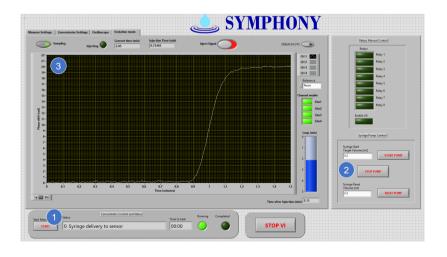

FIGURE 3.19: The interface of *SYMPHONY* integrated system. Numberings correspond to: (1) concentrator control, (2) *Harvard Apparatus* syringe pump control, (3) sensor board read-out interface.

Chapter 4

Results and discussions

In this chapter the results of the biosensing experiments performed with the sensors that have been developed during my PhD are presented and discussed.

In § 4.1, results on the SiON microring resonator based photonic sensors will be presented in terms of bulk sensitivity, limit of detection, AFM1 detection in buffer solution. Based on the validation of the functionalization method, a sensor is developed with an asymmetric Mach-Zehnder interferometer. Section 4.2 reports the characterization of the aMZI photonic chip. Finally, AFM1 detection first in buffer, then in the milk samples is demonstrated. The lowest detectable concentration of AFM1 with *SYMPHONY* system is defined.

The last § 4.3 is focused on the development of affinity biosensors as an application of TripleX based photonic chips, in particular multi-MRR configuration for biotinylated BSA-anti-biotin molecular interaction study. Eight cycles of sensor regeneration processes are successfully realized.

4.1   Microring Resonators for AFM1 detection

I started my PhD research after the first year of *SYMPHONY* project, when the final design of the photonic biosensor was completed. A multi-MRR chip shown in Figure 4.1 was fabricated. These devices were from the BS2 and BS3 wafers.

For the measurements of these chips, the waveguide-probing setup presented in Figure 3.1 is used with the only difference that a fiber array is coupled to the chip outputs. The fiber array allows measuring simultaneously the transmission of four different microrings.
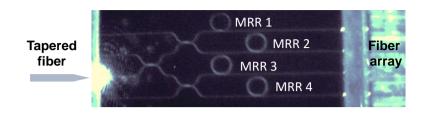
FIGURE 4.1: An image of MRR based chip. On the left, the bright spot is the laser scattering at the input waveguide. On the right, the fiber array is visible. On the chip, the location of the four microring resonators is indicated.

4.1.1 Optical characteristics of MRR chips

The chips from the BS2 and BS3 wafers are characterized. Table 4.1 reports the optical characteristics of covered MRR (SiO$_2$ cladding is present) for BS2 and BS3 wafers. To guarantee single mode operation and to limit propagation losses, was decided to keep the width of the bus waveguide at 900 nm and of the ring one at 1000 nm, respectively. In the work [126] are shown the results of the simulations and optical characteristics of the following geometries.

Propagation losses as low as 0.8 dB/cm for 350 nm $\times$950 nm waveguides were measured in TE polarization. For the same waveguide geometry bending losses in the curve with radius of 100 μm were found to be 0.1 dB/90°. Directional couplers based on such waveguides demonstrated 49/51 splitting ratio for 65 μm-long coupling zone.

The results of the experimental observations yield the fact that the photonic chips from both BS2 and BS3 wafers show the similar performances regarding to the losses. However, the Q-factor for the MRRs from the BS3 wafer is slightly higher in comparison with the one of BS2 wafer, as a reason of the wider waveguide and, consequently, the better confinement of the guiding mode in the bus waveguide (w_{BS3}=350 nm>305 nm=w_{BS2}).

Next, we characterized MRRs with opened sensing windows for both wafers. As it is already described in § 3.1.1, 20 μm wide sensing windows are opened on three of the four MRRs. The removing of the SiO$_2$ layer yields a change in the refractive index of the cladding, resulting in a lower mode confinement and, consequently, in a Q-factor change. After the opening of

TABLE 4.1: Characteristics of SiO$_2$-covered MRRs for samples from BS2 and BS3 wafers (mean value).

Wafer	SiON thickness (nm)	Waveguide width (nm)	Polarization	Propagation losses (dB/cm)[1]	Bending losses (dB/90°)[2]	Q-factor (× 10³)[3]
BS2	305	900	TE	1.0	0.2	
		900	TM	1.1	0.2	
		1000	TE	0.8	0.1	43
		1000	TM	0.9	0.1	
BS3	350	900	TE	0.9	0.1	
		900	TM	1.0	0.1	
		1000	TE	0.8	0.1	46
		1000	TM	0.8	0.1	

[1] The measurement errors are below 0.3 dB/cm
[2] The measurement errors are below 0.1 dB/90°
[3] The measurement errors are below 1×10^3

the sensing windows, we noticed that for TM polarization of BS2 chips the resonance peak vanished. This can be explained with the etching uncertainties, that can either have introduced more surface roughness, increasing the surface losses, or have altered the geometry of the waveguides, increasing the radiative losses such that only TE polarization is guided. We performed the sensing measurements only for TE polarization in case of BS2 chips, and both TE and TM polarizations in case of BS3 chips.

In Figure 4.2a we report an example of a transmission spectra, taken for BS2 sample when the resonator is covered with water. The measured Q-factor in this figure is the maximum for BS2 wafer. Note, the transmission is normalized by VCSEL reference signal. In order to obtain the loaded Q-factor, we performed Lorentzian fit of the resonance peak. The maximum Q-factor of $4\times10^4\pm40$ was extracted, correspondingly to an extinction ratio of *ER*=5dB, calculated according to Eq. 2.18. More than ten chips from this wafer have been measured and for the mean value of 3.1×10^4 with standard deviation of 9×10^3 was calculated for the loaded Q-factor (see Figure 4.2c). Such variation of the Q-factor can be explained with fabrication uncertainties as well as by the inhomogeneous absorption losses of the water while changing from chip to chip. However the peak resolution is sufficient for further sensing measurements.

A significant difference was observed for the chips from BS3 wafer reported in Figure 4.2b. For BS3 chips the resonance peak for both TE and TM polarizations is observed. The maximum Q-factor of $1.3\times10^5\pm500$, correspondingly to extinction ratio of *ER*=7 dB for TE polarization and the Q-factor of $5\times10^4\pm90$, with *ER*=4 dB in case of TM polarization are measured for the same MRR. Repeated measurements for a number of chips for the loaded Q-factor show a mean value of 5.5×10^4 with standard deviation of 10^4 in case of TM and mean value of 11.5×10^4 with standard deviation of 1.5×10^4 in case of TE polarization, respectively (see Figure 4.2c). For the TE polarization the loaded (measured) quality factors are about twice of the ones observed for TM polarization, and this trend was obtained for all chips. It is caused by the fact that TE mode is more confined in the waveguide than the TM mode.
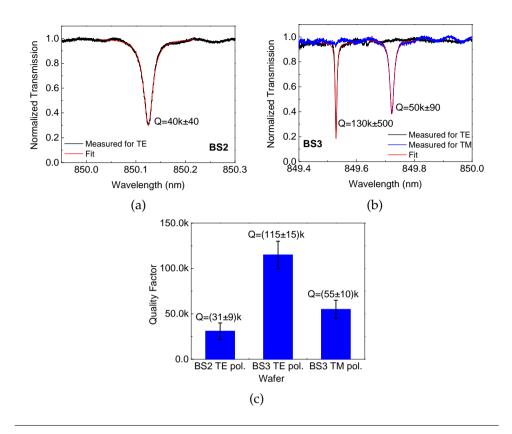
FIGURE 4.2: Normalized transmission spectra for (a) TE polarization of the microring resonator from BS2 wafer, and (b) TE and TM polarizations of the microring resonator from BS3 wafer. Q-factors are extracted from the Lorentzian fit. (c) The mean values of the Q-factors, calculated for more than 10 chips from each wafer.

4.1.2   Sensitivity and Limit of Detection

After optical characterization, bulk sensitivity (S_b) measurements are performed and, consequently, the LOD of the system is determined.

In order to calculate S_b, we monitored in real-time the spectral shifts of the whispering gallery mode (WGM) resonances of the microrings, while

the sensors were exposed to glucose-water solutions of various concentrations. The refractive index of such solutions can be easily measured or estimated. Empirically it has been demonstrated a linear dependence of the refractive index from the glucose-water solution concentration up to 20% (1% = 1 gm/100 ml) solution [127]. According to this relationship, the refractive index variation can be calculated as:

$$\Delta n = 0.0015 \times C, \tag{4.1}$$

where C is glucose concentration in gm/100 ml units.

Volumetric sensing measurement is started with flowing a buffer solution, in this case MES buffer, simultaneously on three microring resonators on a single chip from BS2 wafer. The choice of buffer is due to the use of the same buffer for the measurements, so that we keep the same environmental conditions. Continuous flow at 20 μL/min flow rate is used with the VICI pump described in § 3.4.1. For this measurement a sample loop with $\approx$75 μL is used, thus yielding $\approx$3.7 minutes flow of injected solution over the sensor. Figure 4.3a represents the temporal evolutions of the resonance wavelength (sensorgram) upon subsequent injections of solutions at different concentrations. The first injection is pure water that plays the role of the baseline for glucose-water solutions. When water is injected a negative shift of the resonance wavelength is observed, since the refractive index of water is smaller than the one of MES. As it is expected, all three microrings demonstrate similar performances, showing the similar shift. After $\approx$3.7 minutes, when MES again arrives to the sensor the resonance wavelength recovers the initial value corresponding to 0 nm. Next injection is 0.1% glucose-water solution that yields a resonance shift smaller than previous, due to the relatively higher refractive index in comparison with pure water. Injections are repeated for 0.2, 0.3, 0.4 and 0.5% of glucose-water solutions. With the increase of glucose concentration one can clearly distinguish an increase of the difference between pure water and glucose-water solutions.
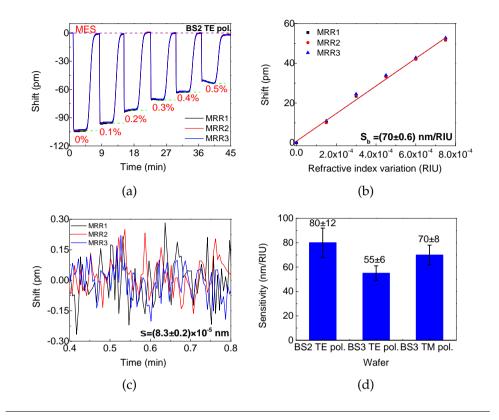
FIGURE 4.3: Bulk sensitivity measurements on BS2 sample. The variation in refractive index is obtained by injections of water-glucose solutions at different concentrations. (a) The temporal evolutions of the resonance wavelength upon subsequent injections of solutions at different concentrations, (b) corresponding resonance wavelength shifts linear fit for TE polarization, (c) shift taken in 24 seconds of MES flow. (d) The mean values of bulk sensitivity, calculated for more than 7 chips for TE polarization of BS2 and both TE and TM polarizations for BS3 chips.

Figure 4.3b represents resonance shift, taken as a difference of the maximum absolute values of the shift for each concentration and the shift due to pure water, as a function of the bulk refractive index variations calculated according to Eq. (4.1). The slope of the linear fit corresponds to S_b, which is ≈70 nm/RIU for the three MRR sensors. The difference of the sensitivity for these MRR is <1%.

In order to obtain the limit of detection (LOD) of the system, the standard deviation of the signal is taken in a region where only the buffer is flowing. We took a period between 0.4-0.8 minutes of the sensorgram (see Figure 4.3c). The standard deviations for all three MRRs are similar, thus we can take the average value of σ = (8.3$\pm$0.2)$\times 10^{-5}$ nm. LOD for this particular chip calculated by Eq. (2.4) is equal to (3.5$\pm$0.1)$\times 10^{-6}$ RIU.

The same protocol was used for all the three cases, i.e., BS2 chips in TE polarization and BS3 chips in both TE and TM polarizations. Figure 4.3d shows statistically obtained values of the bulk sensitivity for these cases. The best sensitivity for BS2 wafer in TE polarization (note, we do not observe a resonance in TM polarization) showing S_b = (80$\pm$12) nm/RIU average value, is calculated for more than 7 chips. Very close values are measured by the BS3 chips for TM polarization, i.e., S_b = (70$\pm$8) nm/RIU, and finally the lowest sensitivity is observed for the BS3 chips in TE polarization of S_b = (55$\pm$6) nm/RIU. Although, all the experimental conditions were kept constant, still there are several reasons for the variation of the sensitivity, such as temperature in laboratory, glucose concentration small variation for each preparation, chip differences coming from the fabrication and so on. However these differences in the sensitivity do not have a significant influence on the limit of detection. Measured LOD for all cases is in the range of (3$\div$6)$\times 10^{-6}$ RIU.

Comparing our devices in terms of both bulk sensitivity and LOD with the state of art, we can see that BS2 and BS3 chips have similar characteristics with the other structures shown in Table 1.2. In particular, the LOD for different types of devices, varies in the range of 10^{-6} - 10^{-7} RIU.

4.1.3 MRR surface functionalization

After a sensor chip is characterized in terms of the Q-factor, bulk sensitivity and LOD, its surface is treated chemically, i.e., it undergoes a functionalization process in order to selectively detect a target molecule, in particular AFM1 in this case.

Two different protocols were developed based on DNA-aptamer and Fab' in order to identify the best one in terms of high reproducibility, stability and selectivity of the surface functionalization. It was demonstrated, that even though there are several properties of the aptamers, such as the

stability to long-term storage or the more economic prices, the antibodies were more reproducible and sensitivity to AFM1 detection.

Development of the functionalization procedure was performed by Laura Pasquardini. In § 4.1.3.1 and § 4.1.3.2 the functionalization protocols based on DNA-aptamers and Fab′ are described, respectively.

4.1.3.1   Aptamer based functionalization strategy

The functionalization procedure performed on the sensors is based on wet silanization protocol. After a cleaning process (with a Piranha solution) to remove organic contaminations the samples were immersed in 0.01% v/v of GPTMS (3-glycidoxypro-pyl methyldiethoxy silane) in anhydrous toluene at 60 °C for 10 min. Then an amino-terminated DNA-aptamer (5′-NH_2-$(CH_2)_6$-GT TGG GCA CGT GTT GTC TCT CTG TGT CTC GTG CCC TTC GCT AGG CCC ACA-3′) at 100 μM in phosphate buffer (50 mM, ionic strength 300 mM, pH 8) was incubated on silanized surfaces for 2 h. The aptameric sequence with a k_D of 10 nM was identified by NeoVentures Biotechnology Inc. [128]. The amino-modified sequence is HPLC purified and was purchased from IDT Integrated DNA Technologies (Leuven, Belgium). Finally, an ethanolamine passivation at 1 mM for 30 min was applied.

4.1.3.2   Fab′ based functionalization strategy

F(ab′)$_2$ fragments are generated by protease digestion (Immobilized Papain Thermo Scientific) of 20 μL of 1 mg/mL anti-AFM1 polyclonal rabbit IgG according to manufacturer's instructions. Then, a 13.3 μM F(ab′)$_2$ solution is mixed with 10 mM DTT to reduce the disulphide bond in the hinge region, and the mixture is incubated for two hours at room temperature. The mixture is poured into a centrifugal filter unit (Microcon YM-10, MWCO 10000, Millipore Corp., Billerica, MA, USA) to remove the excess of DTT. Fab′ are immobilized on the surface adapting the protocol described in [129]. In order to introduce thiol groups able to react with the cysteine groups on Fab fragments, the silicon oxynitride surface is functionalized in wet conditions with mercaptosilane (MPTMS) [130]. The surfaces (both chip and flat samples) are cleaned with an argon plasma (6.8W, one minute) to remove organic contaminants and to hydroxylate the surface and are, then, immersed in a 1% v/v solution of MPTMS in toluene anhydrous at 60 °C for

10 min. Silane-coated substrates are rinsed several times with toluene and then dried in a stream of nitrogen. The immobilization of Fab' fragments onto the bare surface is carried out by deposition of 80 μL of a 0.33 μM Fab' in 10 mM phosphate buffer with 10 mM EDTA. After 2 min, the surface is PEGylated by addition, first, of 200 μM final concentration of mPEG-SH 5000 (for 30 min on orbital shaker at 80 rpm) and, then, of 200 μM of mPEG-SH 2000 (for 60 min on shaker at 80 rpm). The surface is finally cleaned using PBS-EDTA buffer. The same protocol is applied on standard flat gold surface. The concentration of Fab' is determined by measuring their absorbance with a Nanodrop instrument, (extinction coefficient (0.1%) =1.35 at 280 nm).

4.1.3.3   Comparison of the surface functionalization strategies

The Fab' density on silanized SiON is optimized incubating different concentration. After immobilization, the surfaces is incubated with an HRP-conjugated AFM1 (AFM1-HRP) stock solution diluted 80 times in 50 mM MES buffer pH 6.6 for one hour, washed twice in buffer and transferred to a black microplate, where the developer solution is added. HRP in presence of a suitable substrate develops a chemiluminescence signal that can be easily detected. After five min incubation, the signal is recorded with a ChemiDoc MP system (Biorad). Respect to a gold surface (a standard surface for thiol chemistry), a saturation of the surface is obtained at low Fab' concentration, as reported in Figure 4.4a. Fitting the data with a Langmuir equation, it is possible to determine the surface saturation. For SiON surface the value saturates at 2957 a.u. (correlation coefficient = 0.99), while for gold surface a 18588 a.u. value was estimated (correlation coefficient = 0.97). The signal recorded on silanized SiON surface is about 6 times lower than that recorded on gold, suggesting that the surface binding sites on mercaptosilanized SiON are fewer than those on gold surface, as expected. A 0.33 μM Fab' concentration is selected for the following experiments.
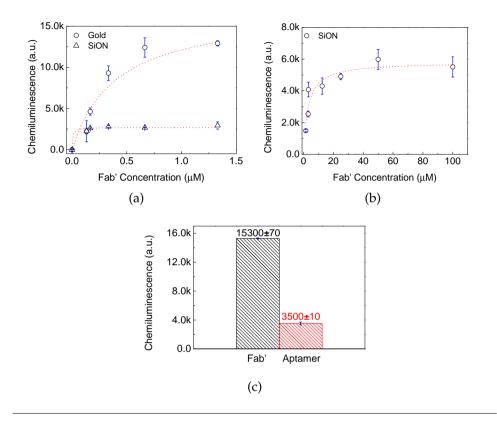
FIGURE 4.4: (a) Chemiluminescence detection of AFM1-HRP on SiON substrates after immobilization of different amount of Fab'. A gold substrate is used as reference. The values are reported as mean value on at least two different experimental sessions and the error bars represent the standard deviation. (b) Fluorescence signal on SiON surface functionalized with different amount of fluorescent aptameric sequences. The values are reported as mean value on three different samples and the error bars represent the standard deviation. (c) Chemiluminescence detection of AFM1-HRP on SiON flat surfaces functionalized with Fab' or aptamer strategy. The data are represented as mean value on three samples and error bars are reported as standard deviation.

The aptamer density is instead optimized using a fluorescent- labelled DNA aptameric sequence. The fluorescence signal is recorded after two

hours of incubation and washing. Figure 4.4b shows the fluorescence signal as a function of the aptamer concentration. Also in this case the Langmuir equation describes the aptamer immobilization. The saturation level resulted at 5970 a.u. (correlation coefficient = 0.98), suggesting that a concentration above 50μM is enough to reach the surface saturation. Then, the two functionalization procedures are compared with respect to their ability to recognize AFM1 by using AFM1-HRP. SiON flat substrates are functionalized with DNA-aptamers or Fab' and the surfaces are incubated with AFM1-HRP in the same conditions reported above. The signals recorded on the Fab'- or aptamer- functionalized surfaces are reported in Figure 4.4c. A higher signal is observed for the Fab'-functionalized surface. The AFM1 detection is about 5 times more efficient on the immune surface respect to the aptamer-functionalized surface.

4.1.4   AFM1 sensing measurements with MRR

Guided by the results of the bulk sensitivity, photonic chips from the BS2 wafer were used for the AFM1 sensing measurements. For those experiments, the microfluidic chamber was initially filled with a 50 mM MES buffer with pH 6.6. We then injected 75 μL of a solution containing the targeted mycotoxin at a known concentration in order to measure the evolution of the resonance wavelength of the resonators due to the capture of the toxins from the functionalized MRR. The solution is inserted into the microfluidic chamber using an injection loop, which avoids the formation of air bubbles in the microfluidic chamber during the buffer exchange and allows having a known fixed injected volume. For all the measurements the flow rate of 3 μL/min was used.

Figure 4.5a shows an example of a sensorgram measured with a solution of 100 nM AFM1 when the surface of the MRRs on the BS2 chip has been functionalized with the Fab'. The measurement starts with flowing the MES buffer. The resonance wavelengths of the three exposed sensors, i.e., MRR2-MRR4, as well as that of the reference sensor MRR1, stay constant while flowing the buffer. We consider these resonance wavelength as a baseline.
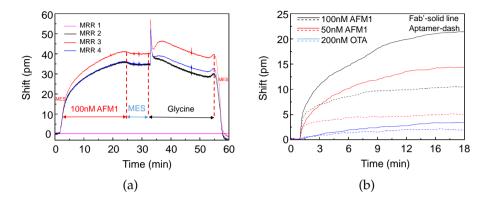
FIGURE 4.5: (a) Sensorgram of a complete measurement cycle for a sensor functionalized with Fab' and for a 100 nM AFM1 solution. (b) Sensing measurements of 50 nM and 100 nM pure AFM1 and 200 nM OTA diluted in MES performed on sensors functionalized with both aptamer (dash lines) and Fab' (solid lines) based strategies. The flowing buffer is MES.

Then, we inject the 100 nM AFM1 solution. The solution reaches the sensor after 2 min when we observe a large resonance shift for MRR2-MRR4 while no shift is measured for the reference MRR1. This shows that no temperature fluctuations are caused by the change in the flown solution. The MRR2-MRR4 resonances roughly follow an exponential law, due to the specific binding of AFM1 to the functionalized surfaces of the three MRR. The binding of the toxins occur from the 2.5 min to the 25 min. At this time, we stop the toxins flow and we switch to a MES buffer flow. This causes a decrease in the resonance shift due to the rinsing of the physically absorbed AFM1 from the surface. Therefore, we consider indicative of the sensor response the value of the resonance shift after 22.5 minutes that is varying between 33÷38 pm for MRR2-MRR4. Finally, we inject a 100 mM glycine-HCl pH 2.3 solution at t=30 min, in order to break the AFM1-antibody bonds and to remove all the linked toxins from the sensor surface while keeping the antibodies in place. This regeneration solution is commonly used in surface binding experiments. It perturbs the aptamers or Fab' tridimensional conformation, which leads to a release of the captured toxins. After glycine solution, at t=55 min we inject again MES and the signals reach close to the baseline indicating that the sensors are again clean. Note that the MRR1 resonance does not shift during the whole cycle. The same procedure was

realized in case of aptamer-based functionalized sensors.

The next important step for any biosensor is to control the selectivity against the target bioanalytes. For this purpose we performed sensing measurements of another mycotoxin with the similar molecular dimensions as well and compared the signals caused by AFM1 specific binding or Ocratoxin A (OTA) non-specific interaction with surface functionalization. Note, that the molecular weight of the AFM1 is 328.27 g/mol and the OTA is 403.81 g/mol.

Figure 4.5b shows various sensorgrams for different composition of the tested samples. Functionalization is specific to AFM1. In order to test the specificity of the functionalization we tried the sensor with a solution containing OTA. We performed sensing measurements with AFM1 at 50 nM, 100 nM and OTA at 200 nM concentrations. Both mycotoxins are diluted in MES buffer. The protocol of the measurements is the same. For both functionalization strategies, the specificity is observed. Indeed, the resonance shift is small for OTA while it is larger for AFM1.

We then tested the reproducibility of results. We repeated AFM1 sensing measurements for numerous chips for both functionalization strategies. Figure 4.6 shows the histograms of repeated measurements on different chips for the same functionalization protocols and the same AFM1 solution to test the reproducibility of the sensor response from chip-to-chip. Figure 4.6a shows the results for aptamer-functionalized MRRs when the concentration of injected AFM1 is 100 nM. As we can clearly observe, the resonance shift changes between 10 pm to 220 pm. The average value with a standard deviation is $\approx 35 \pm 60$ pm showing that the reproducibility of the measurements is poor. The source of these uncertainties can be looked for in the wafer processing, in the functionalization procedure or in the toxin binding dynamics. Since wafer processing reproducibility is very high and the surface functionalization gives reproducible results, we conclude that the low reproducibility is related to binding steps. Figure 4.6b reports the same analyses for sensors functionalized with Fab'. The distribution of the resonance shifts on different chips is much narrower than with aptamer functionalization (between 15 pm and 42 pm) yielding an average value and a standard deviation of $\approx 25 \pm 8$ pm. It is therefore concluded that the Fab' functionalization is more reproducible than the aptamer one.
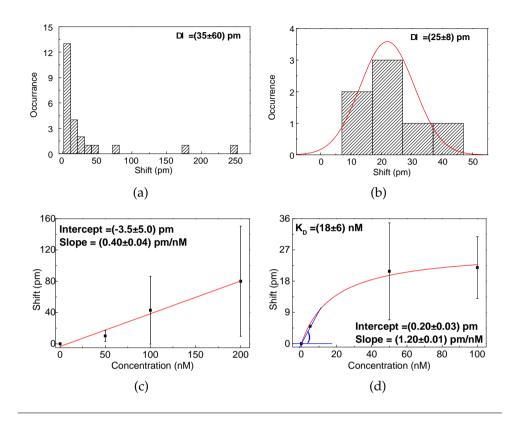
FIGURE 4.6: (a) The histogram of the resonance shift of the microring resonator for aptamer based functionalization. The average resonance shift is 35 pm with an error of 60 pm. (b) The histogram of the resonance shift of the microring resonator for Fab' based functionalization. The average resonance shift is 25 nm with an error of 8 pm. Both histograms are given for 100 nM AFM1. Bin size is 10 pm. (c) The resonance shift for different concentrations of AFM1 detected with aptamers-based functionalization. The line is a linear regression of the data. (d) The resonance shift for different concentrations of AFM1 detected by Fab'. The red line is a Langmuir fit of experimental data and the blue line shows the linear region of the dependence.

In addition, we note that the average shifts are close, within the error bars, for the two functionalization. This differs from what observed with the surface experiments. There are several possible explanations for this. For the flat surface experiments, an enzyme- conjugated Aflatoxin is used, while, for sensing measurements, a pure AFM1 is used. AFM1-HRP and

the antibody used for Fab' production are part of the same Elisa assay. It could be that a higher affinity of Fab' for AFM1-HRP occurred with respect to aptamers. Another consideration relates to the signal measurement methods. Chemiluminescence detection of AFM1-HRP on SiON substrates gives direct information about bound molecules, while the detected signal of the MRRs reflects the environmental changes near to the sensor surface sensed by the evanescent field of the guided optical mode. The evanescent field depends on the thickness of the bound layer on the surface. In fact, the volume of interaction between the analyte and the evanescent field of the MRR optical mode is constrained by the thickness of the layer of the captured analyte. In the case of nanometric-sized molecules, this means that most of the evanescent field of the optical mode is unperturbed and not used to produce a signal. The molecular weight of Fab' is around 500×10^2 g/mol (50 kDa), more than three times larger than the aptamers, while the molecular weight of AFM1 is 328.27 g/mol. The resulting bound layer is therefore far apart for the Fab'-based functionalization than for the aptamer-based functionalization which decreases the interaction between the evanescent tail and the small AFM1 molecules.

For a complete description of a biosensor, a smallest detectable concentration (LOD) of target, in this case AFM1, is needed to be defined. We performed repeated sensing measurements for various AFM1 concentrations. Figure 4.6c shows the measured resonance shift dependence from AFM1 concentration for aptamer-based functionalized sensors. In order to obtain the smallest detectable concentration of AFM1 that can be reliably detected, we use a linear regression to the data (line in Figure 4.6c). The slope of the linear regression yields the sensitivity of the sensor to AFM1, i.e., S_{AFM1}=(0.40±0.04) pm/nM. From resonance measurements we have a standard deviation of σ_λ=(0.08±0.002) pm on the measured wavelength. This corresponds to a theoretical LOD_{AFM1}=$3\sigma_\lambda/S_{AFM1}$=(0.6±0.1) nM.

On the other hand, if we consider the intercept of the linear regression as a best estimate of the error σ_{AFM1} in the concentration measurements, we obtain the experimental LOD_{AFM1}=$3\sigma_{AFM1}/S_{AFM1}\cong$(25±40) nM. For aptamer-based strategy we observed a big scattering of data for all measured concentrations and thus we did not obtain saturation even for high concentrations.

In contrast, with for Fab'-based strategy, we observe the signal saturation at high AFM1 concentrations (see Figure 4.6d). If we consider the dependence of the shift from the small AFM1 concentrations as linear (ble line

in Figure 4.6d), a rough estimation will give the experimental $\text{LOD}_{AFM1} \cong$ $3 \times (0.20 \pm 0.03)$ pm/(1.20 ± 0.01) pm/nM $= (0.5 \pm 0.1)$ nM.

Moreover, in this case, by fitting the data with a Langmuir function (Eq. 2.41), the dissociation constant and the affinity of Fab'-AFM1 interaction can be extracted. From the fit we obtained the values of $K_D = (18 \pm 6)$ nM and $K_A = (5 \pm 2) \times 10^7$ M^{-1}, respectively. Thus, the low-affinity interaction is taking place.

Figure 4.6d shows another important observation as well. Since the signal levels for the 50 nM and 100 nM AFM1 solutions are very close, we can conclude that 50 nM AFM1 is enough to cover all binding sites of the immobilized ligands on the sensor surface. Hence, we can calculate the Fab' surface density by doing the following estimations. 50 nM AFM1 corresponds to the $\approx 3 \times 10^{15}$ molecules/L. The volume over the MRR (SiON waveguide surface) is $\approx 5 \times 10^{-11}$ L (the height of the microfluidic is ≈ 100 μm). Thus, the number of AFM1 molecules over the MRR sensing area is 15^4. Let us consider that all the AFM1 molecules are bonded by the Fab' molecules, from where we get $\approx 2.5 \times 10^{-9}$ mol Fab' on the MRR surface. The sensing surface of the MRR waveguide is 560 μm^2, which yields the Fab' surface density of $\approx 5 \times 10^{-4}$ mol/cm^2, equivalent to 25 g/cm^2 (the Fab' molecular weight of 50 kg/mol).

Finally, let us note, that even if the LOD_{AFM1} for the Fab'-based functionalized MRR sensors is 50 times smaller then for the aptamer functionalized ones, however in both cases the LOD_{AFM1} is larger that what EU regulations allow, i.e., 152 pM for adults and 76 pM for infants. Thus we conclude that our MRR sensors are not suitable for AFM1 detection.

4.2   aMZI for AFM1 detection

The aMZI chip used in sensing experiments is shown in Figure 4.7. All measurements are performed using the alignment stage shown in § 3.2.3. Before carrying out AFM1 sensing measurements first in buffer, then in milk samples, chips are optically characterized.
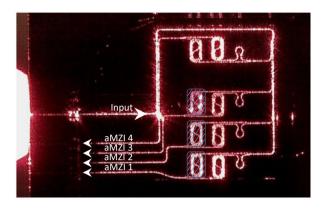
FIGURE 4.7: An image of aMZI based chip. On the left, the bright spot on the chip edge is the laser scattering at the input waveguide. Input and four output waveguides are coupled with a fiber array. Blue dashed zones indicate sensing windows.

4.2.1 Sensitivity and Limit of Detection

Figure 4.8a shows the normalized spectra of all four aMZIs. The transmission signals of all devices are normalized to the maximum signal of the one from the covered aMZI. FSR for open ones are the same and equal to 0.64 nm, while for the covered aMZI4 FSR is slightly different as a result of the refractive index difference. Knowing the FSR, we can calculate the wavelength shift from the phase shift in nm-s, considering that 1 rad $\cong \frac{FSR}{2\pi} =$ 0.1014 nm. For the further discussions the phase shift will be presented in nm-s. This is convenient to do for in order to compare our aMZI sensors with the various configurations.

Next, we defined the performances of our photonic sensors, by characterizing the volume (bulk) Sensitivity (S_b) of the three uncovered aMZIs. To calculate this parameter, we monitored in real-time the phase shift of the aMZI, as one arm of the sensor was exposed to glucose-water or salt (NaCl) solutions of various concentrations.
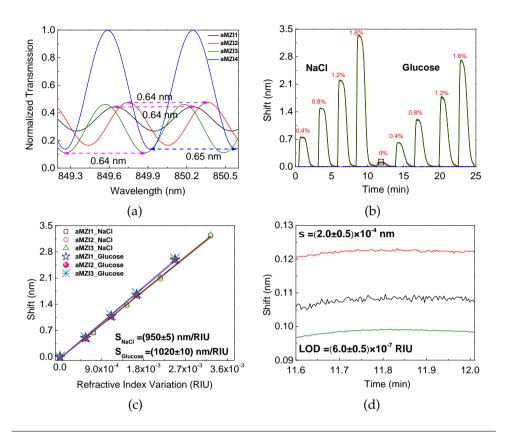
FIGURE 4.8: (a) Normalized transmission spectra of all four aMZIs. (b) The variation in refractive index is obtained by injections of water-glucose and salt solutions at different concentrations (glucose and NaCl concentrations are in %w/v labelled on the plot). (c) Corresponding wavelength shifts linear fit where the slope is the sensitivity. (d) Shift taken in 24 seconds corresponding to the period of 11.6÷12.0 minutes on the sensorgram marked inside the black square. The legend is the same for a, b and d plots.

We tested two different types of solutions in order to ensure that the sensitivity is independent from tested solutions. The measurement started with flowing pure water, which served as a reference liquid. The initial phase was determined when only water was flowing.

Figure 4.8b represents the shifts in nm as a function of the bulk refractive index variations measured simultaneously on four aMZI. Injection of the

glucose or salt solutions caused a significant shift, which was similar for the three sensors on the chip. Since aMZI4 was covered by cladding, the change of the flowing liquid over its surface did not lead to the wavelength shift. Before passing to glucose-water solutions, we injected pure water from the same reservoir of the flowing liquid and a small shift was caused by the temperature differences of the solutions injected from the valve and flowing inside the tubings. This shift later is considered as the baseline. Then, glucose-water solutions are injected at different concentrations.

Figure 4.8c shows the dependence of the shift versus the refractive index of the solution, i.e. the bulk sensitivity. We found a sensitivity of (950±5) nm/RIU and (1020±10) nm/RIU respectively for NaCl and glucose solutions for all the three exposed sensors. This small difference between sensitivities can be a result of the density difference, since in the same range of concentrations (note, concentrations are in %w/v), expressed as percentage there are more molecules of salt than glucose. Nevertheless, this difference is negligible and the fact that after each salt solution the signal is recovering yields that salt does not adsorb on the sensor surface. Finally measuring an average standard deviation of the signal σ=(2.0±0.5)×10^{-4} nm within 24 seconds (see Figure 4.8d) when analyte is missing, we calculated LOD $\cong (6.0 \pm 0.5) \times 10^{-7}$ RIU.

In order to verify the reproducibility, we repeated volumetric sensing measurements for more than 60 different photonic chips (all tested photonic chips before AFM1 measurements underwent volumetric sensing measurements). Figure 4.9 represents the resulting histograms for S_b and LOD, demonstrating a good reproducibility that permits to neglect any additional influence on the toxin sensing from the photonic point of view. A ≈10% spread for the mean value of the sensitivity is observed which is an indication of the repeatability of the sensor fabrication and testing. The mean value for bulk sensitivity is calculated to be $S_b \approx (1250 \pm 150)$ nm/RIU, while the mean value of LOD≈ $(1.2 \pm 0.3) \times 10^{-6}$ RIU.

In comparison with the sensitivity and LOD of the MRR sensors, one can see that the aMZI sensors have ≈10 times higher bulk sensitivity, while the LOD is in the same order of magnitude, i.e., in the range of 10^{-6} - 10^{-7} RIU. Thus, our aMZI sensors are comparable with other configurations (see Table 1.2). The big difference between the sensitivities of the MRRs and aMZIs is a result of a longer sensing length in a case of the aMZIs.
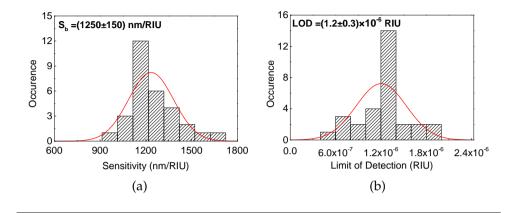
FIGURE 4.9: Statistics for the sensitivity and LOD for about 60 aMZI chips: (a) The histogram for sensitivity obtained by volumetric sensing measurements. The mean value is (1250±150) nm/RIU, even though the best measured sensitivity is (1600±100) nm/RIU. Bin size is taken 100 nm/RIU. (b) The histogram for LOD shows the distribution of LOD with 2×10^{-7} RIU bin size. The calculated minimum LOD is $(4.8\pm1.0)\times10^{-7}$ RIU. However the mean value for LOD is $(1.2\pm0.3)\times10^{-6}$ RIU.

4.2.2   aMZI surface functionalization with Fab'

Considering the results on the aptamer and Fab' based functionalization strategies, and the fact that aMZI are more sensitive, for AFM1 detection in milk aMZI sensors functionalized with Fab' are used. The surface functionalization is performed by Dr. Cristina Potrich. Fab' are immobilized on the Si_3N_4 surface adapting the protocol described in § 4.1.3.2, with some modifications related to the final step of the functionalization protocol. Figure 4.10 represents the schematics of Fab' functionalization approach with the AFM1 detection as the final step. Hence in the milk samples there are casein molecules present and the non-specific absorption of the casein on the Si_3N_4 surface can cause a significant fake signal parallel to the one from the Fab'-AFM1 specific binding, thus an addition step of casein passivation was carried out in order to reduce the casein non-specific effect in final milk sample tests.
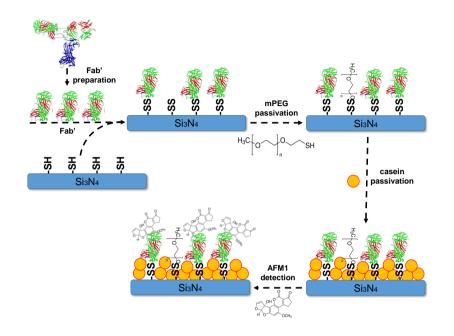
FIGURE 4.10: Schematics of the surface functionalization principle. Fab' fragments are prepared starting from whole antibodies (images of IgG and Fab' are adapted from structures deposited in the Protein Data Bank [131]). Fab' are bonded to the mercapto-silanized sensor surfaces with a disulfide bond. The non-reacted thiol groups are passivated by adding mercapto-PEGs (both 2.000 and 5.000 Da), while the non-specific binding sites still present on the surface are passivated with casein. Note, that the molecule sizes are not scaled and are not corresponding to the real proportions.

The functionalized chip is exposed at 0.1mg/ml of casein solution for 30 minutes, in order to increase the chip performances in a slightly dirty solution. The surface is finally cleaned using a PBS-EDTA buffer. The concentration of the Fab' is determined by measuring their absorbance with a Nanodrop instrument (Extinction coefficient (0.1%)=1.35 at 280 nm).

4.2.3 AFM1 sensing measurements in buffer

Figure 4.11a shows one complete measurement cycle. This includes toxin injection and regeneration of the sensors.

The measurement starts with flowing 50 mM MES buffer with pH 6.6 over the sensors. The phase of the three exposed sensors stays constant while flowing the buffer. We consider this phase value as the phase baseline. Next, the injection of 50 μL of a solution containing 10 nM AFM1 is followed in order to measure the evolution of the phase and, consequently, the wavelength of the aMZI due to the capture of the toxins from the functionalized aMZI.
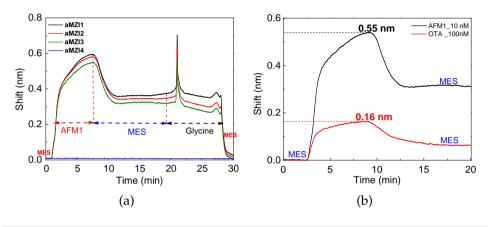

FIGURE 4.11: (a) Sensorgram recorded on the four aMZI sensors for a complete measurement cycle of 10 nM AFM1 solution. (b) Sensorgram for the specific detection of AFM1 compare to the one for non-target OTA at 10 times higher concentration.

The solution is inserted into the microfluidic chamber using an injection loop in order to avoid the formation of air bubbles in the microfluidic chamber during the buffer exchange and to have a known fixed injected volume. All measurements were done with a flow rate of 5 μL/min.

The solution reached the sensor surfaces after 40 seconds when we observed a large phase shift and, then, the phase grew almost linearly due to the specific binding of AFM1 to the exposed surfaces of the three aMZI. It looks like the binding of the toxin occurred between 2,5 and 7,5 minutes. A subsequent flow of MES buffer caused a decrease in the phase due to the rinsing of the unbound AFM1 from the sample surfaces. However the phase do not recover to the initial value due to the stable AFM1 binding on the surface, which is not rinsed with the subsequent flow of buffer solution.

The phase shift in time follows the kinetics of the binding and dissociation of the toxin to the antibody on the surface of the exposed aMZI arms. Finally, we injected a glycine solution at the 20th minute, in order to break the toxin-antibody bonds and remove all the linked toxins from the sensor surface while keeping the antibodies in place: i.e., we aimed to regenerate the sensor. After glycine solution at the 28th minute we injected MES again and the signal recovered the baseline. This means that AFM1 were completely removed from the surfaces of the sensors.

Note, that the functionalization aims at detecting AFM1 and not OTA, so this experiment allows testing the specificity of the sensor response as well. For this purpose we used OTA at 100 nM concentration. Figure 4.11b shows that even though the concentration of OTA is ten times higher than concentrations of AFM1, the non-specific signal is much lower in comparison with the specific signal. In fact, in the case of AFM1 at 10 nM, immediately before MES rinsing, the shift is 0.55 nm, while for OTA at 100 nM it reaches 0.16 nm. Note, that OTA related shift is not absolute and from chip to chip it can change, it is important that the difference of specific and non-specific signals remain stable for different chips.

A big number of chips functionalized with Fab' are tested for AFM1 various concentrations. We used different flow rates in order to optimize the sensor. As expected, flow rate does not affect significantly on the signal level. Figure 4.12a represents the sensorgram of 10 nM AFM1 detection, when the flow rate of the continuous flow is varying. The average shift corresponds to (0.4±0.05) nm. In further analyses for all concentrations we present an average value calculated from all measurements at given concentration.

Figure 4.12b shows the wavelength shift dependence versus AFM1 concentration. The difference between signal levels is mainly caused by Fab' degradation in time even though the functionalization and measurement protocols are always kept the same. For all measurements Fab' bought in December 2015 is used.
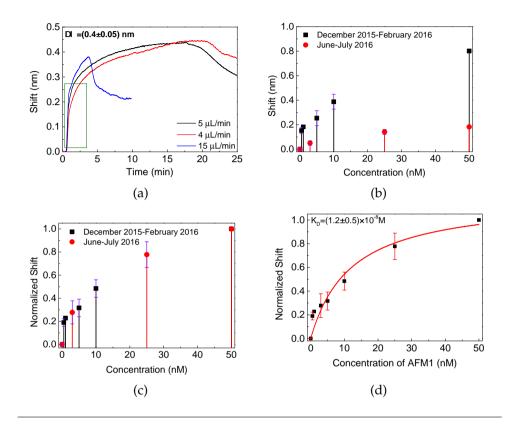
FIGURE 4.12: AFM1 measurements in MES buffer. (a) Sensorgram shows binding curves of AFM1 at 10 nM in case of various flow rates. (b) Shift due to AFM1 specific binding performed in different dates (seasons). (c) Normalized shift on the maximum signal of each season. (d) Normalized shift fit with Langmuir isotherm.

In order to compare results from different dates (seasons) of measurements all data are normalized on the maximum signal observed for the specific period (see Figure 4.12c). When we plot together all data points from 0.5 nM to 50 nM, we obtain a curve that is well fitted with a Langmuir isotherm. From the fit we extract the value of the dissociation constant (see Figure 4.12d), i.e., $K_D=(12\pm5)$ nM. Note, that for MRRs for dissociation constant of Fab'-AFM1 binding we calculated $K_D=(18\pm6)$ nM. This results prove the specific performance of the functionalized surface. For

the AFM1-Fab' binding affinity we get $K_A=(8\pm3)\times10^7$ M^{-1}. Therefore, the known affinity of this product family is in the range[4] of 10^9-10^{11} M^{-1} .

It is well known that molecular interactions, consequently, the rate constants are highly dependent from the flow rate, temperature, and surface functionalization, thus here we discuss a set of measurements performed on fresh functionalized and measured aMZI in the same day, keeping all parameters of the measurements constant, except the toxin concentration. We used 0.5 nM, 5 nM and 50 nM AFM1 concentrations (see Figure 4.13a). The flow rate was set at 10 μL/min. The volume of the injected solution was 70 μl. In order to calculate the dissociation constant from these measurements we derive it from the association and dissociation rate constants, as it is described in Chapter 2. We perform exponential fit for each of the curves between $\Delta t=10\div190$ seconds where the association takes place, as it is shown in Figure 4.13a.

Figure 4.13b shows the dependence of k_{obs} from the AFM1 concentration. The error bars represent the variation of k_{obs} resulting from the fit in $\Delta t\pm10$ s intervals. From the linear fit of k_{obs} as a function of the AFM1 concentration, we can extract values for k_{on} and k_{off}. The association and dissociation rate constants are found to be $(2.2\pm0.2)\times10^5$ M^{-1}s^{-1} and $(1.1\pm0.04)\times10^{-2}$ s^{-1} respectively. Using Eq. (2.40) for the dissociation constant we get $K_D=(50\pm5)$ nM and for the affinity $K_A=(2\pm0.2)\times10^7$ M^{-1}, respectively. Obtained values are in the same order of magnitude as the ones extracted from the Langmuir isotherm.

---

[4]http://www.abcam.com/aflatoxin-antibody-1c6-ab685.html

(a)

(b)

(c)
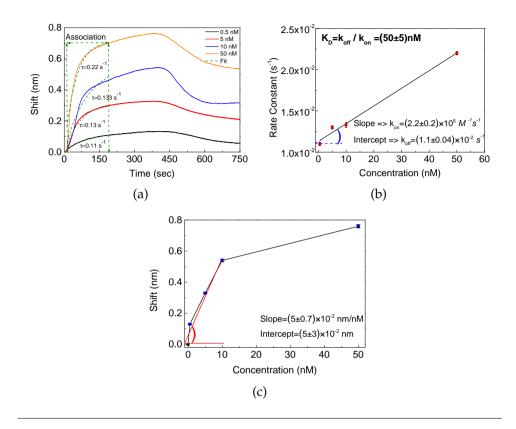
FIGURE 4.13: Sensing measurements of 0.5 nM, 5 nM and 50 nM AFM1 in MES buffer. (a) Sensorgrams for AFM1 different concentrations. (b) The dependence of the pseudo-first-order rate constant for AFM1 concentrations. Slope and intercept of the linear fit correspond to k_{on} and k_{off}. (c) The shift of AFM1 different concentrations. The red line is the linear fit for the small concentrations.

Finally, we can estimate the experimental LOD_{AFM1} in a buffer solution for the aMZI based sensors functionalized with Fab'. Figure 4.13c shows the dependence of the maximum shift at t=380 s from the AFM1 concentration. The error bars show the variation of the shift at 380 ± 20 s. The very small variation shows that the reaction is close to the equilibrium phase. By fitting the linear part of the dependence, for the slope of the linear regression, corresponding to the sensitivity, we get $S_{AFM1}=(5\pm0.7)\times10^{-2}$ nm/nM, while the intercept can be considered as a best estimate of the error σ_{AFM1}

in the concentration measurements. Thus, the of LOD_{AFM1}=(3±1) nM is calculated. Note, that this concentration is higher than the one required by the EU regulations. For this reason the concentrator module is integrated to the final detection system.

4.2.4   Proteins in milk samples

As it is known, milk is a complex substance that contains different molecules of various sizes, i.e., proteins, sugars, vitamins, etc. AFM1 has relatively small dimensions (327 g/mol) in comparison with proteins, in particular with casein ($\approx$ 22±3 kg/mol) [132] present in milk. One of the biggest challenges for any biosensing system meant for AFM1 detection, is non-specific signal from proteins adsorption.

Therefore, during *SYMPHONY* project by our partner ACREO first the blank samples are prepared, without AFM1, that contain known amount of protein. Those samples are measured in UNITN. A flow rate of 15 μL/min is used. As it is presented on the sensorgram in Figure 4.14a, a clear dependence of the signal level from the protein concentration is observed. Two different samples with the same 80 mg/L concentration of protein show a signal level of 4.5 nm and 4.3 nm (black and red curves), while for 60 mg/L protein concentration a signal of 2.9 nm (blue curve) is measured. These results show the need to perform a filtration of milk samples.

Next, the milk sample with measured 70 mg/L of proteins and 0.16 nM ($\approx$50 ng/L) of AFM1 concentrations undergoes a filtration with 3 kDa centrifugal filters (ELISA tests were performed in ACREO). Samples before and after filtration are tested. Figure 4.14b presents the sensorgram reporting measurements both on unfiltered and already filtered milk samples. A clear difference between the sensorgrams, recorded for these samples is distinguishable. Besides the signal levels, one can also appreciate the difference of binding kinetics proving the specific interaction of AFM1 with Fab', when proteins are removed from milk (see the red square in Figure 4.14b).

Filtration approach is used in the *SYMPHONY* final system, during the defatting step. Nevertheless, some proportion of proteins still remain in the prepared samples. For this reason each time before AFM1 measurements, a blank sample is tested and the resulting signal is considered as a baseline or 0 for further toxin analyses.
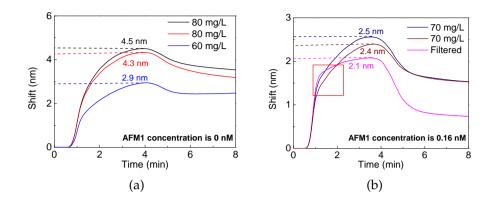
FIGURE 4.14: Sensorgram reports (a) a non-specific signal dependence from protein concentration, present in milk, (b) resulting difference of the signal when proteins are filtered from the milk.

4.2.5 AFM1 detection in milk samples

The final goal of the biosensor, developed in this thesis is the fast and accurate detection of AFM1 in milk samples. Therefore, we tested our device with the milk samples prepared with the procedure described in Appendix B.2. To achieve a fast detection, the sensing duration was reduced down to 90 seconds. This was done by increasing the flow rate up to 20 μL/min and by decreasing the injected solution volume down to 30 μL.

The level of AFM1 in tested samples was first analyzed with the ELISA assay. It is important to mention that the actual concentration of toxin was the result of the system concentrator block that concentrates the toxin in the eluate. For each concentration, we used freshly functionalized and optically characterized chip. This was done in order to avoid surface functionality degradation after regeneration process. The surface preparation process was highly repeatable for the same set of the functionalization processes.

Different sets of milk samples measurements have been performed, therefore here we present the results of the final project demonstration including all optimizations of the complete system.

First test of milk was performed on a sample free from AFM1, as a reference for the system. Note, that in the prepared samples still some proportion of proteins, in particular, casein remains, which causes a non-specific signal.

The non-specific adsorption of milk component even on passivated surfaces is a known phenomenon [133]. For further analysis, we consider this signal as a baseline equal to 0. Next, injecting the milk samples containing 0.96 nM, 1.3 nM, 1.5 nM and 2.2 nM AFM1 we observed a wavelength shift, which increased with the concentration increase, as shown in Figure 4.15a. A clear difference of the signal levels and kinetics between the reference sample and the ones with AFM1 indicates that a specific interaction between AFM1 and Fab' takes place, as expected.
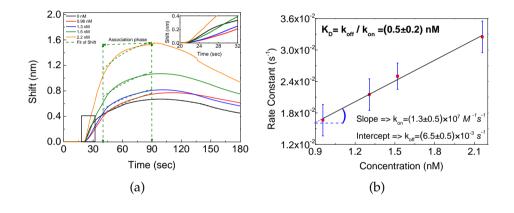
FIGURE 4.15: Sensing measurements of 0.5 nM, 5 nM and 50 nM AFM1 in MES buffer. (a) Sensorgrams for different concentrations of AFM1. (b) The dependence of the pseudo-first-order rate constant of the AFM1 concentrations. Slope and intercept of the linear fit correspond to k_{on} and k_{off}.

From the exponential fit of the curves in the $(40 \div 90) \pm 10$ seconds interval, where the association occurs, we obtain a linear dependence of the rate constant versus the AFM1 concentration, as shown in Figure 4.15b. The error bars show the rate constant variation in $\delta t = 10$ s. From the linear fit of k_{obs} as a function of the AFM1 concentration, we extract values for k_{on} and k_{off} respectively $(1.3 \pm 0.5) \times 10^7$ $M^{-1}s^{-1}$ and $(6.5 \pm 0.5) \times 10^{-3} s^{-1}$. Taking the dissociation constant as the ratio of k_{on} and k_{off}, $K_D = (0.5 \pm 0.2) \times 10^{-10}$ M and affinity $K_A = (2 \pm 1.5) \times 10^9$ M^{-1} values are calculated. All these values are in a range similar to the reported values for aptamers specific for AFM1 binding [134], while, to the best of our knowledge, this is the first time that

kinetic constants are measured for the interaction of AFM1 with Fab' both in buffer and in real samples. The difference of two orders of magnitude between the affinities in buffer and milk samples, respectively, is caused by several aspects. For example, in the tested milk samples there were present additional salts and molecules which could severely affect the interaction between AFM1 and Fab'. Moreover, the components present in real samples could be adsorbed on the surface via non-specific interactions and mask the binding sites specific for AFM1 with the final effect to slow down the kinetic and to decrease the affinity constant measured in milk samples.

4.2.6 Sensor calibration

After the successful demonstration of AFM1 detection in milk, the sensor calibration was realized based on the results presented above. For this set of measurements AFM1 was concentrated by a factor $\approx$20.

Figure 4.16 shows the dependence of the maximum observed shift (at t=90 s) versus AFM1 concentration in the milk samples. The error bars show the shift variation in 10 seconds.
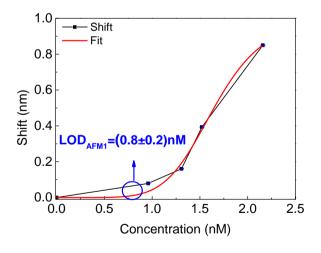

FIGURE 4.16: Calibration curve of the sensor based on aMZI functionalized with Fab'. With this device the lowest detectable concentration of AFM1 is calculated to be (0.8±0.2) nM.

For the small concentrations the increase of the shift is slow, while for the highest concentrations a higher slope is observed. As a 0 shift the signal from the blank sample is taken. By fitting the data with a Langmuir function, the lowest concentration of AFM1 that can be measured is defined (0.8$\pm$0.2) nM. Moreover, recalling the sample pre-concentration up to 20 times, the resulting LOD of $\approx$ (40$\pm$1) pM is achieved, that is lower than the requirements of EU regulations, i.e. 152 pM for adults and 76 pM for infants.

4.3 MRR sensors for anti-biotin analyses

The last section of this chapter is dedicated to the work done during my internship under the supervision of Dr. Geert Besselink in LioniX International. This study aimed to develop an affinity sensor for studying the interaction of biotinylated proteins and antibodies, in particular bovine serum albumin (BSA) and anti-biotin antibody. For this purpose a photonic chip based on six MRRs, presented in Figure 3.3 is used. A relatively fast and easy method for anti-biotin antibody affinity (K_A) and dissociation constant (K_D) measurement is demonstrated, as well as the reaction rate constants for this system are reported. Moreover, a fully regeneration of the sensor is achieved. It is quite tricky to achieve the regeneration protocol for this type of systems since it requires a regeneration solution that cleans the surface from bound molecules but, at the same time, does not damage the coating and the surface functionalization. Different approaches are proposed for system regeneration [71, 135], which highly depends on the specific functionalization and target molecules. Here we propose a method which has the main advantage of being able to regenerate the same chip up to eight times without damaging the sensor characteristics. Finally the specificity of our functional system is demonstrated by comparing the resonance wavelength shift for negative controls such as rabbit antibody and anti-biotin incubated with free biotin.

4.3.1 Sensitivity and Limit of Detection

As in the previous two cases, we firstly perform a sensor characterization in terms of bulk sensitivity and LOD. We monitored in real-time the resonance wavelength shift of six MRRs simultaneously, by flowing various sucrose

solutions over the sensor. The measurement started with flowing MilliQ, as a reference liquid for defining the baseline. Figure 4.17a represents the resonance shifts as a function of the bulk refractive index variations measured on six MRRs in parallel. All the MRRs behave rather similarly.
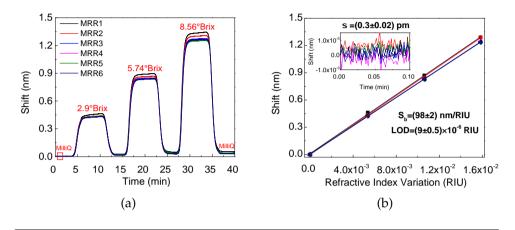
FIGURE 4.17: Bulk sensitivity measurements. (a) resonance shift curves for all six MRR sensors during the injection of the MilliQ-sucrose solutions (sucrose concentration[5]in °Brix is labelled on the plot), (b) evaluation of the bulk sensitivity.

Figure 4.17b shows the relation between the sucrose concentration (i.e., refractive index of the cladding liquid) and the resonance shift. Since the bulk sensitivity is a ratio of the wavelength shift over the refractive index change of the cladding liquid ($S_b = d\lambda_{res}/dn_c$), from the linear fit of the resonance shift vs sucrose concentration the value of bulk sensitivity is obtained. We obtain a sensitivity of (98±2) nm/RIU, while the variation among all six MRRs was less than 2.2%. This fact allows us to use this kind of sensor chip for multianalyte detection. In the work[50] it is previously reported a simulated value of 98nm/RIU for the sensitivity. In the same work it is also reported the quality factor of the MRR, i.e., $Q = 1.5 \times 10^4$. The LOD of the system is calculated considering a standard deviation equal to $\sigma = (0.3 \pm 0.02) \times 10^{-4}$ nm. Using Eq. 2.4 the LOD=$(9 \pm 0.5) \times 10^{-6}$ RIU is obtained.

---

[5]1°Brix is 1 gram of sucrose in 100 grams of solution (MilliQ).

Note, that the sensitivities and LOD for both MRR sensors, discussed in this thesis, are in the same order of magnitude, although the S_{FBK}=(80±12) nm/RIU<(98±2) nm/RIU=S_{LioniX}. This difference is a result of the waveguide dimensions, as well as the effective refractive index differences ($n_{eff,FBK}$ =1.66<1.99=$n_{eff,LioniX}$).

4.3.2 MRR surface preparation with Neutravidin

The preparation of the biorecognition layer on the MRR SiO_2/Si_3N_4 surface, i.e., the chemical coupling of Neutravidin and the next step of the capturing of biotinylated BSA can be monitored using the MRR resonance wavelength measurements. In order to immobilize biotinylated BSA for anti-biotin studies, first we performed protein Neutravidin (100 μg/ml in MES) direct physical adsorption on the SiO_2/Si_3N_4 surface. If the efficiency of adsorption would be satisfying this method is economically profitable and easy to realize. But as it is shown in sensorgram of Figure 4.18a, the physical adsorption was not equally distributed on all MRR on the chip and consequently later sensing measurements would not be compatible. On the figure the signal from only three out of six MRR are presented due to the measurement disturbance by air bubbles.

After flowing Neutravidin on the chip surface, the observed wavelength shift reflected the physical adsorption and layer formation. For the first two sensors we measured a shift of 0.06 nm, while the third one achieved 0.1 nm resonance wavelength shift. The difference of signals between MRR3 and other two was 45%.

Since the method was not reproducible, we moved to an alternative method, i.e., the covalent coupling of Neutravidin to the sensor surface. The functionalization of the chip surface with a carboxylate layer was applied by Surfix BV (Wageningen, The Netherlands) using their proprietary alkene technology. Then at Lionix International BV a multi-step approach is followed in order to achieve immobilization of biotinylated BSA. First the carboxylate groups were activated with EDC/NHS (0.4 M EDC/0.2 M NHS in 10 mM MES, pH 5.3), then coupling of the protein Neutravidin (100 μg/ml in MES) to the chip surface via reaction of the protein amino groups with the NHS-activated carboxylate groups is performed. Finally, the capturing of biotinylated BSA (25 μg/ml in PBS) by the immobilized Neutravidin is allowed to proceed.
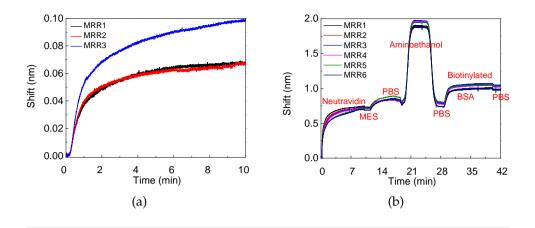
FIGURE 4.18: Sensorgram recorded on MRR sensors when: (a) Neutravidin (10 mM MES) physically adsorbed on the surface and then Biotinylated BSA is injected. (b) covalent coupling of Neutravidin (10 mM MES) was pursued onto the EDC/NHS activated carboxylated coating followed by the capturing of biotinylated BSA (in PBS).

Figure 4.18b shows a typical sensorgram that is obtained during the coupling of Neutravidin onto EDC/NHS activated carboxylated coating of the MRRs surfaces. At t=0 min MES buffer is flowing over the MRRs. After few seconds 100 μg/ml Neutravidin in MES buffer is injected with oscillating flow regime at 0.4 μL/s flow rate. From t=0.5 min to t=11 min the coupling of Neutravidin takes place. At t=11 min MES buffer again arrives to the sensors and the fact that the responses are not decreasing indicates the strength of the Neutravidin binding to the coated surfaces. At t=12 min PBS buffer replaces the MES buffer and a bulk shift is observed. Next the treatment with 1M aminoethanol (pH 9.3) is performed in order to quench the residual NHS activated groups and to dissociate any non-covalently coupled Neutravidin. At t=25 min again PBS buffer is injected to prepare for the biotinylated BSA immobilization. At t=28 min, 25 μg/ml biotinylated BSA (in PBS) is injected. A significant shift of 0.25 nm is observed for all six MRRs, after PBS buffer injection at t=40 min. Even though the variation between the individual MRR responses for Neutravidin is about 7%, i.e. 0.7 nm$\div$0.75 nm decreasing from the first to the last MRR, all the MRRs respond to the biotinylated BSA binding with a similar wavelength shift ($\pm$0.01 nm).

This last observation is very relevant since it allows to asses reproducibility in the 6 MRRs as what concerns the interaction of biotinylated BSA and anti-biotin antibody. The repeatability of the measurements is also achieved from chip-to-chip.

A sensor prepared this way can be modeled with the 1:1 binding scheme.

4.3.3 Anti-biotin sensing measurements

Since the bulk sensitivity measurements show that all six MRRs on the same chip have the same performances, in the next discussions only one MRR sensorgram will be used.

Sensing measurements are realized by using an oscillating flow supported by the pump described in § 3.4.2. Figure 4.19a shows the binding curves for six different concentrations of anti-biotin antibody equal to 6.6 nM (1μg/ml), 33 nM (5μg/ml), 66 (10μg/ml) nM, 132 nM (20μg/ml), 333 nM (50μg/ml) and 1065 (160μg/ml) nM[6], that are injected from the smallest to the highest concentration, after successfully regeneration cycle. Before and after the analyte injection, the MRR sensors are rinsed with a solution of PBS+0.1%BSA. While choosing the concentrations, a knowledge of the affinity and dissociation constant of biotinylated BSA - anti-biotin interaction can be useful. The affinity constant K_A for this particular molecular pair is in the range of 10^6 M^{-1} to 10^8 M^{-1}.

The Langmuir isotherm for these values of K_A is simulated to be within the violet region shown in Figure 4.19b. Normalizing to the maximum shift of the 1650 nM anti-biotin data, the measured points (red dots in figure) appear into the expected region. By fitting the data with the Langmuir function (black line) the affinity and dissociation constants can be extracted. Fit yields values of K_D=(2.0±0.5)×10^{-7} M and K_A=(5.0±1.5)×10^6 M^{-1} for dissociation and affinity constants, respectively.

---

[6]The molecular weight of anti-biotin is 150 kg/mol.
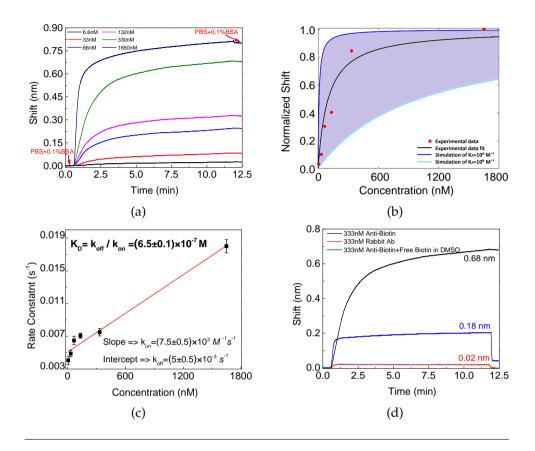
FIGURE 4.19: (a) Sensing measurements of 6.6 nM, 33 nM, 66 nM, 132 nM, 333 nM and 1650 nM anti-biotin antibody diluted in PBS+0.1% BSA buffer. (b) Langmuir isotherm for the dependence of the sensor response on the concentration of anti-biotin. The violet region corresponds to affinity constant of 10^6 $M^{-1} \div 10^8$ M^{-1}. (c) The dependence of the pseudo-first-order rate constant for anti-biotin different concentrations. Slope and intercept of the linear fit are k_{on} and k_{off}. (d) Sensorgram of the sensor due to 333 nM anti-biotin antibody (black curve), 333 nM rabbit antibody (red curve) and 333 nM anti-biotin antibody incubated with free biotin (blue curve).

An alternative way to calculate the dissociation constant is to derive it from the association and dissociation rate constants, as it was done for the AFM1 cases both in buffer and the milk samples. In order to get equilibrium, incubation times much longer than 12 minutes are needed. Therefore,

we perform exponential fit for each of the curves between t=1÷7 minutes. The fitted values of k_{obs} show a linear dependence from the antibody concentration (see Figure 4.19c). Error bars correspond to the fit interval of t±30 s.

From the linear fit of k_{obs} as a function of the antibody concentration C, we can extract values for k_{on} and k_{off}. The association and dissociation rate constants are found to be $(7.5\pm0.5)\times10^3$ $M^{-1}s^{-1}$ and $(5\pm0.5)\times10^{-3}$ s^{-1} values respectively. From these two rate constants, a dissociation constant of $K_D=(6.5\pm0.1)\times10^{-7}$ M and an affinity $K_A=(1.5\pm0.5)\times10^6$ M^{-1} are calculated. This value of the affinity constant again belongs to the known range.

The order of magnitude agreement between the values calculated by both methods confirms the validity of the measured data and shows that it is possible to perform precise analyses of affinity and kinetics in 2 hours, by considering about 13 minutes measurement time for each concentration injection and then sensor regeneration.

Finally, in order to determine the level of specificity, we perform sensing measurements by using negative control rabbit antibody at 333 nM concentration, as well as anti-biotin antibody at 333 nM pre-incubated with free, i.e., dissolved, biotin at 10 μM in 1% DMSO buffer. Figure 4.19d shows the sensorgrams. For anti-biotin (black curve), the response from specific bindings reaches 0.68 nm, while for rabbit antibody (red curve) after rinsing with PBS+0.1% BSA nearly no binding is observed. Similar situation happens while injecting anti-biotin at 333 nM concentration incubated with free biotin (blue curve). Incubation of antibody and free biotin is performed for 10 minutes before injection. After injection, we immediately observe a bulk shift of 0.18 nm due to the refractive index difference between the DMSO and the PBS+0.1% BSA buffers. Thus, when PBS+0.1% BSA again arrives to the sensor, the resonance wavelength returns to almost the initial value. A resulting shift of only 0.02 nm is achieved which indicates the specificity of the used sensor functionalization.

4.3.4   Regeneration Measurements

One of the big advantages of the proposed biosensors is the possibility to regenerate and reuse the same photonic chip several times without an additional surface recovery. It is challenging to find a right regeneration solution that will completely remove the bound analytes while not damaging

the functional layer on the sensor surface. A regeneration protocol that is investigated during this study uses 10 mM glycine/HCl pH 1.5 and needs long incubation times. Here we compare two regeneration processes with different durations.

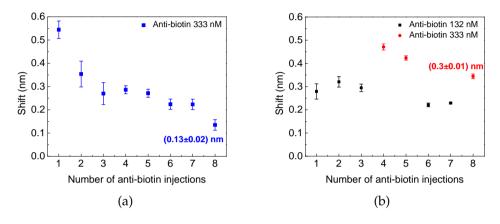(a)   (b)

FIGURE 4.20: Average shift of six MRRs for 8 cycles of regeneration. (a) signal decrease is observed when the regeneration with 10 mM glycine/HCl pH 1.5 is performed for less than 10 minutes. For all measurements, anti-biotin at 333 nM concentration is used (b) the stability of signal is achieved when the regeneration with 10 mM glycine/HCl pH 1.5 is performed for 20÷25 minutes. Different anti-biotin concentrations (132 nM and 333 nM) are used in order to prove the sensors ability to distinguish different concentrations after few regeneration cycles.

Figure 4.20a shows the resonance shift dependence of anti-biotin measurements for eight consequent cycles. Each data point presents an average of the six simultaneous signals and with corresponding error bars. In this case the regeneration incubation time for the six MRRs is less than 10 minutes. After each injection of the same 333 nM concentration of anti-biotin antibody, the sensor response decreases and the MRRs do not behave comparably (big error bars are the evidences). This indicates that the regeneration is not equally realized for all the six sensors and that after 10 minutes of 10 mM glycine/HCl pH 1.5 at $2\mu L/s$ unidirectional flow there are still analyte molecules bound to the ligands which decrease the sensor response to the next analyte injection. After 8 injections, more than 80% of the initial

signal is lost and only (0.13±0.02) nm shift is detected, while for the first injection a shift of (0.55±0.03) nm is achieved.

The situation is different when a longer incubation (20÷25 minutes at 2μL/s) is used. From Figure 4.20b it is obvious that with longer regeneration procedure we are able to recover the maximum response to anti-biotin at 132 nM concentration. In contrast to the previous case, here smaller error bars are obtained, indicating that all the six MRR sensors are equally regenerated. As a comparison, with short incubation times, when at the 8th injection the wavelength shift is (0.13±0.02) nm only, for long incubation times and for the same anti-biotin concentration at 333 nM, a wavelength shift of (0.3±0.01) nm is detected.

For the affinity and kinetic analyses six subsequent measurements are enough for reliable analyses, which makes the proposed regeneration protocol satisfying. In total for each concentration of analyte the measurement lasts at most 35÷40 minutes.

Appendix A

Materials and solutions

A.1   AFM1 sensing buffers

MES buffer, pH 6.6 [1]:

- MilliQ water,

- 50 mM 2-(N-morpholino)ethanesulfonic acid.

PBS buffer, pH 7:

- MilliQ water,

- 50 mM PBS mixture.

A.2   Sensor regeneration solution

Glycine, pH 2 :

- 100 mM glycine,

- HCl as needed to adjust the pH value.

A.3   Biological materials for AFM1 detection measurements

3-mercaptopropyltrimethoxysilane (MPTMS, 99%) is purchased from Gelest Ltd. (Maidstone, Kent, UK), was used without any further purification.

---

[1]Note, that pH 6.6 is the same as milk.

Toluene anhydrous (99.8%), toluene, dithiothreitol (DTT) and all powders for buffered solutions were purchased from Sigma-Aldrich s.r.l. (Milan, Italy). Methoxypolyethyleneglycolthiol (mPEG-SH) with the 2000 and 5000 molecular weights were purchased from Nektar Therapeutics AL (Huntsville, AL, USA). A rabbit polyclonal anti-AFM1 antibody and a horseradish peroxidase (HRP)-conjugated Aflatoxin M1 (AFM1-HRP) containing in I'screen Afla M1 milk Elisa kit were purchased from Tecna s.r.l. (Padua, Italy), while Aflatoxin M1 and Ochratoxin were purchased from Sigma-Aldrich s.r.l. (Milan, Italy). SuperSignal West Femto Chemiluminescent Substrate was purchased from Thermo Scientific (Rockford, IL, USA). The amino-modified DNA-aptamer sequence (5'-NH_2-$(CH_2)_6$-GT TGG GCA CGT GTT GTC TCT CTG TGT CTC GTG CCC TTC GCT AGG CCC ACA-3') was HPLC prified and purchased from IDT Integrated DNA (Leuven, Belgium).

A.4 Biological materials for anti-biotin analysis

The following materials are used: bovine serum albumin (BSA) (essentially fatty acid free, >96%), phosphate buffered saline (PBS) tablets, sucrose (>99.5 %), 2-(N-morpholino) ethanesulfonic acid (MES), glycine, dimethyl sulfoxide (DMSO), goat anti-biotin antibody and biotin were obtained from Sigma-Aldrich. Neutravidin (NeutrAvidin Protein), N-hydroxysuccinimide (NHS), 1-ethyl-3-(3-dimethylaminopropyl)carbo diimide hydrochloride (EDC) are supplied by ThermoFisher Scientific. No-WeighTM Biotinylated BSA is obtained from Pierce (Rockford, IL, USA).

Appendix B

Milk sample preparation

B.1 Fat removal process

Some proteases like Chymosin (present in rennet) are known to denature the casein fraction of milk as used in cheese curdling. In addition, low pH and temperature are traditionally used to denature whey proteins, which are separated from milk in the traditional "ricotta" cheese preparation. The identified procedure described below was designed to guarantee a high recovery of AFM1 and low protein samples after the process. The target was in particular to avoid loss of AFM1 in the separated protein phase since it was previously demonstrated that AF has good affinity with proteins and is therefore lost with normal curdling. The procedure steps are:

- adjust pH to 6.2 with Acetic acid, 5%; typ: 1.2 ml volume;

- heat to $30°C$;

- add solution of rennet from Muchor Miehei (0.8%w/v solution, 2 ml volume);

- wait 3 minutes, then cut in portions and mix without breaking the gel phase;

- heat up to $88°C$, gently mixing;

- mix acetic acid (5% solution) to adjust pH to 5.5, typ: 0.2 ml;

- mix gently for 5 minutes and separate the phases by coarse cloth.

The processed sample was then filtered with the filter system described in section 3.6.

B.2 Eluate preparation process

The main procedures for the concentration module consisted in:

- priming of the entire system to create air bubble free environment;

- milk delivery from the defatting unit;

- bullet rinses, i.e., first using 25 mL of admixture of MES buffer and Triton x100 detergent followed by rinse using 25 mL of pure MES. It has been demonstrated by ACREO that admixture of low concentrations of a detergent resulted in lower protein content of eluates and did not affect performance of antibodies;

- AFM1 release is realized by bullet heating. We let the bullet remain at $61\pm3\,^{\circ}C$ for about 6 min;

- injection of an eluate into the detector unit using syringe filled with compressed air.

Conclusions

In this thesis, various label-free optical biosensors have been studied. The main part of my work was dedicated to the development of a biosensing system for mycotoxin detection in milk. The mycotoxin of our interest is Aflatoxin M1, that is categorized as a human carcinogen and can be found in milk, nuts, maize, etc. Acceptable maximum level of AFM1 in milk according to the EU regulation is 152 pM for adults and 76 pM for infants, respectively. Several commercial techniques, like ELISA, HPLC, SPR exist for AFM1 detection in milk. However, they are laboratory based and require a trained personal to run the analyses, as well they are expensive and time-consuming.

Looking for a simple and effective method to screen the presence of AFM1 in milk, within a European project *SYMPHONY*, biosensors based on the Silicon On Insulator (SOI) Microring Resonators (MRR) and asymmetric Mach-Zehnder Interferometers (aMZI) have been developed. The sensing is performed by measuring the resonance wavelength shift in the MRR transmission or the phase shift of aMZI caused by the binding of the analyte on the functionalized sensor surface.

The knowledge of the label-free optical biosensors gained within the project *SYMPHONY*, I used in a development of a MRR based affinity biosensor for the proteins characterization.

The bulk sensitivity and the instrumental Limit of Detection for both types of sensors have been measured by the experimental setups developed during my PhD. The best sensitivity for the MRR based sensors fabricated in FBK and LioniX, respectively, (80±12) nm/RIU and (98±2) nm/RIU are measured, while for the aMZI based sensors the sensitivity of (1250±150) nm/RIU is measured.

The calculated instrumental LOD in all the three cases, independently from the sensitivity differences, is in the same range of the values, i.e., 10^{-6} - 10^{-7} RIU. This range is also reported in the state-of-the-art for various optical biosensing configurations.

The analyte sensitivity and the smallest detectable concentration of the target molecules (sensor LOD), although, depends on the surface functionalization and the selected ligands. For the AFM1 detection two functionalization strategies based on the DNA-aptamers and Fab' are developed. Therefore, it has been demonstrated that the Fab' functionalized sensors are more reproducible in comparison with the DNA-aptamer functionalized ones. Moreover, the experimental LOD_{AFM1}=(25±40) nM for aptamer and LOD_{AFM1}= (0.5±0.1) nM for Fab' based functionalized MRRs are estimated. Moreover, the aMZI based sensor, functionalized with Fab', has the experimental LOD_{AFM1}=(3±1) nM.

The results for LOD_{AFM1} arise the need of the concentrator module. The developed *SYMPHONY* system consists of three main modules, which first purify the milk sample from proteins (defatting module), then concentrate the sample (concentrator module) in order to suffice a nominal amount of AFM1 that reaches the photonic sensor (detector module). Even though the goal of a miniaturized biosensing system for AFM1 fast detection is not accomplished by the end of the project, however the integration and functional realization in laboratory is completed. In particular the connection between concentrator and detector modules is realized through injection valve and the syringe pumps.

For the tested milk samples the aMZI sensor shows the LOD_{AFM1}=(0.8±0.2) nM. Considering the concentration factor of 20, the resulting LOD_{AFM1} of $\approx$ (40±1) pM is achieved, that is lower than the requirements of the EU regulations.

In addition, the affinity constants for Fab'-AFM1 interaction in the milk samples is calculated for the first time. The affinity constant of K_A=(2±1.5)× 10^9 M^{-1} in the milk samples and K_A=(2±0.2)×10^7 M^{-1} in buffer, respectively, are measured. The higher affinity in the milk samples is observed due to the presence of an additional salt in the milk sample preparation buffer that causes stronger ionic interactions, consequently, the stronger molecular bindings.

In the study of the biotinylated BSA - anti-biotin interaction the affinity constant of K_A=(1.5±0.5)×10^6 M^{-1} is calculated using the multi-MRR

based biosensor functionalized with Neutravidin and immobilized by the biotinylated BSA.

The sensor regeneration protocol is developed, which allows to utilize the same sensor chip for the multiple times. However, for the reliable analyses, for each new experiment it is recommended to use a freshly functionalized sensor chip.

Dissemination activities

Peer-review journal papers

1. T. Chalyan, C. Potrich, E. Schreuder, R. Heideman, C. Pederzolli, A. Adami, and L. Pavesi. "Asymmetric Mach-Zehnder Interferometer based photonic biosensors for Fab'-AFM1 interaction study in milk". In: *Biosensors and Bioelectronics*.

2. F. Khozeymeh, M. Razaghi, T. Chalyan, and L. Pavesi. "Fast analytical modelling of a SOI micro-ring resonator for bio-sensing application". In: *Journal of Physics D: Applied Physics* (May 2018), pp. 1-12.

3. T. Chalyan, L. Pasaquardini, D. Gandolfi, R. Guider, A. Samusenko, M. Zanetti, G. Pucker, C. Pederzolli, and L. Pavesi. "Aptamer- and Fab'-functionalized microring resonators for Aflatoxin M1 detection". In: *IEEE Journal of Selected Topics in Quantum Electronics* 23.2 (March 2017), pp. 350-357.

4. F. Ramiro-Manzano, S. Biasi, M. Bernard, M. Mancinelli, T. Chalyan, F. Turri, M. Ghulinyan, M. Borghi, A. Samusenko, D. Gandolfi, R. Guider, A. Trenti, P.-É. Larré, L. Pasquardini, N. Prltjaga, S. Mana, I. Carusotto, G. Pucker, and L. Pavesi. "Microring Resonators and Silicon Photonics". In: *MRS Advances* 1.48 (May 2016), pp. 3281-3293.

5. A. Samusenko, D. Gandolfi, G. Pucker, T. Chalyan, R. Guider, M. Ghulinyan, and L. Pavesi. "A SiON Microring Resonator-Based Platform for Biosensing at 850 nm". In: *Journal of Lightwave Technology* 34.3 (Feb. 2016), pp. 969-977.

6. T. Chalyan, R. Guider, L. Pasquardini, M. Zanetti, F. Falke, E. Schreuder, R. G. Heideman, C. Pederzolli, and L. Pavesi. "Asymmetric Mach-Zehnder Interferometer based biosensors for Aflatoxin M1 detection". In: *Biosensors* 6.1 (Jan. 2016), pp. 1-10.

7. R. Guider, D. Gandolfi, T. Chalyan, L. Pasaquardini, A. Samusenko, C. Pederzolli, G. Pucker, and L. Pavesi. "Sensitivity and Limit of Detection of biosensors based on ring resonators". In: *Sensing and Bio-Sensing Research* 6 (Dec. 2015), pp. 99–102.

8. R. Guider, D. Gandolfi, T. Chalyan, L. Pasaquardini, A. Samusenko, G. Pucker, C. Pederzolli, and L. Pavesi. "Design and optimization of SiON ring resonators-based biosensors for Aflatoxin M1 detection". In: *Sensors* 15.7 (Dec. 2015), pp. 17300-17312.

Conference proceedings

1. T. Chalyan, G. A. J. Besselink, R. G. Heideman, and L. Pavesi. "Use of microring resonators for biospecific interaction analysis". In: *Proceedings of SPIE, the International Society for optics and photonics*, Optical Sensing, Imaging, and Photon Counting: Nanostructured Devices and Applications 2017, 103530Q (Sep. 2017).

2. T. Chalyan, L. Pasquardini, F. Falke, M. Zanetti, R. Guider, D. Gandolfi, E. Schreuder, C. Pederzolli, R. G. Heideman, and L. Pavesi. "Biosensors based on Si3N4 Asymmetric Mach-Zehnder Interferometers". In: *Proceedings of SPIE*, Optical Sensing and Detection IV, 98991S (May 2016).

3. G. Pucker, A. Samusenko, M. Ghulinyan, L. Pasquardini, T. Chalyan, R. Guider, D. Gandolfi, A. Adami, L. Lorenzelli, and L. Pavesi. "An integrated optical biosensor platform". In: *SPIE Newsroom*, (March, 2016).

4. T. Chalyan, D. Gandolfi, R. Guider, L. Pavesi, L. Pasaquardini, C. Pederzolli, A. Samusenko, and G. Pucker. Characterization of SiON microring resonators for biosensing applications". In: *IEEE BioPhotonics Conference Proceedings*, 3rd BioPhotonics 2015 International Conference, (Oct. 2015).

5. D. Gandolfi, R. Guider, T. Chalyan, L. Pavesi, L. Pasquardini, C. Peder-zolli, A. Samusenko, and G. Pucker. "Sensitivity and Limit of detection of biosensors based on ring resonators". In: *IEEE AISEM Annual Conference, 2015 XVIII*, (March 2015).

Books

1. T. Chalyan and S. Piccione. Conference book of abstracts of the *6th International Symposium on Optics and its Applications 2018 (OPTICS 2018)*. URL: https://goo.gl/gSAbaf.

2. N. Gevorgyan and T. Chalyan. Conference book of abstracts of the *4th International Symposium on Optics and its Applications 2016 (OPTICS 2016)*.

3. P. Beraldini, S. Biasi, Z. Bisadi, T. Chalyan, M. Compri, A. Gaspari, and S. Piccione. "Breaking Load of Twisted Yarns" In: *Proceedings of the event IPSP2016*, Industrial Problems Solving with Physics 2016. Chapter 3, pp. 45-64. Trento, Universita degli Studi di Trento, ISBN: 978-88-8443-712-9.

4. M. Bernard, A. Calabrese, T.Chalyan, Z. El Koura, F. Dallari, S. Donadello, N. Gatti, T. Klaser, M. Leonardi, V. Regazzoni, and A. Sartori. "Industrial Torque Sensor" In: *Proceedings of the event IPSP2015*, Industrial Problems Solving with Physics 2015. Chapter 3, pp. 41-63. Trento, Universita degli Studi di Trento, ISBN: 978-88-8443-674-0.

International Conferences

1. T. Chalyan, C. Potrich, E. Schreuder, and L. Pavesi. "Photonic biosensors for Fab'-AFM1 interaction study in real milk". *SPIE Photonics Europe 2018*, 22-26 April, 2018, Strasbourg, France;

2. T. Chalyan "Breaking the wall of sensors for food safety". *FALLING WALLS LAB BERLIN 2017*, 8-9 November, 2017, Berlin, Germany;

3. T. Chalyan, G. A. J. Besselink, R. G. Heideman, and L. Pavesi. "Use of microring resonators for biospecific interaction analysis". *SPIE Optics and Photonics 2017*, 5-10 August, 2017, San Diego, USA.

4. T. Chalyan, C. Potrich, Floris H. Falke, E. Schreuder, C. Pederzolli, R. Heideman, A. Adami, and L. Pavesi. "Optical biosensors for Aflatoxin M1 detection in milk". *5th International Symposium on Optics and its Applications (OPTICS 2017)*, 3-7 July, 2017, Wroclaw, Poland.

5. T. Chalyan and L. Pavesi. "Integrated Silicon Photonics and Microring Resonators for biosensing applications". *4th International Symposium on Optics and its Applications (OPTICS 2016)*, 25-28 July, 2016, Yerevan-Ashtarak, Armenia.

6. T. Chalyan, L. Pasquardini, C. Potrich, F. H. Falke, E. Schreuder, A. Adami, C. Pederzolli, R. G.Heideman, and L. Pavesi. "Biosensors based on Si_3N_4 Asymmetric Mach-Zehnder Interferometers". *ISOCS-MiNaB-ICT-MNBS 2016*, 25-29 June, Otranto (Lecce), Italy;

7. T. Chalyan, L. Pasquardini, F. Falke, M. Zanetti, R. Guider, D. Gandolfi, E. Schreuder, C. Pederzolli, R. G. Heideman, and L. Pavesi. "Biosensors based on Si3N4 Asymmetric Mach-Zehnder Interferometers". *SPIE Photonics Europe 2016*, 3-7 April, 2016, Brussels, Belgium;

8. T. Chalyan, R. Guider, D. Gandolfi, L. Pasquardini, F.H. Falke, E. Schreuder, C. Pederzolli, R.G.Heideman, and L. Pavesi. "Si_3N_4 based Asymmetric Mach-Zehnder Interferometers for biosensing applications". *3rd International Symposium on Optics and its Applications (OPTICS 2015)*, 1-5 October, 2015, Yerevan-Ashtarak, Armenia;

9. T. Chalyan, D. Gandolfi, R. Guider, L. Pavesi, L. Pasaquardini, C. Pederzolli, A. Samusenko, and G. Pucker. Characterization of SiON microring resonators for biosensing applications". *3rd International Conference BioPhotonics 2015*, 20-22 May, 2015, Florence, Italy;

10. T. Chalyan, D. Gandolfi, R. Guider, L. Pasaquardini, A. Samusenko, C. Pederzolli, G. Pucker, and L. Pavesi. "Performance optimisation of biosensors based on SiON microring resonators". *Developments in Optics and Communications 2015 (DOC Riga 2015)*, 8-10 April, 2015, Riga, Latvia.

Bibliography

[1] D. R. Thevenot et al. "Electrochemical biosensors: recommended definitions and classification". In: *Biosensors and Bioelectronics* 16.1–2 (Jan. 200), pp. 121–131. URL: `https://doi.org/10.1016/S0956-5663(01)00115-4`.

[2] YSI History. "Yellow Springs". In: (1975). URL: `https://www.ysi.com/about/history`.

[3] S. Cinti et al. "Electrochemical Biosensors for Rapid Detection of Foodborne Salmonella: A Critical Overview". In: *Sensors* 17.8 (Aug. 2017), pp. 1910–1933. URL: `http://www.mdpi.com/1424-8220/17/8/1910`.

[4] P. Damborsky, J. Svitel, and J. Katrlik. "Optical biosensors". In: *Essays in Biochemistry* 60.1 (June 2016), pp. 91–100. URL: `http://essays.biochemistry.org/content/60/1/91.article-info`.

[5] C. I. L. Justino et al. "Graphene based sensors and biosensors". In: *TrAC Trends in Analytical Chemistry* 91 (June 2017), pp. 53–66. URL: `https://doi.org/10.1016/j.trac.2017.04.003`.

[6] C. O. Parker et al. "Electrochemical Immunochip Sensor for Aflatoxin M1 Detection". In: *Analytical Chemistry* 81 (2009), pp. 5291–5298. URL: `http://hdl.handle.net/20.500.11937/10094`.

[7] W. Pang et al. "Piezoelectric microelectromechanical resonant sensors for chemical and biological detection". In: *TrAC Trends in Analytical Chemistry* 12.1 (Jan. 2012), pp. 29–44. URL: `10.1039/c1lc20492k`.

[8] L. G. Carrascosa et al. "Nanomechanical biosensors: A new sensing tool". In: *TrAC Trends in Analytical Chemistry* 25.3 (Mar. 2006), pp. 196–206. URL: `https://doi.org/10.1016/j.trac.2005.09.006`.

[9] M. A. Cooper and V. T. Singleton. "A survey of the 2001 to 2005 quartz crystal microbalance biosensor literature: Applications of acoustic physics to the analysis of biomolecular interactions". In: *Journal of Molecular Recognition* 20.3 (June 2007), pp. 154–184. URL: https://doi.org/10.1002/jmr.826.

[10] M. Pohanka et al. "Piezoelectric Biosensor for a Simple Serological Diagnosis of Tularemia in Infected European Brown Hares (Lepus europaeus)". In: *Sensors* 7.11 (Nov. 2007), pp. 2825–2834. URL: http://www.mdpi.com/1424-8220/7/11/2825.

[11] G. den Boef and A. Hulanicki. "Recommendations for the usage of selective, selectivity and related terms in analytical chemistry". In: *Pure and Applied Chemistry* 55.3 (1983), pp. 553–556. URL: http://dx.doi.org/10.1351/pac198855030553.

[12] J. Vessman et al. "Selectivity in analytical chemistry (IUPAC Recommendations 2001)". In: *Pure and Applied Chemistry* 73.8 (2001), pp. 1381–1386. URL: http://dx.doi.org/10.1351/pac200173081381.

[13] E.S. Kulisek and J.P. Hazebroek. "Comparison of extraction buffers for the detection of fumonisin B(1) in corn by immunoassay and high-performance liquid chromatography". In: *Journal of Agricultural and Food Chemistry* 48.1 (Jan. 2000), pp. 65–73. URL: DOI:10.1021/jf990696j.

[14] J. G. Bruno and J. L. Kiel. "In vitro selection of DNA aptamers to anthrax spores with electrochemiluminescence detection". In: *Biosensors and Bioelectronics* 14.5 (May 1999), pp. 457–464. URL: https://doi.org/10.1016/S0956-5663(99)00028-7.

[15] S. Mehrabani, A. J. Maker, and A. M. Armani. "Hybrid Integrated Label-Free Chemical and Biological Sensors". In: *Sensors* 14 (May 2014), pp. 5890–5928. URL: https://goo.gl/wpfrU2.

[16] X. Fan et al. "Sensitive optical biosensors for unlabeled targets: A review". In: *Analytica Chimica Acta* 620.1-2 (July 2008), pp. 8–26. URL: https://doi.org/10.1016/j.aca.2008.05.022.

[17] M. Nirschl, F. Reuter, and J. Voros. "Review of Transducer Principles for Label-Free Biomolecular Interaction Analysis". In: *Biosensors* 1.3 (May 2011), pp. 70–92. URL: http://www.mdpi.com/2079-6374/1/3/70.

[18] J.P. Lafleur et al. "Recent advances in lab-on-a-chip for biosensing applications". In: *Biosensors and Bioelectronics* 76 (Feb. 2016), pp. 213–233. URL: https://doi.org/10.1016/j.bios.2015.08.003.

[19] G. Luka et al. "Microfluidics Integrated Biosensors: A Leading Technology towards Lab-on-a-Chip and Sensing Applications". In: *Sensors* 15.12 (Dec. 2015), pp. 30011–30031. URL: doi:10.3390/s151229783.

[20] D. Lockwood and L. Pavesi. "Silicon photonics II. Components and integration". In: *Springer, Berlin, 2nd edition* (2011). URL: https://goo.gl/vxctci.

[21] A. L. Washburn et al. "Quantitative, label-free detection of five protein biomarkers using multiplexed arrays of silicon photonic microring resonators". In: *Analytical chemistry* 82.1 (Jan. 2010), pp. 69–72. URL: https://www.ncbi.nlm.nih.gov/pmc/articles/PMC2800857/.

[22] C. H. AHN et al. "Disposable Smart Lab on a Chip for Point-of-Care Clinical Diagnostics". In: *PROCEEDINGS OF THE IEEE* 92.1 (Jan. 2004), pp. 154–173. URL: https://goo.gl/KGLr8N.

[23] N. Verma and M. Singh. "Biosensors for heavy metals". In: *BioMetals* 18.2 (Apr. 2005), pp. 121–129. URL: https://link.springer.com/article/10.1007/s10534-004-5787-3.

[24] L. A. Pinnaduwage et al. "Explosives: a microsensor for trinitrotoluene vapour". In: *Nature* 425.6957 (Oct. 2003), p. 474. URL: doi:10.1038/425474a.

[25] R. Bhat, R. V. Rai, and A.A. Karim. "Mycotoxins in Food and Feed: Present Status and Future Concerns". In: *Comprehensive Reviews in Food Science and Food Safety* 9 (2010), pp. 57–81. URL: https://doi.org/10.1111/j.1541-4337.2009.00094.x.

[26] CAST. "Mycotoxins: Economic and Health Risks". In: *Council for Agricultural Science and Technology* (1989). URL: https://goo.gl/Tr79rJ.

[27] J. D. Groopman et al. "Aflatoxin Exposure in Human Populations: Measurements and Relationship to Cancer". In: *CRC Critical Reviews in Toxicology* 19.2 (Sept. 1988), pp. 113–145. URL: https://goo.gl/jen2Yx.

[28] C. Wild and Y. Yun. "Mycotoxins and human disease: a largely ignored global health issue". In: *Carcinogenesis* 31.1 (Jan. 2010), pp. 71–82. URL: `DOI:10.1093/carcin/bgp264`.

[29] IARC. "Evaluation of carcinogenic risks in humans". In: *International Agency for Research on Cancer* 82 (2002), pp. 171–274. URL: `https://monographs.iarc.fr/ENG/Monographs/vol82/mono82.pdf`.

[30] P. Christou, K. D. Miller, and A. Paau. "Chemical conversion of aflatoxin Bl to Ml". In: *Phytochemistry* 24 (1985), pp. 933–935. URL: `https://doi.org/10.1016/S0031-9422(00)83156-8`.

[31] IARC. "List of classifications". In: *International Agency for Research on Cancer* 56 (1993). URL: `https://goo.gl/xn6vkn`.

[32] S. H. Henry, F. X. Bosch, and J. C. Bowers. "Aflatoxin, Hepatitis and Worldwide Liver Cancer Risks". In: *Mycotoxins and Food Safety. Advances in Experimental Medicine and Biolog* 504 (2002). URL: `https://doi.org/10.1007/978-1-4615-0629-42`.

[33] K.P. Polzhofer. "Thermal stability of aflatoxin M1". In: *Z Lebensm Unters Forsch* 164.2 (June 1977). URL: `https://www.ncbi.nlm.nih.gov/pubmed/888578`.

[34] A. Behfar et al. "Determination of Aflatoxin M1 Levels in Produced Pasteurized Milk in Ahvaz City by Using HPLC". In: *Jundishapur Journal of Natural Pharmaceutical Products* 7.2 (May 2012), pp. 80–84. URL: `https://www.ncbi.nlm.nih.gov/pmc/articles/PMC3941857/`.

[35] Waters. "How Does High Performance Liquid Chromatography Work". In: *Waters Corporation* (2018). URL: `https://goo.gl/DRaUzq`.

[36] P. Bower. "High-Performance Liquid Chromatography (HPLC)". In: *Journal of Visualized Experiments* 170 (2018), pp. 1–4. URL: `https://www.jove.com/science-education/10156`.

[37] R. D. Stubblefield. "The Rapid Determination of Aflatoxin M1 in Dairy Products". In: *Journal of the American Oil Chemists Society* 56 (Sept. 1979), pp. 800–802. URL: `file:///F:/LabelFree/Writings/Thesis.pdf`.

[38] E. Engvall and P. Perlmaun. "Enzyme-linked immunosorbent assay, ELISA. Quantitation of specific antibodies by enzyme-labeled anti-immunoglobulin in antigen coated tubes". In: *Journal Immunology* 109.4 (Feb. 1972), pp. 129–135. URL: DOI:10.1049/el:20000340.

[39] A. Biancardi. "Determination of aflatoxin M1 residues in milk. A comparative assessment of ELISA and IAC-HPLC methods". In: *Industrie Alimentari* 36.2 (July 1997), pp. 870–876. URL: https://goo.gl/ZfPpgr.

[40] I. E. Tothill. "Biosensors and nanomaterials and their application for mycotoxin determination". In: *World Mycotoxin Journal* 4.4 (Nov. 2011), pp. 361–374. URL: https://goo.gl/mQ5YsP.

[41] N. Paniel, A. Radoi, and J. L. Marty. "Development of an electrochemical biosensor for the detection of Aflatoxin M1 in milk". In: *Sensors* 10.10 (Oct. 2010), pp. 9439–9448. URL: http://www.mdpi.com/1424-8220/10/10/9439.

[42] Y. Wang, J. Dostalek, and W. Knoll. "Long range surface plasmon enhanced fluorescence spectroscopy for the detection of Aflatoxin M1 in milk". In: *Biosensors and Bioelectronics* 24.7 (Mar. 2009), pp. 2264–2267. URL: https://doi.org/10.1016/j.bios.2008.10.029.

[43] G. Istamboulie et al. "Development of an impedimetric aptasensor for the determination of aflatoxin M1 in milk". In: *Talanta* 146 (Jan. 2016), pp. 464–469. URL: https://doi.org/10.1016/j.talanta.2015.09.012.

[44] P. Markaki and E. Melissari. "Occurrence of aflatoxin M1 in commercial pasteurized milk determined with ELISA and HPLC". In: *Food Additives and Contaminants* 14.5 (Jan. 1997), pp. 451–456. URL: https://goo.gl/8zsP7S.

[45] J.Bijl and C.V. Peteghem. "Rapid extraction and sample clean-up for the fluorescence densitometric determination of aflatoxin M1 in milk and mil powder". In: *Analytica Chimica Acta* 170 (1985), pp. 149–152. URL: https://doi.org/10.1016/S0003-2670(00)81738-9.

[46] M. Abouzied et al. "A sensitive ELISA for the detection and quantitation of Aflatoxin M1 (AFM1) in milk and dairy products". In: *Neogen Corporation* (2015). URL: https://goo.gl/s2fbH7.

[47]   R. S. Salter et al. "Collaborative Study of the Charm ROSA Safe Level Aflatoxin M1 Quantitative (SLAFMQ) Lateral Flow Test for Raw Bovine Milk". In: *Charm Sciences, Inc* (2018). URL: https://www.charm.com/rosa-lateral-flow-mycotoxin-strips.

[48]   L. Sibanda, S. Saeger, and C. V. Peteghem. "Development of a portable field immunoassay for the detection of Aflatoxin M in milk". In: *International Journal of Food Microbiology* 48.3 (June 1999), pp. 203–209. URL: https://doi.org/10.1016/S0168-1605(99)00045-8.

[49]   I. Langmuir and V. J. Schaefer. "Optical measurement of the thickness of a film adsorbed from a solution". In: *Journal of the American Chemical Society* 59.7 (1937), pp. 1406–1406. URL: DOI:10.1117/12.922139.

[50]   G.A.J. Besselink et al. "Performance of Arrayed Microring Resonator Sensors with the TriPleX Platform". In: *Biosensors and Bioelectronics* 7.2 (June 2016). URL: DOI:10.4172/2155-6210.1000209.

[51]   F. Vollmer and S. Arnold. "Whispering-gallery-mode biosensing: label-free detection down to single molecules". In: *Nature Methods* 5 (June 2008), pp. 591–596. URL: doi:10.1038/nmeth.1221.

[52]   B. Liedberg, C. Nylander, and I. Lunstrom. "Sensitive optical biosensors for unlabeled targets: A review". In: *Sensors and Actuators B: Chemical* 4 (1983), pp. 299–304. URL: doi:10.1016/0250-6874(83)85036-7.

[53]   E. Kretschmann and H. Reather. "Recent advances in lab-on-a-chip for biosensing applications". In: *Z. Naturforsch* 23 (Nov. 1968), pp. 2135–2136. URL: http://zfn.mpdl.mpg.de/data/Reihe_A/23/ZNA-1968-23a-2135_n.pdf.

[54]   V. Hodnik and G. Anderluh. "Toxin Detection by Surface Plasmon Resonance". In: *Sensors* 9.3 (Feb. 2009), pp. 1339–1354. URL: doi:10.3390/s9031339.

[55]   S. J. Daly et al. "Development of surface plasmon resonance-based immunoassay for aflatoxin B1". In: *Journal of Agricultural and Food Chemistry* 48.11 (Oct. 2000), pp. 5097–5104. URL: https://goo.gl/tuovM2.

[56] M. Puiu et al. "Kinetic approach of aflatoxin B1-acetylcholines terase interaction: A tool for developing surface plasmon resonance biosensors". In: *Analytical Biochemistry* 421.2 (Feb. 2012), pp. 587–594. URL: https://doi.org/10.1016/j.ab.2011.10.035.

[57] P. Kozma et al. "Integrated planar optical waveguide interferometer biosensors: A comparative review". In: *Biosensors and Bioelectronics* 58 (Aug. 2014), pp. 287–307. URL: https://doi.org/10.1016/j.bios.2014.02.049.

[58] P. V. Lambeck. "Integrated opto-chemical sensors". In: *Sensors and Actuators B* 8.1 (Apr. 1992), pp. 103–116. URL: https://goo.gl/H7pPYH.

[59] D. Gandolfi et al. "Role of Edge Inclination in an Optical Microdisk Resonator for Label-Free Sensing". In: *Sensors* 15.3 (Feb. 2015), pp. 4796–4809. URL: doi:10.3390/s150304796.

[60] D. Duval et al. "Interferometric waveguide biosensor based on Si-technology for point-of-care diagnostic". In: *Proceedings SPIE* 8431.P (2012). URL: DOI:10.1117/12.922139.

[61] Q. Liu et al. "Mach-Zehnder interferometer(MZI) point-of-care system for rapid multiplexed detection of microRNAs in human urine specimens". In: *Biosensors and Bioelectronics* 71 (2015), pp. 365–372. URL: http://dx.doi.org/10.1016/j.bios.2015.04.052.

[62] S. Dante et al. "All-optical phase modulation for integrated interferometric biosensors". In: *Optics Express* 20.7 (2012), pp. 7195–7205. URL: https://doi.org/10.1364/OE.20.007195.

[63] R.G. Heideman, R.P.H. Kooyman, and J. Greve. "Performance of a highly sensitive optical waveguide Mach-Zehnder interferometer immunosensor". In: *Sensors and Actuators B: Chemical* 10.3 (Feb. 1993), pp. 209–217. URL: https://doi.org/10.1016/0925-4005(93)87008-D.

[64] R.G. Heideman and P.V. Lambeck. "Remote opto-chemical sensing with extreme sensitivity: design, fabrication and performance of a pigtailed integrated optical phase-modulated Mach-Zehnder interferometer system". In: *Sensors and Actuators B: Chemical* 61.1–3 (Dec. 1999), pp. 100–127. URL: https://doi.org/10.1016/S0925-4005(99)00283-X.

[65]   Q. Liu et al. "Highly sensitive Mach-Zehnder interferometer biosensor based on silicon nitride slot waveguide". In: *Sensors and Actuators B: Chemical* 188 (Nov. 2013), pp. 681–688. URL: https://doi.org/10.1016/j.snb.2013.07.053.

[66]   A. Brandenburg and R. Henninger. "Integrated optical Young interferometer". In: *Applied Optics* 33.25 (1994), pp. 5941–5947. URL: https://doi.org/10.1364/AO.33.005941.

[67]   A. Ymeti et al. "Realization of a multichannel integrated Young interferometer chemical sensor". In: *Applied Optics* 42.28 (2003), pp. 5649–5660. URL: https://doi.org/10.1364/AO.42.005649.

[68]   S. Aikio, M. Hiltunen, and J. Hiltunen. "Compensation of drift by using a multichannel integrated Young interferometer". In: *Applied Optics* 54.25 (2015), pp. 4771–4780. URL: https://doi.org/10.1364/AO.54.004771.

[69]   C. G. B. Garrett, W. Kaiser, and W. L. Bond. "Stimulated emission into optical whispering modes of spheres". In: *Physical Review* 124 (Dec. 1961), pp. 1807–1809. URL: DOI:10.1117/12.922139.

[70]   H. Zhu et al. "Analysis of biomolecule detection with optofluidic ring resonator sensors". In: *Optics Express* 15.15 (2007), pp. 9139–9146. URL: https://doi.org/10.1364/OE.15.009139.

[71]   S. Zlatanovic et al. "Photonic crystal microcavity sensor for ultracompact monitoring of reaction kinetics and protein concentration". In: *Sensors and Actuators B: Chemical* 141.1 (Aug. 2009), pp. 13–19. URL: https://doi.org/10.1016/j.snb.2009.06.007.

[72]   K. De Vos et al. "Silicon-on-Insulator microring resonator for sensitive and label-free biosensing". In: *Optics Express* 15.12 (2007), pp. 7610–7615. URL: https://doi.org/10.1364/OE.15.007610.

[73]   M. Ghulinyan et al. "Monolithic Whispering-Gallery Mode Resonators With Vertically Coupled Integrated Bus Waveguides". In: *IEEE Photonics Technology Letters* 23.16 (Feb. 2011), pp. 1166–1168. URL: DOI10.1109/LPT.2011.2157487.

[74]   M. Ghulinyan et al. "Silicon-based monolithically integrated whispering-gallery mode resonators with buried waveguides". In: *Proceedings of SPIE* 8431 (Apr. 2012). URL: DOI:10.1117/12.922226.

[75] F. Vollmer et al. "Protein detection by optical shift of a resonant microcavity". In: *Applied Physics Letters* 80.21 (Apr. 2002), pp. 4057–4059. URL: `DOI:10.1063/1.1482797`.

[76] A. M. Armani et al. "Label-Free, Single-Molecule Detection with Optical Microcavities". In: *Science* 317.5839 (July 2014), pp. 783–787. URL: `DOI:10.1126/science.1145002`.

[77] M. D. Baaske, M. R. Foreman, and F. Vollmer. "Single-molecule nucleic acid interactions monitored on a label-free microcavity biosensor platform". In: *Nature Nanotechnology* 9 (Aug. 2014), pp. 933–939. URL: `DOI:10.1038/NNANO.2014.180`.

[78] F. Sedlmeir et al. "Detecting THz in the telecom range: All resonant THz up-conversion in a whispering gallery mode resonator". In: *2014 39th International Conference on Infrared, Millimeter, and Terahertz waves (IRMMW-THz)* (Sept. 2014), pp. 1–2. URL: `DOI:10.1109/IRMMW-THz.2014.6956012`.

[79] K. Grutter. "Optical Whispering-Gallery Mode Resonators for Applications in Optical Communication and Frequency Control". In: *PhD thesis Grutter:EECS-2013-23* UCB/EECS-2013-235 (Dec. 2013). URL: `http://www2.eecs.berkeley.edu/Pubs/TechRpts/2013/EECS-2013-235.html`.

[80] J. W. Silverstone et al. "Qubit entanglement between ring resonator photon-pair sources on a silicon chip". In: *Nature Communications* 6.7948 (Aug. 2015). URL: `DOI:10.1038/ncomms8948`.

[81] C. Castellan et al. "Tuning the strain-induced resonance shift in silicon racetrack resonators by their orientation". In: *Optics Express* 26.4 (Feb. 2018), pp. 4204–4218. URL: `https://doi.org/10.1364/OE.26.004204`.

[82] M. Borghi et al. "High-frequency electro-optic measurement of strained silicon racetrack resonators". In: *Optics letters* 40.22 (Feb. 2015), pp. 5287–5290. URL: `https://doi.org/10.1364/OL.40.005287`.

[83] A.D. Kersey et al. "Fiber grating sensors". In: *Journal of Lightwave Technology* 15 (1997), pp. 1442–1463. URL: `DOI:10.1109/50.618377`.

[84] N. Chen, B. Yun, and Y. Cui. "Tuning the sensing responses of polymer-coated fiber Bragg gratings". In: *Journal of Applied Physics* 104 (2006), p. 116110. URL: https://doi.org/10.1063/1.3042227.

[85] H.J. Patrick, A.D. Kersey, and F. Bucholtz. "Analysis of the response of long period fiber gratings to external index of refraction". In: *Journal of Lightwave Technology* 16.9 (Sept. 1998), pp. 1606–1612. URL: 10.1109/50.712243.

[86] X. Chen et al. "Real-time detection of DNA interactions with long-period fiber-grating-based biosensor". In: *Optics Letters* 32.17 (2007), pp. 2541–2543. URL: https://doi.org/10.1364/OL.32.002541.

[87] J. Lou, L. Tong, and Z. Ye. "Modeling of silica nanowires for optical sensing". In: *Optics Express* 13.6 (2005), pp. 2135–2140. URL: https://doi.org/10.1364/OPEX.13.002135.

[88] F. Xu, P. Horak, and G. Brambilla. "Optical microfiber coil resonator refractometric sensor: erratum". In: *Optics Express* 15.15 (2007), pp. 9385–9385. URL: https://doi.org/10.1364/OE.15.009385.

[89] F. Xu et al. "An embedded optical nanowire loop resonator refractometric sensor". In: *Optics Express* 16.2 (2008), pp. 1062–1067. URL: https://doi.org/10.1364/OE.16.001062.

[90] W. Liang et al. "Highly sensitive fiber Bragg grating refractive index sensors". In: *Applied Physics Letters* 86 (2005), p. 151122. URL: https://doi.org/10.1063/1.1904716.

[91] L. Tong et al. "Subwavelength-diameter silica wires for low-loss optical wave guiding". In: *Nature* 426.22 (Dec. 2003), pp. 816–819. URL: doi:10.1038/nature02193.

[92] L. Rindorf et al. "Photonic crystal fiber long-period gratings for biochemical sensing". In: *Optics Express* 14.18 (2006), pp. 8224–8231. URL: https://doi.org/10.1364/OE.14.008224.

[93] F.C. Chien et al. "Coupled waveguide–surface plasmon resonance biosensor with subwavelength grating". In: *Journal of Physics D: Applied Physics* 22.11 (May 2007), pp. 2737–2742. URL: https://doi.org/10.1016/j.bios.2006.11.021.

[94] J. Dostalek, J. Homola, and M. Miler. "Rich information format surface plasmon resonance biosensor based on array of diffraction gratings". In: *Sensors and Actuators B* 107 (Nov. 2005), pp. 154–161. URL: https://goo.gl/5N8Yfh.

[95] G.G. Nenninger et al. "Long-range surface plasmons for high-resolution surface plasmon resonance sensors". In: *Sensors and Actuators B* 74.1–3 (Apr. 2001), pp. 145–151. URL: https://doi.org/10.1016/S0925-4005(00)00724-3.

[96] K. Misiakos et al. "Broad-band Mach-Zehnder interferometers as high performance refractive index sensors: Theory and monolithic implementation". In: *Optics Express* 22.8 (2014), pp. 8856–8870. URL: https://doi.org/10.1364/OE.22.008856.

[97] A. Ymeti et al. "Realization of a multichannel integrated Young interferometer chemical sensor". In: *Applied Optics* 42.28 (2003), pp. 5649–5660. URL: https://doi.org/10.1364/AO.42.005649.

[98] S. M. Grist et al. "Silicon photonic micro-disk resonators for label-free biosensing". In: *Optics express* 21.7 (2013), pp. 7994–8006. URL: https://doi.org/10.1364/OE.21.007994.

[99] N. M. Hanumegowda et al. "Refractometric sensors based on microsphere resonators". In: *Applied Physics Letters* 87 (Sept. 2005), pp. 1–3. URL: https://doi.org/10.1063/1.2132076.

[100] I. M. White et al. "Label-free detection with the liquid core optical ring resonator sensing platform". In: *Methods in molecular biology* 503.1–3 (Apr. 2009), pp. 139–165. URL: https://www.ncbi.nlm.nih.gov/pubmed/19151939.

[101] A.N. Chryssis et al. "Detecting hybridization of DNA by highly sensitive evanescent field etched core fiber Bragg grating sensors". In: *IEEE Journal of Selected Topics in Quantum Electronics* 11.4 (Dec. 2005), pp. 864–872. URL: https://ieeexplore.ieee.org/document/1545988/.

[102] Z. He, Y. Zhu, and H. Du. "Long-period gratings inscribed in air- and water-filled photonic crystal fiber for refractometric sensing of aqueous solution". In: *Applied Physics Letters* 92.4 (Jan. 2008), pp. 1–3. URL: https://doi.org/10.1063/1.2838349.

[103] H.J. Lee, D. Nedelkov, and R.M. Corn. "Surface Plasmon Resonance Imaging Measurements of Antibody Arrays for the Multiplexed Detection of Low Molecular Weight Protein Biomarkers". In: *Analytical Chemistry* 78.18 (Sept. 2006), pp. 6504–6510. URL: DOI:10.1021/ac060881d.

[104] X. Li et al. "A surface plasmon resonance assay coupled with a hybridization chain reaction for amplified detection of DNA and small molecules". In: *Chemical Communication* 39.50 (Mar. 2014), pp. 5049–5052. URL: DOI:10.1039/c4cc01374c.

[105] Q. Liu et al. "Highly sensitive Mach-Zehnder interferometer biosensor based on silicon nitride slot waveguide". In: *Sensors and Actuators B: Chemical* 188 (2013), pp. 681–688. URL: https://doi.org/10.1016/j.snb.2013.07.053.

[106] A. J. Qavi et al. "Anti-DNA:RNA Antibodies and Silicon Photonic Microring Resonators: Increased Sensitivity for Multiplexed microRNA Detection". In: *Analytical Chemistry* 83.15 (June 2011), pp. 5949–5956. URL: DOI:10.1021/ac201340s.

[107] S. Sridevi et al. "Sensitive detection of C-reactive protein using optical fiber Bragg gratings". In: *Biosensors and Bioelectronics* 65 (Mar. 2015), pp. 251–256. URL: https://doi.org/10.1016/j.bios.2014.10.033.

[108] Consortium SYMPHONY. "Description of Work. Technical report". In: *Symphony - Annex I* (2013). URL: http://www.symphony-project.eu/.

[109] F. J. Aparicio et al. "Silicon oxynitride waveguides as evanescent-field-based fluorescent biosensors". In: *Journal of Physics D: Applied Physics* 47.40 (Nov. 2014). URL: https://doi.org/10.1088/0022-3727/47/40/405401.

[110] J. Homola. "Surface plasmon resonance sensors for detection of chemical and biological species". In: *Chemical Reviews* 108.2 (Jan. 2008), pp. 462–493. URL: DOI:10.1021/cr068107d.

[111] S. Zlatanovic et al. "Photonic crystal microcavity sensor for ultracompact monitoring of reaction kinetics and protein concentration". In: *Sensors and Actuators B: Chemical* 141.1 (Aug. 2009), pp. 13–19. URL: https://doi.org/10.1016/j.snb.2009.06.007.

[112] D. Gandolfi. "On-chip photonic label-free biosensors". In: *PhD Thesis. University of Trento* (2015). URL: http://eprints-phd.biblio.unitn.it/1452/.

[113] D. C. Stone and J. Ellis. "Stats Tutorial - Instrumental Analysis and Calibration". In: *Department of Chemistry, University of Toronto* (Sept. 2011). URL: http://www.chem.utoronto.ca/coursenotes/analsci/stats/LimDetect.html.

[114] I. M. White and X. Fan. "On the performance quantification of resonant refractive index sensors". In: *Optics Express* 16.2 (2008), pp. 1020–1028. URL: https://doi.org/10.1364/OE.16.001020.

[115] Y. Shen et al. "Plasmonic gold mushroom arrays with refractive index sensing figures of merit approaching the theoretical limit". In: *Nature Communications* 4.2381 (Aug. 2013). URL: http://dx.doi.org/10.1038/ncomms3381.

[116] A. Yariv. "Universal relations for coupling of optical power between microresonators and dielectric waveguides". In: *Electronics Letters* 36.4 (Feb. 2000), pp. 321–322. URL: DOI:10.1049/el:20000340.

[117] D. G. Rabus. "Ring Resonators: Theory and Modeling". In: *The Compendium* (2007), pp. 3–40. URL: https://goo.gl/js7uJL.

[118] M. Borselli, T. Johnson, and O. Painter. "Beyond the Rayleigh scattering limit in high-Q silicon microdisks: theory and experiment". In: *Optics Express* 13 (Mar. 2005), pp. 1515–1530. URL: https://doi.org/10.1364/OPEX.13.001515.

[119] S. M. Spillane et al. "Ideality in a Fiber-Taper-Coupled Microresonator System for Application to Cavity Quantum Electrodynamics". In: *Optics Express* 91.4 (July 2003), pp. 1–4. URL: http://www2.mpq.mpg.de/~tkippenb/PRLIdeality.pdf.

[120] M. Hofmann et al. "Asymmetric Mach-Zehnder interferometers without an interaction window in polymer foils for refractive index sensing". In: *Applied Optics* 55.5 (Feb. 2016), pp. 1124–1130. URL: http://dx.doi.org/10.1364/AO.55.001124.

[121] L. Chrostowski and M. Hochberg. "Silicon Photonics Design: From Devices to Systems". In: *Cambridge University Press* (2015). URL: https://goo.gl/9BpLue.

[122] R. Tobias and S. Kumaraswamy. "Biomolecular Binding Kinetics Assays on the Octet Platform". In: *ForteBio - A Division of Pall Life Sciences* (2013), pp. 1–22. URL: https://goo.gl/xS58nU.

[123] R.A Copeland. "Protein–Ligand Binding Equilibria". In: *Wiley-VCH* (Jan. 2002). URL: https://doi.org/10.1002/0471220639.ch4.

[124] R. Heideman, M. Hoekman, and E. Schreuder. "TriPleX-based integrated optical ring resonators for lab-on-a-chip and environmental detection". In: *IEEE Journal of Selected Topics in Quantum Electronics* 18 (Feb. 2012), pp. 1583–1596. URL: http://ieeexplore.ieee.org/abstract/document/6155587/.

[125] K. Worhoff et al. "TriPleX: A versatile dielectric photonic platform". In: *Advances in Optical Technologies* 4.2 (2015), pp. 189–207. URL: https://www.degruyter.com/view/j/aot.2015.4.issue-2/aot-2015-0016/aot-2015-0016.xml.

[126] A. Samusenko et al. "SiON Microring Resonator-Based Platform for Biosensing at 850 nm". In: *Journal of Lightwave Technology* 34.3 (Jan. 2016), pp. 969–977. URL: http://ieeexplore.ieee.org/document/7384690/.

[127] V. K. Singha et al. "Application of He-Ne laser to study the variation of refractive index of liquid solutions with the concentration". In: *Journal of Integrated Science and Technology* 1.1 (May 2013), pp. 13–18. URL: http://www.pubs.iscience.in/journal/index.php/jist/article/view/4.

[128] W.B. Shim et al. "Chemiluminescence competitive aptamer assay for the detection of aflatoxin B1 in corn". In: *Food Control* 36.1 (Feb. 2014), pp. 130–135. URL: http://refhub.elsevier.com/S2214-1804(15)30012-X/h0045.

[129] T. Chalyan et al. "Asymmetric Mach-Zehnder Interferometer based biosensors for Aflatoxin M1 detection". In: *Biosensors* 6.1 (Jan. 2016), pp. 1–10. URL: http://www.mdpi.com/2079-6374/6/1/1.

[130] K. Yoshimoto et al. "Direct Observation of Adsorption-Induced Inactivation of Antibody Fragments Surrounded by Mixed-PEG Layer on a Gold Surface". In: *Journal of the American Chemical Society* 132 (2010), pp. 7982–7989. URL: https://pubs.acs.org/doi/10.1021/ja910372e.

[131] T. M. Dillon et al. "Structural and functional characterization of disulfide isoforms of the human IgG2 subclass". In: *Journal of Biological Chemistry* 283.23 (June 2008), pp. 16206–16215. URL: doi:10.1074/jbc.M709988200.

[132] H. W. Modler. "Functional Properties of Nonfat Dairy Ingredients - A Review. Modification of Products Containing Casein". In: *Journal of Dairy Science* 68.9 (Sept. 1985), pp. 2195–2205. URL: https://goo.gl/9BpLue.

[133] A. Karczmarczyk et al. "Sensitive and rapid detection of aflatoxin M1 in milk utilizing enhanced SPR and p(HEMA) brushes". In: *Biosensors and Bioelectronics* 81.1 (July 2016), pp. 159–165. URL: https://doi.org/10.1016/j.bios.2016.02.061.

[134] S. Malhotra et al. "Selection of aptamers for aflatoxin M1 and their characterization". In: *Journal of Molecular Recognition* 27.8 (Aug. 2014), pp. 493–500. URL: https://onlinelibrary.wiley.com/doi/abs/10.1002/jmr.2370.

[135] A.W. Peterson et al. "Kinetic Control of Hybridization in Surface Immobilized DNA Monolayer Films". In: *Journal of American Chemical Society* 122.32 (July 2000), pp. 7837–7838. URL: https://pubs.acs.org/doi/abs/10.1021/ja0015489.